Review

A review of modulation strategies for improving catalytic performance of transition metal phosphides for oxygen evolution reaction

Chen-Jin Huang, Hui-Min Xu, Ting-Yu Shuai, Qi-Ni Zhan, Zhi-Jie Zhang, Gao-Ren Li [*]

College of Materials Science and Engineering, Sichuan University, Chengdu 610065, China

ARTICLE INFO

ABSTRACT

Recently, researchers have focused on non-noble metal catalysts to replace noble metal catalysts for oxygen evolution reaction that is crucial for hydrogen production from water splitting. Among many metal-based compounds, transition metal phosphides (TMPs) often exhibit excellent HER catalytic performance due to the high electronegativity of P, which is favored by researchers. However, the OER catalytic performance of TMPs is not outstanding. Thus, improving its OER catalytic performance is crucial for the realization of excellent overall water-splitting bifunctional TMPs catalysts. In this review, we take TMPs as an example to analyze how to prepare highly active OER catalysts. Firstly, the evaluation criteria of OER reaction are introduced to compare the activity of catalysts. Then, from two aspects of improving the intrinsic activity of active sites and increasing the number of active sites/active surface area, we analyzed how to prepare highly active OER catalysts. For the former, it is often necessary to explore the method to make the OER potential close to the thermodynamic limit on the basis of understanding the OER mechanism. Therefore, we first summarized the widely recognized OER mechanism. Then, in order to improve the intrinsic activity of active sites, this paper expounds how to prepare efficient OER catalysts from four aspects: optimizing the adsorption and desorption of key intermediates, generating and optimizing vacancies in the catalyst, building multiple active sites, and promoting the formation of active phases. These four aspects are in line with the mechanism one by one; To increase the number of active sites/active surface area, strategies for constructing unique nanostructures and selecting special carriers were proposed. Finally, we propose key issues and challenges for future development in view of the shortcomings of each method.

1. Introduction

The excessive burning of fossil fuels has brought severe energy crises and environmental problems. With population growth and economic development, environmental and energy issues have gradually attracted people's attention [1]. Hydrogen has the characteristics of high calorific value, clean and pollution-free. It is considered an ideal energy carrier and critical clean energy to solve environmental pollution and energy crises [2]. Fortunately, the overall electrocatalytic water splitting is an emerging hydrogen production method [3].

Hydrogen production from water electrolysis involves two half-reactions: cathodic two-electron hydrogen evolution reaction (HER) and anodic four-electron oxygen evolution reaction (OER). However, the large operational potential window required to couple HER and OER significantly hinders the universal application of hydrogen production from water electrolysis. Therefore, preparing efficient and stable

catalysts is the key to reducing hydrogen production's power consumption from electrolyzed water. The OER involves complex four proton-coupled electron transfer (PCET) steps, undergoes the formation of OH* , O* , OOH* intermediates, and requires a high overpotential to drive, eventually leading to slow electrolysis of water to produce hydrogen. Therefore, OER is the bottleneck of electrocatalytic water splitting [4]. Therefore, it is very urgent to find a suitable catalyst to reduce the energy barrier required for oxygen evolution reaction, which can make the water electrolysis hydrogen production reach the ideal practical level, so as to further solve the environmental problems and energy crisis.

Although researchers have developed ruthenium or iridium noble metal oxides (RuO_2 and IrO_2) for OER, their high cost and scarcity hinder their wide application [5]. Therefore, designing low-cost, highly stable, and highly active catalysts is necessary. The OER process relies heavily on the adsorption and desorption of intermediates, and the

---

metal ions in the catalyst often adsorb OH⁻, and the non-metallic ions capture electrons. The two processes interact to promote the OER process, so finding the suitable metal and non-metallic ions is crucial [6]. Researchers have devoted a lot of energy to the study of various non-metals, such as metal oxides [7], metal sulfides [8], metal hydroxides [9], metal nitrides [10], and metal selenides [11]. Among them, the transition metal phosphides (TMPs) are particularly favored by researchers [12]. This is because TMPs have a unique hydrogenase like catalytic mechanism [13]. M^{x+} and P^{y-} act as proton receptors and hydride receptors, respectively, thus generating high water decomposition catalytic activity [14]. In addition, M^{x+} and P^{y-} play an important role in hydroxyl adsorption and O_2 desorption respectively [15]. The role of P in TMPs is also reflected in that the embedded transition metal lattice can increase the atomic spacing, weaken the interaction between metals and make the d-band shrink, increase DOS and endow it with good conductivity [16]. Secondly, through P alloying, metal dissolution can be effectively inhibited from thermodynamics, thus improving the corrosivity and stability of the catalyst [17,18]. In addition, P will be oxidized into phosphate species in the OER catalytic process, which can distort the geometric configuration of the catalyst to improve the surface wettability, help to absorb water molecules, and effectively improve the OER activity [19,20]. Finally, the difference in composition will lead to different electronic structures, forming metal phase, semiconductor phase or insulating phase. The chemical properties of P are very active and diverse. Therefore, proper adjustment of the stoichiometric ratio and composition of metal and P can produce a variety of structures, showing different physical and chemical properties, such as high conductivity [21]. The properties of M-P bond depend on the stoichiometry and electronegativity difference between M and P [22]. In TMPs, metal is relatively positively charged and P is relatively negatively charged, so M-P bonding has certain covalence and ionicity, which can make the catalyst more stable in the catalytic process [23,24]. Phosphide can be divided into metal rich TMP and phosphorus rich TMP according to the stoichiometric ratio of metal/phosphorus. The electrons of phosphorus rich phosphides are often concentrated around P, which is not an ideal catalyst. In contrast, metal rich phosphides have attracted much attention [25]. In terms of conductivity, rich metal TMPs are closer to metals than semiconductors and insulators, because the existence of M-M bonds in rich metal TMPs makes them have metallic properties, even superconductivity [26]. The rich M-P bonds in metal rich TMP endow metal phosphides with certain hardness, thermal stability and chemical stability [21].

Zhou et al. compared the OER activity of phosphides, oxides and sulfides containing the same transition metals [27]. The results showed that the catalytic performance was phosphide>sulfide>oxide. The author believes that the conductivity of oxides and sulfides is inferior to that of metal rich phosphides, which have some metal properties [28]. At the same time, compared with the layered structure of metal sulfide, the isotropy of phosphide makes the surface rich in unsaturated coordination atoms, which are expected to be the active sites of OER [29]. To sum up, among many non-noble metal-based compounds, TMP has excellent electrocatalytic performance and is widely concerned. However, there is still a lack of more evidence to explain why the activity of TMPs is superior to that of TM oxides/hydroxides. It is still necessary for researchers to design experiments for phosphate species generated in the OER process or for the surface reconstruction phenomenon in the OER process to explore the underlying mechanism.

The researchers' studies on TMPs mainly focused on Co based catalysts and Ni based catalysts. Positively charged cobalt ions can act as hydroxyl acceptors to promote the cleavage of O-H bonds and the formation of O-O bonds during OER and are considered critical raw materials for synthesizing efficient water-splitting catalysts [30]. The surface of cobalt phosphide undergoes an in-situ transformation during the OER process into its corresponding oxide/hydroxide phase, which is considered to be a true active species. And the original cobalt phosphide forms a conductive network. The active sites are attached to the

conductive network, which enhances the conductivity of the material, so cobalt phosphide is a potential OER catalyst with potential. Cobalt phosphide is considered to be a suitable water splitting catalyst by researchers because of its low cost, non-toxicity, and good catalytic performance. At present, it has been studied in various forms, including nanosheets [31], nanowires [19], and nanotubes [32]. In addition to cobalt phosphide as a popular catalyst for electrolytic water in the TMPs, nickel phosphide with a unique electronic structure is also favored by researchers. The excellent OER performance of nickel-based phosphides is due to the modulation of the local electronic environment of the Ni species [33]. Nickel phosphide also has an incompletely filled orbit, which can easily give or obtain electrons. The content of P in NiP can regulate its OER and HER activities. The metal rich NiP has high OER activity, and the phosphorus rich NiP has high HER activity [34,35]. For OER, P in NiP can be used as the conductive support of the active species hydroxyl oxide in the OER process, but the removal of surface P is required [34,36]. Kim et al. showed that the dissolution step in pulse reverse electrodeposition can promote the removal of PO^{x-} by regulating a stronger dissolution process, thus exposing more OER active sites (Ni $(OH)_2$, NiO and NiOOH) of NiP [37]. Therefore, nickel phosphide also has the potential of high OER activity.

In this review, we take TMPs as an example to analyze how to realize highly active OER catalysts. Firstly, the evaluation criteria of OER reaction are introduced to compare the activity of catalysts. Then, from two aspects of improving the intrinsic activity of active sites and increasing the number of active sites/active surface area, we analyzed how to prepare highly active OER catalysts. For the former, it is often necessary to explore the method to make the OER potential close to the thermodynamic limit on the basis of understanding OER mechanism. Therefore, we first summarized the widely recognized OER mechanism. Then, in order to improve the intrinsic activity of active sites, this paper expounds how to prepare efficient OER catalysts from four aspects: optimizing the adsorption and desorption of key intermediates, generating and optimizing vacancies in the catalyst, building multiple active sites, and promoting the formation of active phases. These four aspects are in line with the mechanism one by one; To increase the number of active sites/active surface area, strategies for constructing unique nanostructures and selecting special carriers were proposed. Finally, we propose key issues and challenges for future development in view of the shortcomings of each method.

2. Electrochemical parameters of evaluating OER catalytic performance

The ideal electrocatalysts should have following advantages: (1) excellent electrocatalytic activity; (2) Rich reserves, low price, no pollution; (3) remarkable stability, the catalyst can work for a long time and the performance degradation is not obvious. Therefore, a series of evaluation criteria are needed to evaluate the OER performance of catalysts. The commonly used evaluation indicators include overpotential, Tafel slope, ECSA, TOF, stability and R_{ct}.

2.1. Overpotential

The standard electrode potential for OER is 1.23 V (vs. RHE). However, due to the influence of hysteresis kinetics, activation barrier, and series resistance, it is necessary to apply an additional potential far from equilibrium at the anode to drive the OER process. This additional potential is called overpotential (η), which represents the difference between the genuine and equilibrium potential. η can be separated into concentration overpotential, activation overpotential and resistance overpotential. The concentration overpotential is due to the fact that the ion concentration near the electrode surface is not identical to the genuine ion concentration in the solution due to the unhurried ion diffusion. Stirring is a method to reduce the concentration polarization as much as possible, but it is impossible to completely eliminate the

concentration overpotential due to the existence of the diffusion layer on the electrode surface. The activation overpotential is caused by the slow electrochemical reaction, which can reflect the intrinsic catalytic performance of the catalyst. Researchers often screen out excellent catalysts based on this. Resistance overpotential is due to the resistance between the test system and the interface, which can be eliminated by iR compensation.

According to the Butler-Volmer equation, only part of the electric energy can cause the change of the electrode potential in the electrochemical reaction process, so the overpotential is the regulator of the electrochemical reaction rate. By controlling the magnitude of overpotential, the electrochemical reaction rate can be changed by several orders of magnitude. Therefore, it is extremely important to study the overpotential to improve the reaction rate.

An overpotential at 10 mA cm^{-2} is typically selected as a benchmark for characterizing and comparing OER electrocatalysts in various electrolytes. The overpotential at this point is defined as η_{10}. However, the overpotential is sometimes affected by the double-layer capacitance, and the measurement is no longer accurate at a current density of 10 mA cm^{-2} [43]. A higher current density, such as an overpotential at a current density of 100 mA cm^{-2} is selected as the evaluation criterion [38], or the LSV curve is plotted at a slow scan rate to reduce the effect of double-layer capacitance [45]. It is worth mentioning that high current densities are often utilized in industry to produce hydrogen gas more quickly. Therefore, comparing the overpotential at high current density is more commercially significant [39,40]. However, Kibsgaard et al. showed that the normalization of the test current by geometric area can only reflect the apparent activity but not the intrinsic activity [40], because the actual surface area of the catalyst should be much larger than the geometric surface area of the electrode.

In the three-electrode system, researchers usually select the appropriate reference electrode (RE) for electrochemical measurement, and use reversible hydrogen electrode (RHE) for overpotential measurement [41]. The overpotential of OER can be calculated by Eq. (1) by linear sweep voltammetry [42].

$$\eta = E_{applied} - E_0 - iR \tag{1}$$

In this formula, $E_{applied}$ is the actually applied potential, E_0 is the theoretical equilibrium value (1.23 V), and iR is the ohm correction under the same conditions. Where R is the overall resistance, including contact resistance between catalyst and substrate, the charge transfer resistance between catalyst and electrolyte and the intrinsic resistance of catalyst, and i is the current at a specific current density [42]. This is because in the three-electrode system, there will be an ohmic voltage drop between the working electrode (WE) and reference electrode (RE), so iR compensation should be performed when calculating the overpotential [41]. It is worth mentioning that when applied to water splitting, there is an unavoidable R resulting in power consumption. Therefore, more helpful information comes from overpotentials not determined by iR compensation, especially when the two differ significantly at high current densities [42]. Unfortunately, few studies have reported both uncompensated overpotentials and overpotentials after iR compensation.

2.2. Tafel slope and exchange current density

As early as 1905, Tafel analyzed HER of various metal electrodes and first proposed an empirical formula for describing electrode kinetics: the Tafel formula, which is described by formula (2) [43].

$$\eta = a + b \times \log\left(\frac{j}{[j]}\right) \tag{2}$$

where $[j]$ is the unit current density so that it is dimensionless, and b is the Tafel slope.

Later generations derived the Tafel equation from the Butler-Wolmer

Eq. (3) (B-V equation) [44], expressed as Eq. (4) [45].

$$j = j_0 \exp\left[\frac{\alpha_a zF}{RT}\left(E - E_{eq}\right)\right] - j_0\left[-\frac{\alpha_c zF}{RT}\left(E - E_{eq}\right)\right] \tag{3}$$

$$\eta = \frac{RT}{\alpha F}\ln(j_0) - \frac{RT}{\alpha F}\ln(j) \tag{4}$$

where α is the transfer coefficient, F is the Faraday constant, R is the ideal gas constant (8.314 J K^{-1} mol^{-1}), T is the absolute temperature, j_0 is the exchange current density, j is the current density, and η is the overpotential.

There is a linear relationship between the overpotential and the logarithmic form of the current density. The charge transfer coefficient can be calculated by the Tafel slope, which is difficult to measure directly from other experiments. The Tafel slope can be determined by redrawing the log$j \sim \eta$ image based on the polarization curve (the linear sweep voltammograms, LSV curves). The ordinate of Tafel image (Potential (V vs. RHE)) is the abscissa of the LSV (Potential (V vs. RHE)). The abscissa of the Tafel image can be obtained by taking the logarithm of the absolute value of the ordinate of the LSV curve, as shown in Fig.1 (a, b) [46].

Two important parameters can be obtained from the Tafel image. One is the Tafel slope, which is usually related to the electrochemical reaction mechanism, indicating how fast the current density increases as the overpotential increases. The unit of the Tafel slope is generally mV dec^{-1}, representing the amount of change required for an overpotential when the current changes tenfold. As we expect the reaction to proceed quickly and efficiently, the Tafel slope is the smaller, the current increases by ten times, the smaller the voltage increases, the lower the energy consumption. In the equation, the smaller Tafel slope (b) indicates excellent electrocatalytic kinetics, which means that only a tiny overpotential change is required to meet the rapid increase in current density. It is worth noting that if we expect the reaction to proceed toward a specific path, it is necessary to determine whether the Tafel slope should be large or small based on selectivity.

It is worth noting that some studies have pointed out that using LSV and CV curves to obtain the Tafel slope is unstable. This is because both LSV and CV are not steady-state tests. Although the rate of linear voltammetric scanning is 1 mV s^{-1}, the current obtained is still not a steady-state current, but the Tafel slope needs to be tested in a steady state. If the sweep speed is controlled at 0.01 mV s^{-1}, it is close to a steady state, but the experimental time cost increases. So we can choose CA steady-state test [45]. In addition, the theoretically derived Tafel slope simplifies surface coverage, but in actual operation, the surface coverage will change according to different overpotentials. Therefore, the Tafel curve should be measured multiple times over a wide overpotential range to obtain a more accurate Tafel slope [45,47]. In terms of application, the Tafel slope can be used to infer the reaction's rate-determining step (RDS). Kazuhiro Takanabe et al. took the OER reaction as an example, assuming that each step of the OER process was RDS, and obtained different Tafel images [47]. It is worth noting that the observed Tafel slope is 120 mV dec^{-1} when the surface material coverage formed in the step before RDS is the largest. In addition, by observing the Tafel images with the steps of generating MOH and MOO$^-$ as RDS, the region with a Tafel slope of 30 mV dec^{-1} can be found. This shows that judging RDS only based on the Tafel slope is inaccurate. Tafel slope, overpotential, and coverage should be combined to determine the RDS of the reaction.

Another important kinetic parameter describing the electrochemical reaction rate under equilibrium conditions is the exchange current density (j_0), defined as the reduction reaction rate and oxidation reaction rate at equilibrium potential. It represents the corresponding current density when $\eta = 0$ and there is no net electrolysis (i.e., the intersection of the extrapolated linear portion of Tafel image with the E = equilibrium potential (E$_0$) line) [48]. Currently, j_0 is challenging to
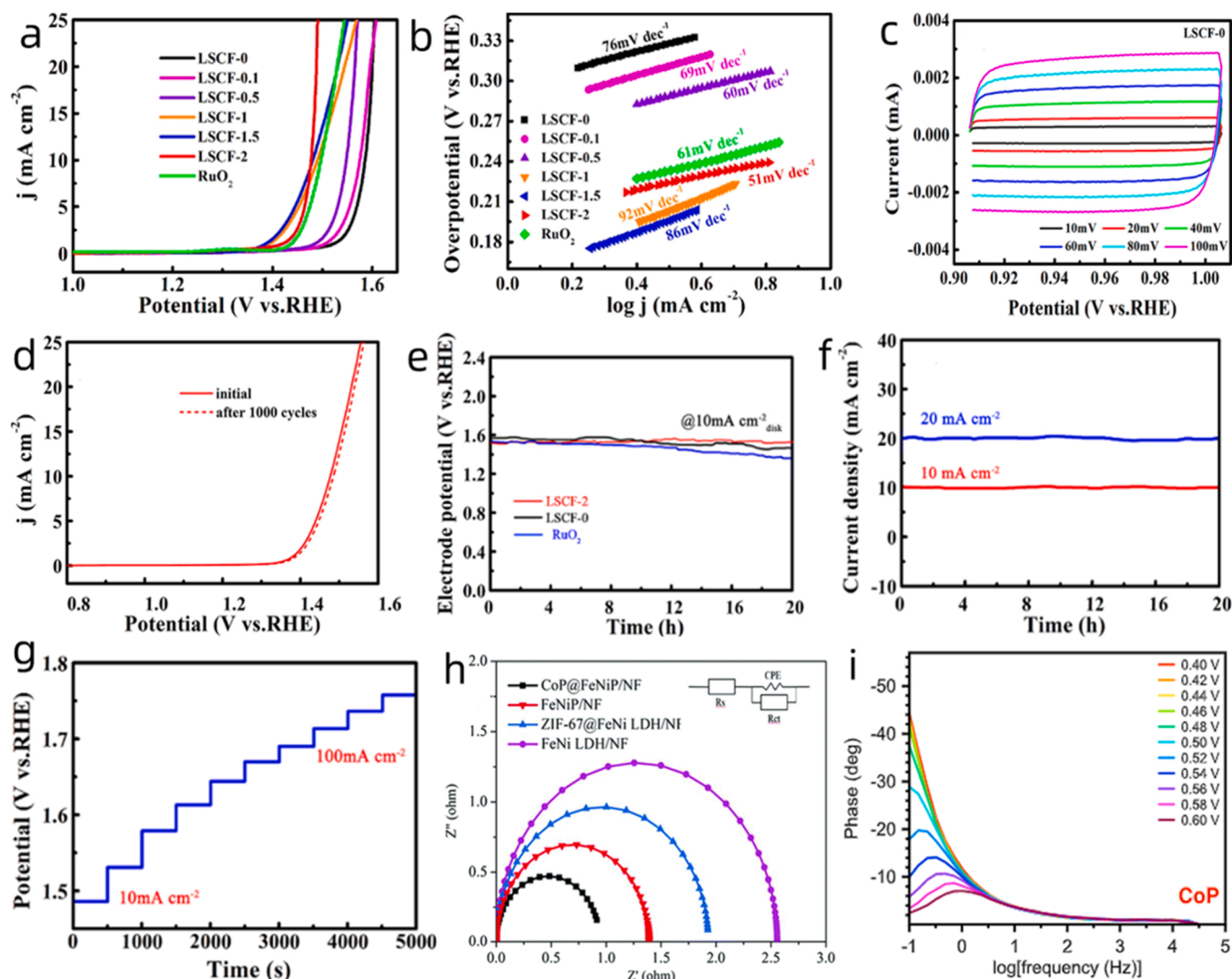
Fig. 1. (a) OER polarization curves of LSCF and commercial RuO_2 loaded on RDE (1600 rpm) in 1.0 M KOH solution. Scan rate: 5 mV s^{-1}. (b) Tafel plots of LSCF and commercial RuO_2 catalysts. (c) CV curves at different scan rates for LSCF-0. (d) Polarization curves of LSCF-2 catalyst freshly prepared and after 1000 cycles in 1.0 M KOH. (e) Chronopotentiometry curves of LSCF-0, LSCF-2, and RuO_2 catalysts for 20 h. (f) Chronoamperometric curves of LSCF-2 at different current densities. (g) Multistep chronopotential curves of LSCF-2 in 1.0 M KOH solution. (a-g) Reproduced with permission [46]. Copyright 2019, American Chemical Society. (h) EIS Nyquist plots of different electrodes recorded under OER. Reproduced with permission [63]. Copyright 2021, Royal Society of Chemistry. (i) Bode plots of CoP recorded at the various applied voltages, which are referred to SCE, for oxygen evolution reaction. Reproduced with permission [62]. Copyright 2019, American Chemical Society.

measure directly by electrochemical methods and is usually obtained by potentiodynamic polarization curves. The exchange current density is an inherent property of the electrode reaction, only related to the reaction rate constant, the electrode material, and the concentration and the temperature of reaction substance. When electrode reaction is in a non-equilibrium state in the electrochemical reaction, mainly for the kinetic characteristic, the exchange current density can be used to describe the dynamic characteristics. The electrode reaction with a larger exchange current density requires a smaller driving force (smaller current density) to react. Wang and his colleagues used the exchange current density to evaluate the OER kinetic process of the iridium electrode, j_0 is 1.99×10^{-11} A cm^{-2}, and the higher exchange current density corresponds to lower Tafel slope [48]. However, Kundu et al. believed that in the OER reaction, the size of the pH value and the difference of the catalyst would seriously affect the charge transfer rate [49]. In this case, the exchange current density is used as the evaluation standard, which is far less accurate than the overpotential at a fixed current density (such as 10 mA cm^{-2}). Suguru et al. believe that the exchange current density, like the overpotential, is also affected by the

normalization of geometric surface area and can only reflect the apparent activity [39]. Therefore, whether the exchange current density can be used to evaluate OER activity accurately remains to be discussed.

2.3. Mass activity and specific activity

The current is usually normalized by geometric surface area in mA cm^{-2}. However, it is not accurate to normalize the current density by geometric area. This method can only reflect the true area of the electrode with a smooth and flat surface. However, most electrocatalysts are nanostructures with high specific surface area and high roughness factor. Recent studies have also reported that catalysts do not have a smooth and flat surface when modified on a substrate electrode [50]. Therefore, the use of geometric area normalized current density is not accurate. It is necessary to introduce new appropriate evaluation criteria to reflect the catalytic activity of the catalyst accurately.

Mass activity (MA) represents the normalized current response of catalyst loading. The unit of MA is A g^{-1}. It avoids the influence of rough surface area, but the comparison of catalysts with different particle sizes,

densities, and morphology will cause serious deviation. In addition, if the mass of catalyst is missing during the reaction, the measured MA may also be different [39]. The intrinsic activity of electrocatalysts is better evaluated by specific activity (SA), which is determined by the actual surface area of the catalyst, usually calculated by Brunauer-Emmett-Teller (BET) isotherm and electrochemical active surface area (ECSA). The current is normalized by ECSA (j_{ECSA} = j/ECSA), and the j_{ECSA} can well reflect the intrinsic activity of catalyst.

ECSA refers to the area of material exposed to the electrolyte. Researchers can now use underpotential deposition, stripping, redox peak integral, and electric double-layer capacitance to calculate ECSA. The underpotential deposition method uses the metal surface to show the characteristic deposition of different ions to calculate ECSA, such as Pd [51]. The stripping method calculates the amount of material adsorbed on the metal surface according to the amount of charge through the interface and the number of electrons transferred by the reaction to obtain the actual surface area of the metal surface, such as CO stripping [59]. Unfortunately, the crystalline face greatly affects the former two, and it is not easy to apply to polycrystalline catalysts. The Redox peak integral method can easily find the number of active sites, but the limitations are very large, only applicable to single metal catalysts [39]. The researchers can obtain the C_{dl} value according to CV curve of non-faraday region(Fig. 1(c)). The non-faradaic region refers to the voltage range of 0.1 V based on the open circuit potential in the system. In this range, the charge and discharge curves related to the scanning rate are plotted. The redox current difference is the ordinate, the scanning speed is the abscissa, and the slope is the C_{dl} value And ECSA can be calculated from C_{dl} using Formula (5) [52].

$$ECSA = C_{dl}/C_s \tag{5}$$

where C_s is the assumed specific capacitance, typically 60 μF cm^{-2} for phosphides. It is shown that the ECSA of the same catalyst is proportional to C_{dl}. This method is applicable to almost any catalyst, but the accuracy of the calculation results is questionable. It is commonly utilized to calculate the roughness factor and study the activity difference caused by the change of electrochemical surface area and load [46,53].

2.4. Turnover frequency (TOF)

TOF can describe the rate of a catalyst catalytic reaction and the intrinsic catalytic activity of the catalyst. It refers to the number of reactions occurring per unit time and per unit active site at a given temperature, pressure, reactant ratio, and a certain degree of reaction, or is defined as the number of catalytic reactions occurring per unit time and per unit active site or the number of target products generated or the number of reactants consumed. By definition, the greater TOF value, the more active sites, and the better the catalytic activity. Yousef Haik et al. prepared a gold-supported gadolinium-doped CoB catalyst with ultrahigh TOF (1600 s^{-1}). A high TOF value reflects excellent OER activity [54].

The TOF definition focuses on active sites, indicating how quickly the catalyst can catalyze the required electrochemical reaction, reflecting the intrinsic activity of the catalyst, which is an indicator that should be focused on when evaluating OER performance. TOF is the best excellent factor to express the intrinsic activity of the catalyst, which can be used to understand further the gas escape reaction kinetics of a given catalyst. TOF is usually calculated using Eq. (6) [39].

$$TOF = \frac{jN_A}{nF\Gamma} \tag{6}$$

In the above equation, j represents the current density at a given overpotential (A cm^{-2}), N_A is the Avogadro number, and n is the number of electrons transferred to form a product molecule (for H$_2$, it is 2, for O$_2$, it is 4), and F is the Faraday constant (96 485 C), Γ is the surface concentration of active sites or the exact number of active sites of catalyst

materials in the catalytic reaction.

Although TOF can provide a critical kinetic parameter for various electrocatalysts, and there are many analytical methods for quantifying reactants and products, the difficulty in the application is to determine the number of active sites of the catalyst accurately. Unfortunately, the active sites are not thoroughly studied for most catalytic reactions. Suppose it is assumed that the electrochemically active surface area (ECSA) is approximately equal to the actual surface area (this assumption needs to be improved). In that case, ECSA can be used to calculate the exact number of active sites of TOF, but the premise is that the crystallographic information of the metal surface is known, which is very challenging. It is worth noting that some studies have pointed out that the TOF calculated by ECSA is basically close at a lower load, but the TOF calculated at too large load is quite different. This reminds us to control the range of loads when calculating TOF [55].

The second novel calculation method uses the ORR current measured in the rotating ring disk electrode (RRDE) experiment to measure the TOF of the OER on the disk simultaneously. Since the ORR current measured on the ring electrode is only due to the evolution of O$_2$ from the disk electrode, it will give TOF greater accuracy. The formula is described by Eq. (7)[56].

$$TOF = \frac{i_R}{A \times F \times n \times N_{CL} \times \Gamma} \tag{7}$$

Where i_R represents ring current density, and N_{CL} represents the collection efficiency of ring electrode [56]. Recently, Najafpour et al. used the Randles-Sevcik equation to derive a calculation formula for OER's TOF. The formula is shown in Eq. (8) [57].

$$\frac{i_c}{i_p} = \frac{n_{cat}}{0.4463np\left(\frac{k_{cat}RT}{n_pFv}\right)^{\frac{1}{2}}} \tag{8}$$

Where turnover frequency (k_{cat}) can be derived from the slope of i_c/i_p to $v^{1/2}$. This equation can be used to calculate TOF for homogeneous electrocatalysts, while for heterogeneous electrocatalysts, the calculation results not accurate [57]. It is worth noting that the calculation of TOF is to be carried out under low conversion conditions. This is because the calculation of TOF requires the use of an instantaneous reaction rate. When the conversion rate of reactants is less than 10%, the instantaneous and average reaction rates are approximately equal. Thus, using the average rate as an alternative, the data is within the error range.

2.5. Faraday Efficiency (FE)

The electrode reaction contains two critical processes: the Faraday and non-Faraday processes. The former follows Faraday's law: the amount of chemical reaction caused by current passing is proportional to the amount of electricity passing through, which refers to the process of charge transfer at the metal-solution interface to drive OER. Under certain conditions, there is no charge transfer at a given metal-solution interface due to unfavorable thermodynamic or kinetic factors. However, there is still external current flow, which will cause Faraday loss. Therefore, it is necessary to introduce the evaluation standard of Faraday efficiency. FE refers to the electron conversion efficiency of the generated product, such as O$_2$ and H$_2$, and is a crucial indicator for evaluating the selectivity of a catalyst for an electrochemical reaction. In OER, it refers to the ratio of the actual amount of oxygen generated to the theoretical amount of oxygen generated. Generally, there are two methods to determine the FE of OER. Currently, rotating ring-disk electrode (RRDE) voltammetry[58,59] and ratio method are often used to calculate FE. The former calculates FE by detecting the number of electron transfers and current values on the disk and ring. The latter is based on the ratio of actual gas production to theoretical gas production to obtain Faraday efficiency. Common methods include water gas replacement, gas chromatography, fluorescence spectroscopy, etc [60].

The formula (9) for calculating FE by RRDE voltammetry is listed as follows[59,61]:

$$FE = \frac{I_R n_D}{I_D n_R N_{CL}} \tag{9}$$

where I_R and n_R refer to the current on the ring and the number of electrons transferred, respectively; I_D and n_D refer to the current on the disk and the number of electrons transferred, respectively; N_{CL} is the collection efficiency of the RRDE used, depending on the brand. When FE is 100%, it can be considered that the energy provided by the current is not wasted on other side reactions. In addition, the other electrochemical phenomena have no current contribution to gas escape current. No matter which method is utilized, the FE values obtained by different methods should be consistent under the same experimental conditions.

2.6. Electrocatalytic stability

Electrocatalytic stability is a critical evaluation criterion in practical application, which can be used to evaluate the long-term durability of catalysts under specific conditions. In some practical applications, it is sometimes even necessary to sacrifice the activity to pursue high stability. There are usually two methods to test electrocatalytic stability. The first method is to perform a cyclic voltammetry (CV) cycle at a high scan rate. Then compare the LSV curves after the initial cycle and continuous multiple CV cycles to screen electrocatalysts with high stability and durability. This method is called the accelerated degradation (AD) test. In OER case, the number of acceleration cycles usually range from several hundred to several thousand. If the catalyst is still stable after more than 1000 cycles, it has high stability. By comparing the LSV curves before and after to check the overpotential shift at a specific current density. The smaller the offset, the higher stability. The second method is to observe the degradation of current density by chronoamperometry (*i-t* curve at constant potential) or the increase of overpotential by chronopotentiometry (*E-t* curve at a fixed current density). Whether the potential is constant in each step of multi-step chronopotentiometric curve, the stability at low and high current density can be judged, and the mass diffusion efficiency can be judged according to the height of the step. The above method is reflected in Fig.1 (d-g) [46]. In addition, after testing the electrochemical stability of catalyst, the researchers often perform scanning electron microscopy, transmission electron microscopy, and X-ray photoelectron spectroscopy on the sample to observe surface morphology, phase, and electronic valence of the sample before and after the electrochemical test to further test the stability of the sample.

2.7. Electrochemical impedance spectroscopy (EIS)

EIS is a common method to analyze the charge transfer kinetics in electrochemical reactions. EIS tests are usually performed at the voltage at which OER occurs to accurately reflect the resistance of the diffusion layer. In the OER test, R_s, R_{ct}, C_{dl}, etc. are mainly calculated according to the equivalent circuit fitting. R_s indicates that the series resistance is typically used for *iR* compensation. According to the EIS, the Nyquist diagram can be obtained as shown in Fig.1(h), which can be used to calculate the charge transfer resistance (R_{ct}). According to the low-frequency semicircle fitting in the figure, R_{ct} can be obtained. R_{ct} refers to the resistance during the transfer of electrons from the electrode to electrolyte. The smaller R_{ct} indicates faster electron transfer kinetics and higher OER catalytic activity. In addition, the Bode diagram obtained by EIS (Fig.1(i)) can be used to analyze the frequency domain at the interface or surface [62].

3. OER catalytic mechanism on metal phosphides catalysts

As we all know, the metal phosphide-based catalyst for OER is unstable under acidic conditions. As there is a large amount of OH^- in alkaline environment, the energy required to break the O-H bond is lower than that required to break two O-H bonds in acidic conditions, which is conducive to the formation of key intermediates OH* and O* during oxygen evolution reaction. Therefore, the catalyst has high OER activity under alkaline conditions [64]. On the other hand, the industrial electrolysis of water requires the catalyst to work at an appropriate pH, and the alkaline medium (electrolyte containing 25–35 wt% KOH) is less corrosive to the equipment and catalyst [65, 66]. Therefore, the OER catalyst suitable for alkaline conditions is usually prepared and its performance is tested in 1.0 M KOH. Under alkaline conditions, the overall decomposition of water is often limited by the hysteretic kinetics. Some studies believe that this is because the consumption rate of OH^- is lower than that of H^+ and the fracture of H-OH in water molecules is more difficult than that in hydrated protons [67,68]. Therefore, researchers need to prepare efficient catalysts to reduce energy barriers and accelerate reaction kinetics.
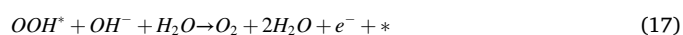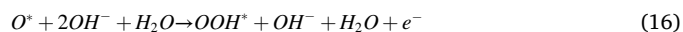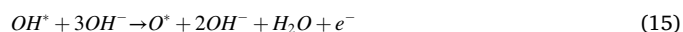
Researchers often improve the performance of electrocatalysts from two aspects, namely the number of active sites and the intrinsic activity of active sites. For the former, the number of active sites can often be increased by regulating the surface area, size and morphology of the catalyst and increasing the contact area between the catalyst and the electrolyte. For the latter, it is often necessary to explore the method to make the OER potential close to the thermodynamic limit on the basis of understanding the OER mechanism. Therefore, it is extremely necessary to summarize the widely recognized OER mechanism.

3.1. Adsorbate evolution mechanism (AEM)

The AEM is an OER mechanism widely recognized by researchers. The process of OER in acidic medium is $2H_2O \rightarrow O_2 + 4H^+ + 4e^-$, involving the following four steps [69]:

$$* + 2H_2O \rightarrow OH^* + H_2O + H^+ + e^- \tag{10}$$

$$OH^* + H_2O \rightarrow O^* + H_2O + H^+ + e^- \tag{11}$$

$$O^* + H_2O \rightarrow OOH^* + H^+ + e^- \tag{12}$$

$$OOH^* \rightarrow O_2 + H^+ + e^- + * \tag{13}$$

The process of OER in alkaline medium is $4OH^- \rightarrow O_2 + 2H_2O + 4e^-$, involving the following four steps [69]:

$$* + 4OH^- \rightarrow OH^* + 3OH^- + e^- \tag{14}$$

$$OH^* + 3OH^- \rightarrow O^* + 2OH^- + H_2O + e^- \tag{15}$$

$$O^* + 2OH^- + H_2O \rightarrow OOH^* + OH^- + H_2O + e^- \tag{16}$$

$$OOH^* + OH^- + H_2O \rightarrow O_2 + 2H_2O + e^- + * \tag{17}$$

where * represents the active site of the catalyst [70]. It is worth noting that oxygen can also be produced by direct binding of two O* ions [71]. Generally speaking, the above reaction steps are thermodynamic uphill reactions [72], and each step needs to overcome a specific energy barrier. The step with the highest energy barrier is the rate-determining step (RDS). AEM usually involves complex chemical bond breaking and formation, adsorption and desorption of intermediates on the surface and four proton coupled electron transfer (PCET) steps. OH^- firstly loses an electron and is adsorbed at the metal site of the catalyst to become adsorbed OH* . After that, OH* combines with OH^- to O* and H_2O and loses an electron. The generated O* further combines with OH^- and loses an electron to form OOH* . Finally, OOH* reacts with the fourth OH^- and loses an electron to release oxygen and H_2O, at the same time, the

active sites regenerate. The OER mechanism in acidic media is similar to that in alkaline media, except that oxygen comes from water rather than hydroxide, as shown in Fig. 2(a).

The theoretical potential of the oxygen evolution reaction in the standard state is 1.23 V, and the Gibbs free energy of the whole reaction (four steps) in the equilibrium state is 4.92 eV. Obviously, the potential of these four steps cannot be 1.23 V at the same time, because there will be a kinetic obstacle. Different from the method of measuring the overvoltage at the electrochemical workstation, the formula (18) for theoretical calculation of the overvoltage is as follows:

$$\eta_{OER} = \frac{\Delta G_{max}}{e} - 1.23 V \qquad (18)$$

Wherein, the reaction step with maximum Gibbs free energy is called potential determining step (PDS). Generally, due to the strong adsorption of O* on the catalyst surface, this step is $O^* \rightarrow OOH^*$ [73].

The essence of catalytic reaction is the process of catalyst adsorbing specific atoms to form intermediates. Therefore, the activity of OER catalyst is closely related to the adsorption energy of catalyst and intermediate produced during OER reaction. Using the generally accepted theory of adsorbate evolution mechanism (AEM), researchers can screen catalysts with high catalytic activity by optimizing the adsorption capacity (not too strong or too weak) of the catalyst for reactant intermediates [74]. Past reports have proved that during the OER process, the change of theoretical overpotential from one oxide surface to the next is related to a single descriptor representing oxygen affinity, which can be oxygen adsorption energy (ΔG_O) [75] or Relative stability of OH* and OOH* ($\Delta G_{OH} - \Delta G_{OOH}$) [76] or the difference between ΔG_O and ΔG_{OH} [77]. It can be found that if the surface oxygen binding capacity is too strong, the formation of OOH* is the main limiting factor, while if the surface oxygen binding capacity is too weak, the limiting factor is the formation of OH* . Therefore, in order to achieve the best activity, the bonding strength between the catalyst surface and the oxygenated intermediate should be moderate, which conforms to the Sabatier principle. Based on this, the Sabatier volcano diagram can be drawn, as shown in Fig. 2(b) [78]. However, AEM theory involves many complex intermediates such as O* , OH* and OOH* . The adsorption energies of these intermediates are linearly related, which is called the proportional relationship. In particular, the difference between the binding energies of OH* and OOH* is a constant value [79] ($\Delta G_{OOH} = \Delta G_{OH} + 3.2 \pm 0.2$ eV , $\Delta G_{HO^*} = a_1\Delta G_{O^*} + b_1$, $\Delta G_{HOO^*} = a_2\Delta G_{O^*} + b_2$) , This is because both of them are bound to the catalyst surface by the oxygen atom in the form of single bond, so the binding energy of the two is closely related [75]. And whether the adsorption energy of intermediates can be independently controlled means that whether high overpotential is required to drive OER. The proportional relationship limits the over potential of the catalyst to no less than 0.37 V. However, the proportional relationship also provides a direction for catalyst design. Because the over potential of OER is the difference (ΔG_O-ΔG_{OH}) /e and 3.2 V- (ΔG_O-ΔG_{OH}) /e, so when ΔG_O-ΔG_{OH} is 1.6 eV, the over potential of the catalyst can be close to 0, so it has the best activity [79].

3.2. Lattice-oxygen-mediated mechanism (LOM)

Although the use of AEM mechanism can point out the direction for researchers to quickly screen the catalyst with the best OER activity, the overpotential of the reported OER catalyst has broken through the limitation of AEM, which shows the limitation and inaccuracy of AEM theory. For example, as shown in the volcano map drawn by the AEM mechanism, SrCoO$_3$ in perovskite materials has the best activity, but the compression strain LaNiO$_3$ is superior to SrCoO$_3$ [80]. The OER activity of some oxides shows a high dependence on pH [81,82], and the oxygen produced in the OER process may come from the oxides [83,84]. These phenomena cannot be explained by AEM theory. In response to this phenomenon, Mefford et al. proposed lattice oxygen reaction mechanism (LOM) using DFT calculations to rationalize this abnormal phenomenon [85]. In addition, Grimaud et al. also provided direct evidence
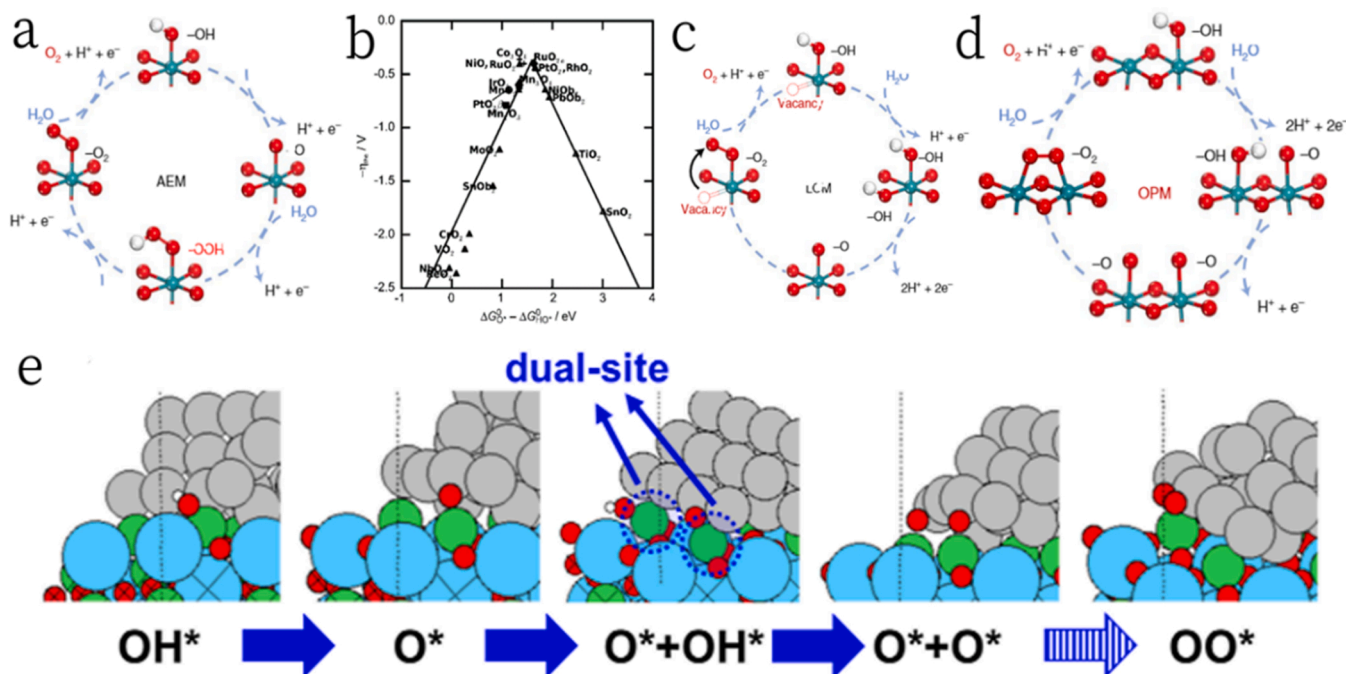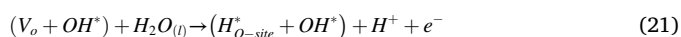

Fig. 2. (a) Schematic illustration of simplified OER mechanisms: The AEM. Reproduced with permission [88]. Copyright 2021, Nature. (b) The negative values of theoretical overpotential were plotted against the standard free energy of $\Delta G^0_{O^*}$-$\Delta G^0_{HO^*}$ step. Reproduced with permission [76]. Copyright 2011, Wiley-VCH. (c) and (d) Schematic illustration of simplified OER mechanisms: The LOM and the OPM. Reproduced with permission [88]. Copyright 2021, Nature. (e) Illustration of the dual-site mechanism. In(e), red balls are O atoms, cyan balls are La atoms, green balls are Ni atoms, gray balls are Ag atoms, and white balls are H atoms. Reproduced with permission [95]. Copyright 2021, American Chemical Society.

for LOM mechanism [86]. Lee et al. mapped the LOM mechanism, as shown in Fig. 2(c). The LOM mechanism can be expressed as follows [87]:

$$OH^* \rightarrow (V_o + OO^*) + H^+ + e^- \tag{19}$$

$$(V_o + OO^*) + H_2O_{(l)} \rightarrow O_{2(g)} + (V_o + OH^*) + H^+ + e^- \tag{20}$$

$$(V_o + OH^*) + H_2O_{(l)} \rightarrow (H^*_{O-site} + OH^*) + H^+ + e^- \tag{21}$$

$$(H^*_{O-site} + OH^*) \rightarrow OH^* + H^+ + e^- \tag{22}$$

The obvious difference between LOM mechanism and AEM mechanism is that lattice oxygen participates in the reaction of intermediates by reversibly forming surface oxygen vacancies (VO), and activated lattice oxygen participates in the OER process and promotes O-O coupling. Two M-O species are formed after the deprotonation of H_2O * at two metal sites. The binding force between two metal cations and O decreases, making it possible to directly couple two adjacent M-O species O-O (skipping $H_2O \rightarrow OOH^*$) [88]. Less thermodynamic limitation due to LOM mechanism (VO $+OO^* \rightarrow$ VO $+OH^*$ $\Delta G = 1.4 - 1.6$ eV), compared with AEM mechanism ($OH^* \rightarrow$ OOH^* $\Delta G = 3.0 - 3.1$ eV) , the catalyst following LOM mechanism is expected to obtain lower OER overpotential ($0.17 - 0.41$ eV) [89]. Recently, Piao et al. also found evidence of lattice oxygen in the prepared phosphide, suggesting the possible LOM mechanism, filling a blank in the research of phosphide [90].

However, the oxygen vacancy defects generated in LOM mechanism will also promote the dissolution of surface metal cations, eventually leading to the degradation of the catalyst and reducing the stability of the catalyst [86,89,91]. In addition, LOM has its limitations. Alexie M. Kolpak et al. believed that AEM's OER active volcano is common to all perovskite, while LOM's active volcano is closely related to the characteristics of A cation in ABO_3 [89]. A review of the differences between LOM and AEM has been reported [92], so it will not be repeated here. It is worth mentioning that one of the important differences between AEM and LOM is that the OER activity under AEM mechanism is related to pH, while the activity under LOM is not related to pH, which can be used as one of the evidences to judge the mechanism.

3.3. Oxide path mechanism (OPM)

OPM mechanism overcomes the shortcomings of AEM mechanism and LOM mechanism, that is, it does not produce oxygen defects or OOH* intermediates, and only involves O* and OH* as OER intermediates, which is expected to ensure stability while breaking the inherent proportion relationship. This mechanism allows active sites to synergistically promote water dissociation and O-O coupling to produce O_2 without lattice oxygen, as shown in Fig. 2(d). However, the occurrence of OPM mechanism has higher requirements on the geometric location of active sites than AEM and LOM mechanisms. Symmetric bimetallic sites with appropriate atomic distances are required to participate in the OPM mechanism [93,94]. Masaoka et al. reported the first OER catalyst following OPM mechanism, namely pentanuclear iron catalyst for water oxidation [93]. In addition, as shown in Fig. 2(e), the report of Eunho Lim et al. confirmed that the two site reaction mechanism of the OPM mechanism (OH*→O*→O*+OH*→O*+O*→OO*→O_2) is thermodynamically superior to the traditional AEM mechanism (OH*→O*→OOH*→O_2), reducing the theoretical limit potential by 0.7 V [95]. Lin et al. prepared a load meeting OPM design rules α-Ru electrocatalyst (Ru/MnO_2) on MnO_2 nanofibers was used as acid OER catalyst [88]. The Ru-Ru distance between atoms in Ru/MnO_2(2.9 Å) is shorter than the Ru-Ru distance between atoms in RuO_2(3.1 Å), which promotes the coupling of O-O radicals, and the presence of OOH* is not detected in the in situ detection, which proves the feasibility of the OPM mechanism in acidic media.

3.4. Species transformation of TMPs during OER process

Although it is unclear which reaction mechanism the OER process follows, a large number of experiments have proved that metal-based phosphides will transform into corresponding oxides/hydroxides during the OER process, which is the genuine active species of OER. . Under OER operation, this process may occur within one or more electrochemical scanning cycles [96]. However, the OER catalytic performance of transition metal phosphides are often superior to their corresponding oxides/hydroxides [96,97]. This may be because the phosphating helps the active metal center to convert into a metal oxide/hydroxide phase, which forms near the conductive platform and is more catalytically active than the original oxide [98]. In addition, the active species of OER can also form heterostructures with phosphate species to facilitate the transfer of electrons from phosphate to the surface, thereby facilitating the OER process [99]. Moreover, the existence of P species can dilute the density of metal atoms, weaken the M-M bond strength, and help the intermediate to couple with M [100]. It may also be that the formed core-shell structure is more conductive. The elongation of M-P bond in TMP accelerates the oxidation of metal atoms at high potentials, contributing to the formation of metal-corresponding oxide or hydroxide shells [101]. The internal TMPs core acts as a conductive scaffold for these active sites [102]. For example, the oxides formed by TMP and metal will create a TMP/MO_x core-shell structure. The TMP core acts as a catalyst center and can improve the stability of the shell. The MO_x shell accelerates the oxidation of intermediates and serves as an active site for oxygen evolution reaction [103]. Such a structure can accelerate OER catalysis [104]. It is also possible that an amorphous oxide/hydroxide phase is formed, which enhances catalytic activity [105]. Lshareef et al. prepared amorphous NiFe-OH/NiFeP as an OER catalyst, confirming that the amorphous state enhances the catalytic activity [97]. Zhao et al. found Co@CoFe highly disordered intermediates in the process of surface reconstruction of – P contribute to the formation of highly active species $Co^{III/IV}$–$Fe^{III/IV}$, while the formation of $Co^{III/IV}$–$Fe^{III/IV}$ in Co FeOOH is more difficult [106]. The stronger catalytic activity of TMPs may also come from the synergy between the formed multi-components. In short, there is no clear answer to this question at present. It is necessary for the researchers to use spectral analysis technology and calculation to further explore, fundamentally understand the OER mechanism, and point out the direction for preparing more accurate OER catalysts.

The researchers used a variety of characterization methods to confirm that the real active species of TMPs oxygen evolution reaction is the corresponding oxide/hydroxide. Xie et al.'s research show that compared with neutral electrolytes, the electrochemical activation in a harsh alkaline environment can easily break the Co-Co bond of Co_2P and promote the formation of more metal oxide/hydroxide active species on the surface [107], making the surface more hydrophilic and reducing contact resistance between the electrode and the electrolyte. HRTEM images (Fig. 3(a)) show a 2 nm amorphous cobalt oxide/cobalt hydroxide layer around the Co_2P particles after OER. EDX elemental mapping (Fig. 3(b)) further indicates that O distributes densely around the Co_2P particles. FT-EXAFS spectra (Fig. 3(c)) further confirm the formation of cobalt oxide/cobalt hydroxide. This universal activation method contributes to the OER process of the catalyst in a neutral medium. Hu et al. used Ni_2P as a Janus catalyst to study its OER performance [108]. TEM images show that nickel oxide/nickel hydroxide particles gathered around Ni_2P particles. The overpotential of the current density of 10 mA cm^{-2} in 1.0 M KOH was only 290 mV. The activity derives from the core-shell Ni_2P/NiO_x formed under OER catalysis. Xi et al. also explored the formation of active phase in the electrochemical stability test. At 1.51 V vs. RHE, the current density continued to increase with time, slightly decreased after reaching the peak value but still greater than the initial value [109]. The increase of current density was attributed to the formation of active species in the OER process.

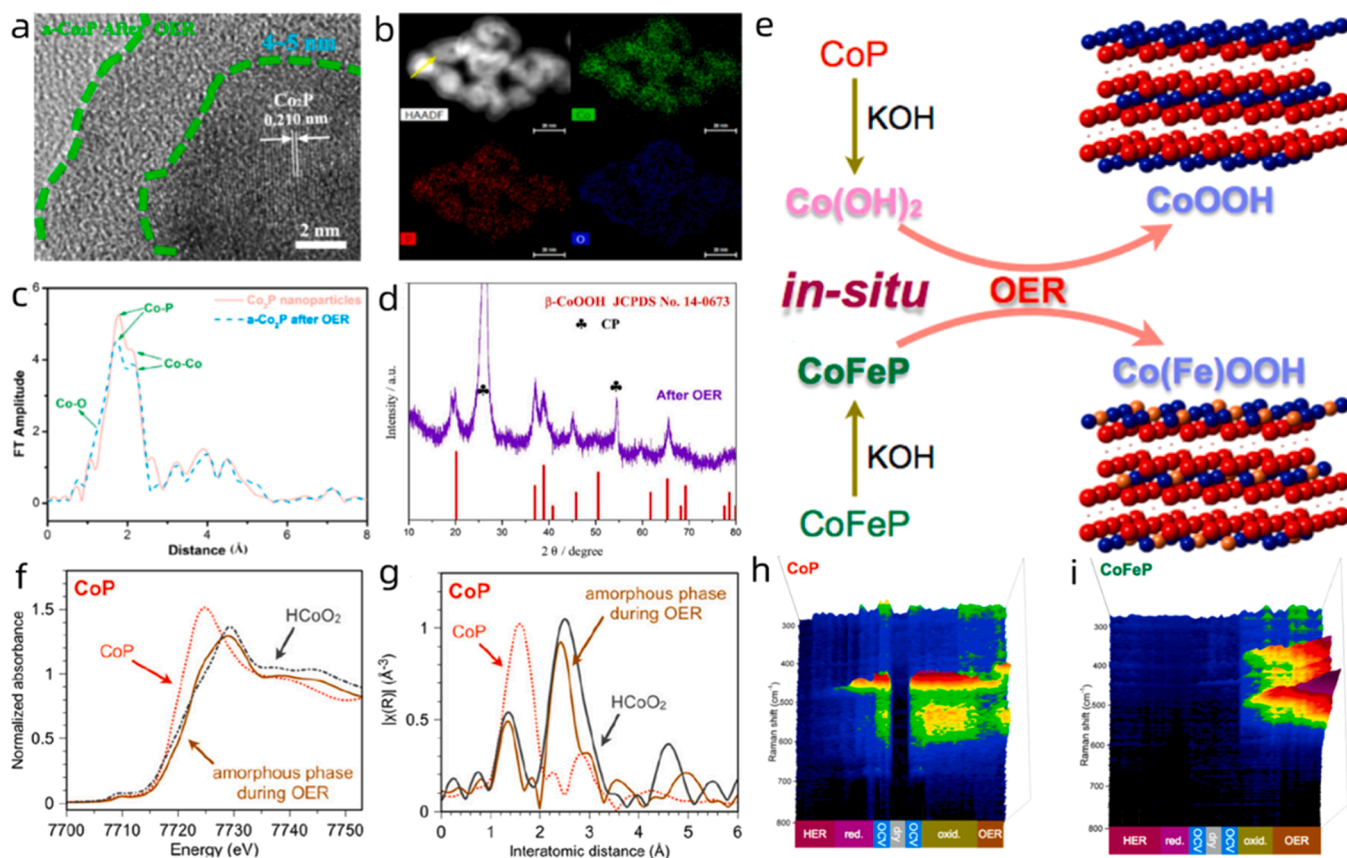It is worth mentioning that in situ techniques can be used to study the

Fig. 3. (a) HRTEM image of α-Co$_2$P after the neutral OER process. (b) HAADFSTEM and EDX elemental mapping images of α- Co$_2$P after the neutral OER process. (c) FT-EXAFS spectra at the Co K-edge of Co$_2$P nanoparticles (red) and α- Co$_2$P nanoparticles after the neural OER process (blue). (a-c) Reproduced with permission [107]. Copyright 2016, American Chemical Society. (d) XRD pattern of Cu$_{0.08}$Co$_{0.92}$P/CP after OER test. Reproduced with permission [110]. Copyright 2020, Elsevier. (e) Schematic representation of the genuine phases of cobalt-based phosphides in an electrolyte of 1.0 M KOH (aq) and during OER via in situ identification. Blue, orange, red, tin, and pink balls represent atoms for cobalt, iron, oxygen, phosphor, and hydrogen ions. In situ XAS: (f) X-ray absorption near-edge structure (XANES) of CoP during the OER. (g) Fourier-transformed extended X-ray absorption fine structure (EXAFS) of CoP for the identification of amorphous states during OER. (h, i) In situ Raman measurements for cobalt-based phosphides. Co(OH)$_2$: sharp peak at 500 cm^{-1} and a broad shoulder centered at around 580 cm^{-1}; CoOOH: sharp peak at 480 cm^{-1} and a broad shoulder centered at around 575 cm^{-1}; FeOOH in CoFeOOH: sharp peak at 425 cm^{-1} and a broad shoulder centered at around 525 cm^{-1}. (e-i) Reproduced with permission [62]. Copyright 2019, American Chemical Society.

actual situation in the catalytic process. In situ synchrotron radiation X-ray diffraction (XRD) can reveal the phase transition during the reaction. Shen et al. used XRD (Fig. 3(d)) to study the phase transition of Cu-CoP before and after OER and found that Cu-CoP converts to Cu-CoOOH, the actual active species of OER [110]. Sang Hoon Joo et al. studied the composition of cobalt oxide nanoparticles in electrochemical OER by in-situ X-ray absorption spectroscopy (XAS) [111]. They found that the composition of cobalt oxide nanoparticles in electrochemical OER is Co$_3$O$_4$ and CoOOH, and a small amount of Co(OH)$_2$, and that the Co(III) material obtained by the oxidation of Co (II) by the H$_2$O$_2$ intermediate plays a vital role in the catalytic activity of OER. On this basis, Chen et al. combined XRD with XAS to detect the genuine species of electrocatalysts in the case of surface reconstruction or entire phase conversion [62]. As shown in Fig. 3(e), they studied OER species change process of CoP and Fe-doped CoP in KOH solution to explore the genuine active species. The addition of CoP to alkaline electrolyte will produce Co(OH)$_2$, which will gradually transform into amorphous state. The XAS diagram (Fig. 3(f, g)) indicates that it is an active phase CoOOH, which is consistent with the XRD pattern. When Co(OH)$_2$ significantly converts into CoOOH, OER begins to occur, indicating that the actual species of OER in CoP is CoOOH. Impressively, the presence of Fe stabilizes the phosphating phase so that CoFeP does not convert into Co(OH)$_2$ when contacted with KOH (aq). Therefore, Fe-doped cobalt phosphide rapidly transforms into Fe-doped CoOOH during the OER, which is the active species of OER. In situ Raman spectroscopy (Fig. 3(h, i)) further confirmed that the

electroactive species of the OER process were metal oxides/hydroxides, which was consistent with the characterization results. The genuine active species of the reaction is of great significance in finding the correct reaction mechanism, carrying out appropriate theoretical calculations, and preparing genuine catalytic materials.

4. Modulation strategies for improving OER catalytic performance

Researchers often prepare highly active OER catalysts by increasing the intrinsic activity of active sites and the number of active sites/active surface area. In order to improve the intrinsic activity of active sites, this paper describes how to prepare efficient OER catalysts from four aspects: optimizing the adsorption and desorption of key intermediates, generating and optimizing vacancies in the catalyst, building multiple active sites, and promoting the formation of active phases. These four aspects correspond to the mechanism one by one; To increase the number of active sites/active surface area, strategies for constructing unique nanostructures and selecting special carriers were proposed.

4.1. Improve the intrinsic activity of active sites

4.1.1. Adjust the adsorption of key intermediates

As explained in the mechanism section, the adsorption and desorption capacity of the catalyst for oxygen-containing intermediates is an

important factor affecting RDS in the OER process. The RDS of most TMPs catalysts is O*→OOH* step. Adjusting the adsorption capacity of the catalyst for oxygen-containing intermediates is the key to breaking the scale relationship and improving OER activity. The two most commonly used strategies are element doping and building heterostructure.

4.1.1.1. Element doping to regulate the adsorption of intermediates. Element doping is an effective strategy to control the adsorption of intermediates. The researchers used DFT calculation to simulate the effect of doping elements replacing transition metals in phosphides on OER activity, and found that element doping can regulate the adsorption and desorption of intermediates, thereby reducing the energy barrier of OER process, which is due to the difference in atomic radius and electronegativity between doping elements and transition metals [112]. In addition, element doping can also create new active sites for the OER process [113].

Lu et al. innovatively designed Cr-doped FeNi-P nanoparticles encapsulated in N-doped carbon nanotubes (Cr-FeNi-P/NCN) [114]. The doping of Cr caused the binding energy of Fe 2p and Ni 2p to shift positively, which accelerated the electron transfer. Raman spectra show that the doping of Cr makes CN graphitize, and the ratio of the D band to the G band is 1.161, which indicates Cr-doping could enhance the conductivity. They performed DFT calculations to study the active source of OER process as shown in Fig. 4(a, b). The undoped FeNi-P RDS is O*→OOH* step, and the required free energy is 1.68 eV; However, after Cr doping, RDS is transformed into the formation of O_2 molecules, and the required free energy changes to 1.62 eV. Therefore, Cr doping optimizes the RDS of OER by regulating the adsorption of intermediates, resulting in excellent OER activity of Cr FeNi-P/NCN, η_{10} is 240 mV, Tafel slope is 72.36 mV dec^{-1}. Yu et al. used DFT calculation to study the influence of doped Ni on the adsorption of intermediates [115]. It is worth mentioning that the high sensitivity of metal phosphide catalysts to air often leads to surface oxidation, and XPS also shows the
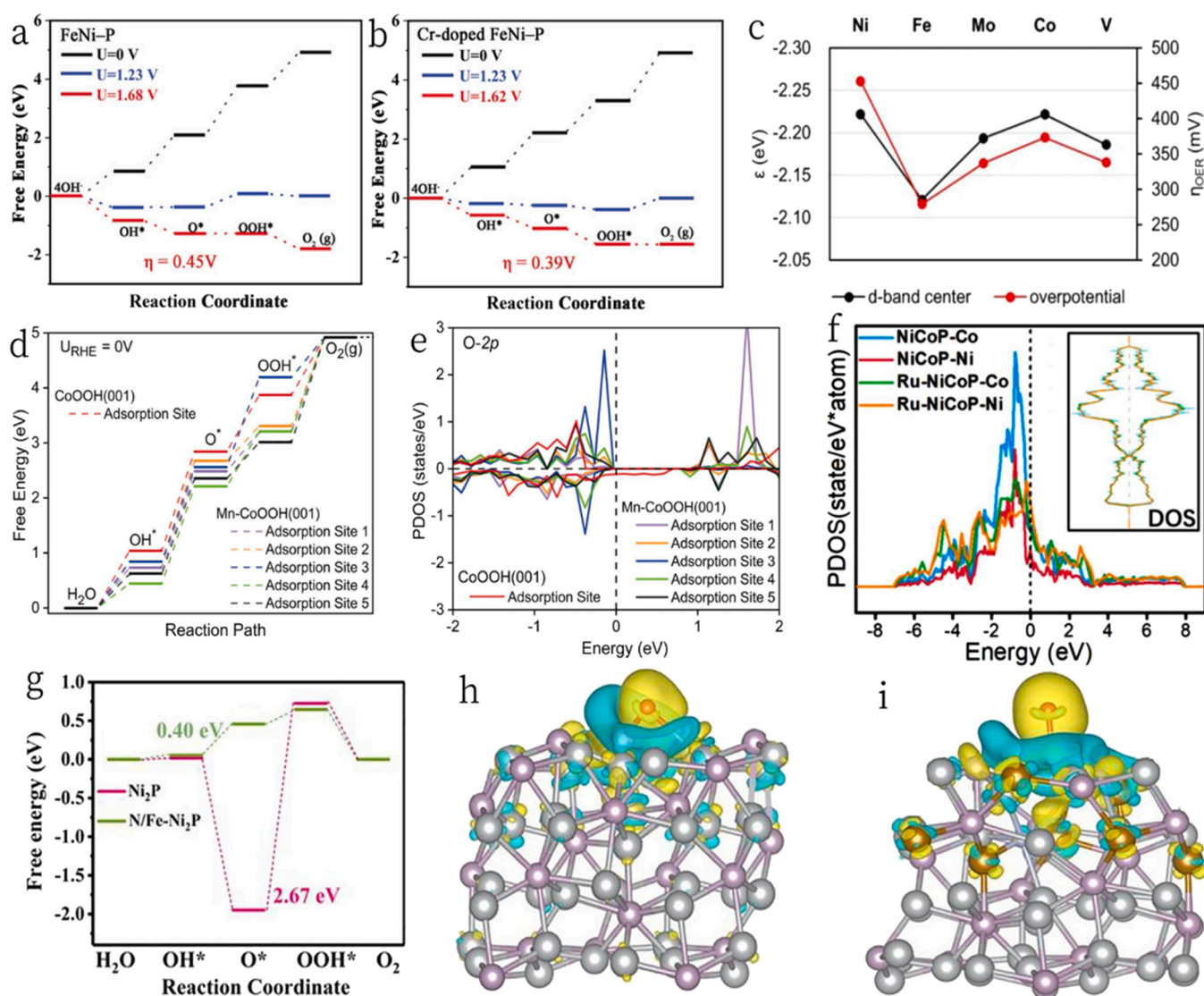

Fig. 4. . (a, b) Free energy diagrams for OER on the FeNi–P and Cr-doped FeNi–P surface, respectively. (a-b) Reproduced with permission [114]. Copyright 2019, WILEY-VCH. (c) Comparing calculated ε values and the experimental overpotentials according to dopants for OER. Reproduced with permission [121]. Copyright 2021, Elsevier. (d) Gibbs free energies of CoOOH (001) and Mn-CoOOH (001). (e) The density of projected states (PDOS) of O 2p orbital in CoOOH (001) and Mn-CoOOH (001). (d) and (e) Reproduced with permission [122]. Copyright 2021, Elsevier. (f) Calculated PDOS of special single-site on various catalysts, where the vertical dotted line indicates the Fermi energy level and the inset shows DOS of overall catalysts. Reproduced with permission [123]. Copyright 2020, Elsevier. (g) The Gibbs free-energy diagrams obtained for the alkaline OER of N/Fe-Ni$_2$P and Ni$_2$P. Differential charge density distributions of (h) Ni$_2$P and (i) N/Fe-Ni $_2$P for O* adsorption. (g-i) Reproduced with permission [127]. Copyright 2021, Elsevier.

corresponding oxidation state, so it is more appropriate to select a model with partial surface oxidation for DFT. Therefore, the author adopts the Co-P-O model and the Co-Ni-P-O model. Ni doping optimizes that the free energy of all steps , so that the energy barrier of RDS is reduced from 1.62 eV to 1.57 eV. This is attributed to that when Ni is sufficiently close to Co, Ni weakens the oxygen affinity of Co, resulting in the decrease of the binding energy of oxygen containing intermediates at the Co site [116]. Therefore, CoNi (20:1) -P @ NS has excellent OER activity, η_{10} is 209 mV, Tafel slope is 52 mV dec^{-1}. Yan et al. designed Cu doped CoP nano sheet array (Cu-CoP) to catalyze OER in 1.0 M PBS (phosphate buffer solution) [117]. The experiments confirmed that Cu-CoP was transformed into Cu-CoOOH in the OER process, and the optimization of Cu doping on the adsorption of intermediates was investigated by DFT calculation. The adsorption energy of O* on the Cu-CoOOH surface is significantly lower than that of the original CoOOH, which leads to a significant reduction in the energy barrier required for the RDS OH*→O* step of the reaction (2.0 eV→1.08 eV).

The D-band center theory is widely used to evaluate the ability of catalysts to adsorb and desorb oxygen-containing intermediates in the OER process [118,119]. The OER activity can be reflected by the D-band center. The moderate increase of the D-band center means that the OER activity is enhanced, which represents the adsorption strength of oxygen containing intermediates (OCl-OH*, O* and OOH*) [120]. Therefore, the D-band center is often used to reflect the adsorption and desorption of oxygen containing intermediates by the catalyst in DFT calculation. Yong et al. compared the OER activity of various metal doped nickel phosphide nanowires (Fe, Mo, V, Co) [121]. As shown in Fig. 4(c), DFT calculation shows the perfect consistency between the shift of D-band center after different doping elements and the overpotential under 100 mA cm^{-2}, that is, the shift of D-band center is upward, and the overpotential drops. The Fe doped NiFeP has the highest d band center 2.12 eV and the best OER activity, η_{100} is 279 mV, Tafel slope is 34 mV dec^{-1}.

Feng et al. prepared Mn doped CoP porous nano sheets as OER catalysts [122]. The experimental results show that Mn doping will cause lattice distortion, thus increasing the number of active sites. As shown in Fig. 4(d), after Mn doping, there are five different adsorption sites (Ads) for Mn CoOOH. The increase of adsorption sites is conducive to OER catalysis. The ΔG required for RDS of Ads2 and Ads5 of Mn-CoOOH is higher than that of CoOOH (001) surface, but the ΔG of RDS of Ads1, Ads3 and Ads4 is significantly reduced, which generally leads to the decrease of OER energy barrier of Mn-CoOOH, and the RDS changes from OH* → O* to O$_2$ desorption. As shown in Fig. 4(e) projected density of states (PDOS), the change of RDS is due to Mn doping increases the energy gap states of Co 3d and O 2p orbitals near the Fermi level, resulting in more electron transfer between Co and O, which makes OH* more easily adsorbed on Ads, reducing the energy barrier of OH*→O* step. The Mn-CoP-2 catalyst with the best OER activity has a η_{10} of 288 mV, and Tafel slope is 77.2 mV dec^{-1}. Tofik et al. synthesized Sn doped Ni$_5$P$_4$ catalyst (Sn-NiP) and tested the relationship between the content of Sn dopant in Ni$_5$P$_4$ and the final OER activity [98]. 3 wt% Sn is the best doping level, the catalyst needs 173, 200 and 310 mV to reach the current density of 10, 30 and 100 mA cm^{-2} respectively, and the Tafel slope is 46 mV dec^{-1}. If the concentration of Sn atom is too high, the Sn-O bond length will be prolonged, which will lead to instability of the system. The doping of Sn atoms leads to the increase of the energy density of Fermi level, which enhances the charge transfer dynamics of the syste. In addition, Sn doping increases the Fermi level density of state (DOS) and makes the D-band center closer to the Fermi level.

In addition, doping precious metals with more OER activity than Ni or Co can also optimize the adsorption of key intermediates. Chen et al. substituted a small amount of Ru for Ni in NiCoP for OER catalysis [123]. As shown in Fig. 4(f), the calculation results of PDOS show that Ru atoms show a higher density state near the Fermi level, which indicates that Ru sites promote electron transfer and make the catalyst have good conductivity [124]. In addition, Ru site is more likely to

become the catalytic site of OER, which may be due to its good adsorption of oxygen and hydrogen containing intermediates. Due to the introduction of Ru, RuNiCoP/NF catalyst has high inherent catalytic activity, η_{20} is 216 mV, η_{50} is 265 mV, η_{100} is 285 mV, Tafel slope is 84.5 mV dec^{-1}. Gong et al. loaded ultra-low Ru (0.6 wt%) doped NiFe bimetallic phosphide on NF for OER catalysis (RuNiFeP/NF) [38]. Thanks to the co-regulation of Ru and Fe, Fe species changed the electronic structure and D-band center of Ni$_2$P and optimized the adsorption of OH$^-$ and the desorption of O$_2$ [125], while Ru species optimized the adsorption free energy of H$_2$O, resulting in excellent OER activity of the catalyst, η_{10} was 179 mV, η_{100} was 227 mV, Tafel slope was 44.9 mV dec^{-1}.

The double doping strategy is often better than the single doping strategy, which is generally doped with double transition metals or non-metal and metal elements. Liu et al. used the dual doped Ni and Mn strategy to control the metal 3d to achieve the best state, and prepared Ni-Mn-FeP nano arrays for OER catalysis [126]. It can be seen from the calculated PDOS that Mn doping effectively regulates the electronic structure of Ni. Mn doping makes the 3d Ni sites spin up and down significantly forward, which is consistent with the change of binding energy shown by XPS spectrum. Therefore, the adsorption of Ni sites on oxygen containing intermediates is further enhanced, reducing the energy barrier required for O*→OOH* (4.166 eV→3.045 eV). Therefore, the doping of Mn regulates the electronic state of the doped Ni, enabling it to provide a new active site for OER process. The overpotential required to drive 10 and 100 mA cm^{-2} in 1 M KOH is only 185 mV and 205 mV respectively, and the Tafel slope is 49.4 mV dec^{-1}. Lin et al. constructed N/Fe double doped nickel phosphide (N/Fe-Ni$_2$P/Ni$_{12}$P$_5$) for OER catalysis [127]. N/Fe-Ni$_2$P/Ni$_{12}$P$_5$ only needs 217 mV and 281 mV overvoltage to drive the current of 10 mA cm^{-2} and 500 mA cm^{-2}, and the Tafel slope is 44.1 mV dec^{-1}. The excellent OER activity is attributed to the optimization of intermediate adsorption by co doping. As shown in Fig. 4(g), in the Gibbs free energy diagram, OH*→O* is very easy to occur on pure Ni$_2$P, which is a spontaneous downhill Gibbs energy change, while RDS is O*→OOH* , and the required Gibbs energy becomes 2.67 eV. As N/Fe is co-doped, the RDS of N/Fe-Ni$_2$P becomes O*→OOH* , only 0.4 eV is needed, which indicates that the adsorption of O* is promoted and RDS is optimized. The authors also built a polarized local electron configuration, as shown in Fig. 4(h, i), which shows that after co-doping the number of electrons transferred from the catalyst to O* becomes less, which confirms that co-doping weakens the interaction between the catalyst and O* , and optimizes adsorption of intermediates.

4.1.1.2. Constructing heterostructures to regulate intermediate adsorption.
When constructing heterostructures, it is a very effective strategy to use the difference of work functions between the two components to induce the redistribution of charges at the interface, thereby regulating the adsorption and desorption of key intermediates. Sun et al. constructed a metal-semiconductor Mott-Schottky heterostructure by loading Co nanoparticles on the surface of CoP$_2$ nanosheets [128]. The work function of metal Co is greater than that of semiconductor CoP$_2$, so the built-in electric field drives electrons to transfer from CoP$_2$ to Co, which creates an electron accumulation area around Co, accelerating the water decomposition. Ding et al. coupled CeO$_2$ to adjust the electron distribution at the Fe$_2$P-CoP interface, so that the electron transfers from P to Fe, O and Ce, resulting in the rise of the D-band center of Fe [129].

Cao et al. prepared Cu$_3$P-Ni$_2$P heterostructure on foam copper as OER catalyst [130]. An obvious heterogeneous interface between Cu$_3$P and Ni$_2$P can be observed in HRTEM photos. The heterostructure constructed by the OER active source promotes electron rearrangement and regulates the adsorption of intermediates. The electronic structure analysis shows that the average valence of Cu decreases while the average valence of P in the Ni$_2$P part increases, which means that 4.65 electrons migrate from Ni$_2$P to Cu$_3$P, as shown in Fig. 5(a). DFT
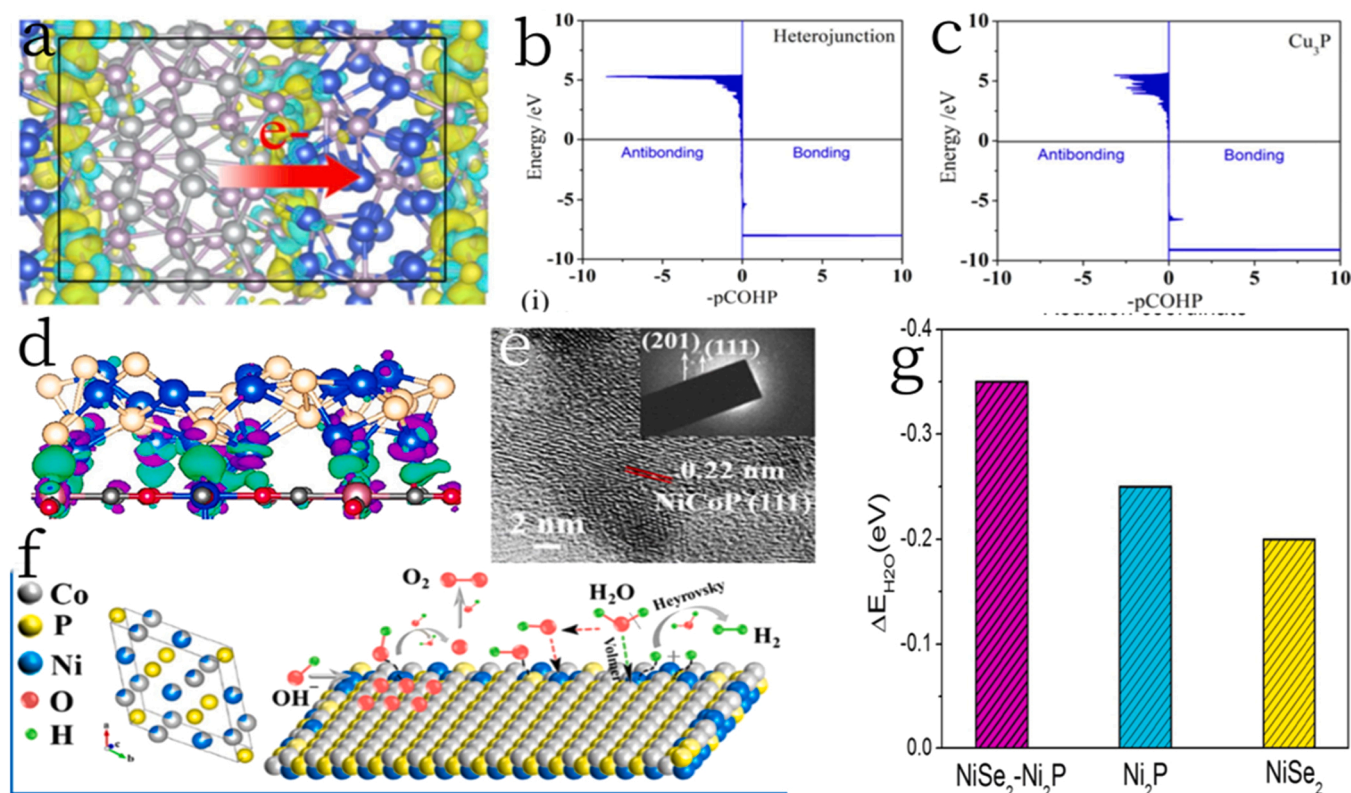
Fig. 5. (a) Schematic diagram of interfacial charge transfer. The calculated-pCOHP of (b) heterojunction and (c) Cu_3P. (a-c) Reproduced with permission [130]. Copyright 2022, Elsevier. (d) The charge-density difference of the CoP/Co-PBA complex. Cyan and purple isosurfaces indicate the gain and loss of electrons. Reproduced with permission [135]. Copyright 2021, American Chemical Society. (e) HR-TEM (SAED pattern, inset) of $Ni_{5\%}CoP$. (f) Catalytic mechanism diagram for overall water splitting at crystalline-amorphous phase interfaces. (e-f) Reproduced with permission [68]. Copyright 2021, Elsevier. (g) H_2O adsorption energy for the Ni_2P, $NiSe_2$ and $NiSe_2$-Ni_2P catalysts. Reproduced with permission [139]. Copyright 2019, Elsevier.

calculation was used to study its active source. The RDS of Cu_3P is the desorption of OH* intermediate, and the energy barrier is 0.308 eV. The RDS of Ni_2P is $H_2O^* \rightarrow H^* + OH^*$, and the energy barrier is 0.297 eV. Cu_3P/ Ni_2P @ CF combining the advantages of Cu_3P and Ni_2P, RDS is $H_2O^* \rightarrow H^* + OH^*$, and the energy barrier is 0.195 eV, even lower than the dissociation of water on Cu_3P (0.217 eV). The author also calculated the - pCOHP (Crystal organic Hamilton population) between O and H in the water molecules adsorbed on the heterostructure and Cu_3P surface to explore the adsorption of OH* on the catalyst [131]. As shown in Fig. 5(b, c), the ICOHP (Integrated COHP) of the heterostructure is 3.14, lower than Cu_3P (3.59), which means that the O-H bond adsorbed on the heterostructure is easier to break, which is consistent with the Gibbs free energy change diagram.

Zhang et al. prepared a foam nickel (NF) supported Ni_xCo_yP/Co_2P heterostructure (Ni_xCo_yP/Co_2P @ NF) as OER catalyst [132]. XPS spectra showed that the doped Mo species induced the formation of the second phase rich metal Co_2P, which has excellent water decomposition ability [133]. In addition, some Mo substitutes Co or Ni for bonding with P or N atoms, which makes the electron cloud move from P atoms to Co atoms, leading to electron rearrangement, thus optimizing the proton transfer ability of the catalyst from the P site to the active site. It is worth mentioning that the appearance of O-H and H_2O peaks in the XPS spectrum indicates the excellent hydrophilicity of the catalyst, which contributes to the adsorption of intermediates (OH*, OOH*) in the whole water decomposition process [134]. Therefore, the catalyst has excellent OER activity, with an overpotential of 352 mV and a Tafel slope of 93.5 mV dec^{-1} at a current density of 100 mA cm^{-2}.

Xu et al. creatively anchored NiCoFe-P nanoparticles in situ on porous NiCoFe PBA nanocages, and optimized the OER process of TMPs by using the strong electron absorption ability of cyano groups [135]. As

shown in Fig. 5(d), charge density analysis shows that electrons are transferred from the CoP cluster to the $Co_3[Fe(CN)_6]_2 \cdot H_2O$ substrate, reducing electrons in the cluster and promoting the $O^* \rightarrow OOH^*$ step, thus optimizing OER performance. Compared with the original CoP, PDS changes from $O^* \rightarrow OOH^*$ to $OOH^* \rightarrow O_2$, and the potential barrier changes from 2.79 eV to 2.58 eV. Therefore, the catalyst has excellent OER activity, with 223 mV overvoltage and 78 mV dec^{-1} low Tafel slope at a current density of 10 mA cm^{-2}.

When constructing heterostructures, creating a crystalline-amorphous (c-a) interface is a more effective strategy to enhance OER activity. The crystalline phase can promote electron transfer, while the amorphous phase leads to random orientation of internal atoms due to long-range disorder, resulting in a large number of unsaturated coordination atoms, which can provide abundant adsorption active sites [136, 137]. Therefore, proper adjustment of the crystallinity of the crystalline phase-amorphous phase can regulate the electronic structure and optimize the adsorption of intermediates, balance the conductivity and catalytic activity, and achieve excellent OER activity. Zhao et al. prepared a quasi-monolayer NiCoP 2D sub-nanostructure ($Ni_{5\%}CoP$) with c-a interface for OER catalysis [68]. As shown in Fig. 5(e), obvious c-a interface can be observed in HRTEM image. As shown in Fig. 5(f), the crystalline phase accelerates the adsorption of H^+, while the amorphous region accelerates the adsorption of OH$^-$, resulting in the fracture of HO-O bond at the c-a interface, thus accelerating the overall process of water decomposition. Therefore, the current density of catalyst driving 10 mA cm^{-2} only needs 259 mV, and the Tafel slope is 46 mV dec^{-1}. The author revealed the importance of amorphous materials relative to catalytic activity through mathematical models. However, a large number of current studies focused on the preparation methods and electrochemical properties of catalysts, and little attention was paid to

how to regulate the crystallinity of crystals.

Heterostructure can also be constructed by physical mixing. Bhutani and others simply mix CoP and FeP to form effective interface synergy (FeP-CoP), which can stabilize the adsorption of intermediates [138]. The difference of work function drives strong charge transfer from CoP to Fe site. DFT calculation shows that the PDS of single component is OOH*→O_2, while FeP-CoP with oxygen on the surface only needs 1.74 eV, which significantly optimizes the reaction energy barrier. Therefore, the η_{10} of the catalyst is 220 mV, the Tafel slope is 39.7 mV dec^{-1}, and the catalyst has a mass activity of 18987 A g_M^{-1} at an overvoltage of 500 mV.

In addition to regulating the adsorption of intermediates (OH*, O*, OOH*) in the OER reaction, the construction of heterostructure can also accelerate the adsorption of water and improve the ability of cracking water as a whole. Mu et al. have grown $NiSe_2$-Ni_2P heterogeneous nano fold structure on foam nickel ($NiSe_2$-Ni_2P/NF) [139]. TEM images reveal that a nano-wrinkle structure with a large number of voids, which can quickly supply electrolytes and shorten the ion diffusion distance. As shown in Fig. 5(g), the $NiSe_2$-Ni_2P heterogeneous interface has a prominent ΔE_{H_2O} value, and the adsorption energy of water (−0.35 eV) is lower than those of Ni_2P (−0.25 eV) and $NiSe_2$ (−0.2 eV), indicating that the construction of heterostructure can also accelerate the adsorption of H_2O, thus improving the overall water decomposition performance, Therefore, the overpotential of catalyst driven 50 mA cm^{-2} current density is only 220 mV, and the Tafel slope is 68 mV dec^{-1}. Similarly, Wang et al. prepared Ni_2P/NiS_2 heterostructures for OER [140]. The catalyst has an impressive electrocatalytic performance in 1.0 M KOH. The high current density overpotential of 100 mA cm^{-2} is only 320 mV, and the Tafel slope is 23 mV dec^{-1}. DFT calculation shows that the water adsorption energy (0.60 eV) on Ni_2P/NiS_2 heterostructure is far lower than Ni_2P (0.31 eV) and NiS_2 (0.15 eV). This is due to the strong coupling effect on the heterostructure, which accelerates the reaction kinetics of electrolytic water.

As mentioned above, the RDS of most TMPs is O*→OOH* . This inherent proportional relationship leads to high overpotential. On the one hand, researchers have developed DFT calculation to theoretically evaluate the adsorption capacity of catalysts for intermediates. On the other hand, the strategies of element doping and heterostructure construction are widely used to optimize the adsorption of intermediates. Double element doping in doping seems to be more promising than single atom doping, because different elements can have synergistic effects, but there are relatively few reports on double element doping. In addition, common heterostructures focus on electron rearrangement at the interface, while the creation of amorphous and crystalline heterostructures is rarely reported, and the latter also has great potential. Some catalysts prepared for optimizing adsorption and desorption of intermediates are listed in Table 1 for comparisons.

4.1.2. Create or optimize vacancy

It can be seen from the above mechanism that vacancy is the key to induce LOM mechanism, and the existence of vacancy has an important contribution to the improvement of catalyst activity. Due to imperfect atomic arrangement, the defects exist in most nanomaterials. Defects can be divided into vacancies, lattice defects, impurity atoms, intrinsic defects, etc [141]. Recent studies have found that creating defects in the crystal structure can enhance the conductivity of the catalyst. This is because the defects in the metal compounds can cause changes in the valence of elements, regulate the electronic structure and energy barriers, and enhance the charge transfer rate, thereby improving the catalytic performance [142]. In addition, the presence of defects can also optimize the adsorption of intermediates to accelerate the reaction kinetics. Therefore, researchers can study the vacancies in electrocatalysts to improve their catalytic activity.

The methods of synthesizing vacancies are often divided into physical methods and chemical methods. The common physical methods are plasma etching [143], hydrogen annealing [144], liquid stripping [145]

Table 1
Comparisons of OER catalytic activities of various TMPs.

Catalyst	Overpotential (mV@mA cm^{-2})	Tafel slope (mV dec^{-1})	iR compensation	Reference
Cr-FeNi-P/NCN	240 @ 10	72.36	with	[114]
CoNi (20:1) -P @ NS	209 @ 10	52	with	[115]
NiFeP/NF	279 @ 100	34	with	[121]
Mn-CoP	288 @ 10	77.2	95%	[122]
Sn-Ni_5P_4	310 @ 100	46	with	[98]
Ru-NiCoP	285 @ 100	84.5	with	[123]
Ru-NiFeP	227 @ 100	44.9	95%	[38]
Ni-Mn-FeP	205 @ 100	49.4	95%	[126]
N/Fe-Ni_2P/$Ni_{12}P_5$	281 @ 500	44.1	with	[127]
Ni_xCo_yP/ Co_2P @ NF (50MCNP@NF)	352 @ 100	93.5	with	[132]
NiCoFe- P @ NiCoFe	223 @ 10	78	unknown	[135]
$Ni_{5\%}CoP$	259 @ 10	46	with	[68]
FeP–CoP	220 @ 10	39.7	100%	[138]
$NiSe_2$-Ni_2P/NF	220 @ 50	68	without	[139]
Ni_2P/NiS_2	320 @ 100	23	with	[140]

Note: in the column of iR compensation, "with" represents iR compensation, "without" represents no iR compensation, the percentage represents the percentage of compensation, and "Unknown" represents no clear indication of compensation in the literature.

and heat treatment [146]. Common reduction methods include chemical reduction and element doping [142]. Gong et al. proved that oxygen plasma exposure and hydrogen annealing are effective methods to form defects [144]. The schematic diagram of oxygen plasma treatment of samples to generate vacancies is shown in Fig. 6(a-h). Oxygen plasma exposure can reduce crystal symmetry, promote lattice distortion, and produce cracks with a certain angle, thereby exposing more active sites. The schematic diagram of vacancy generation by hydrogen annealing at different temperatures is shown in Fig. 6(i-p). The hydrogen annealing method can etch the substrate surface of the catalyst to produce many triangular pores, thereby exposing more electroactive sites. In addition, Ar plasma treatment can also produce P vacancies, S vacancies, O vacancies, etc. in the compound, increasing carrier concentration and improving OER activity [143]. However, in constructing P vacancies, plasma etching usually causes damage to the device, and reduction treatment is challenging to control the number of P vacancies. Fortunately, Feng et al. developed a simple and novel phase change strategy to generate many P vacancies [147].

Ion vacancies can be divided into cation vacancies and anion vacancies. Anion vacancies can realize the excellent OER catalytic properties and are often used to reconstruct electronic states and active sites to improve surface activity of catalyst [142]. Various anion vacancies have been studied, and Feng et al. have pointed out that the Se vacancies can induce strong electronic interactions [148]. Luo et al. adjusted oxygen vacancies by designing interfaces to improve OER catalytic performance [149]. Most vacancies in metal phosphides are P vacancies or O vacancies. Interestingly, DFT calculations show that the presence of P_v can induce the formation of oxygen defects after long-term OER tests [150]. The dissolution of surface P atoms can lead to the lattice distortion, which may produce a large number of oxygen defects. The existence of O vacancy is the key of LOM mechanism, which is helpful to optimize the binding energy of intermediate active substances, and it is an important source to significantly improve the OER catalytic activity of oxygenated compounds. In addition to P_V, oxygen vacancy defects have also been shown to shorten the distance of mass transfer, thereby increasing OER activity [151,152]. Oxygen vacancies are beneficial to expose active sites and accelerate kinetic process, and the nearby delocalized electrons easily enter the conduction band to improve conductivity and optimize adsorption free energy of OER intermediates [153].
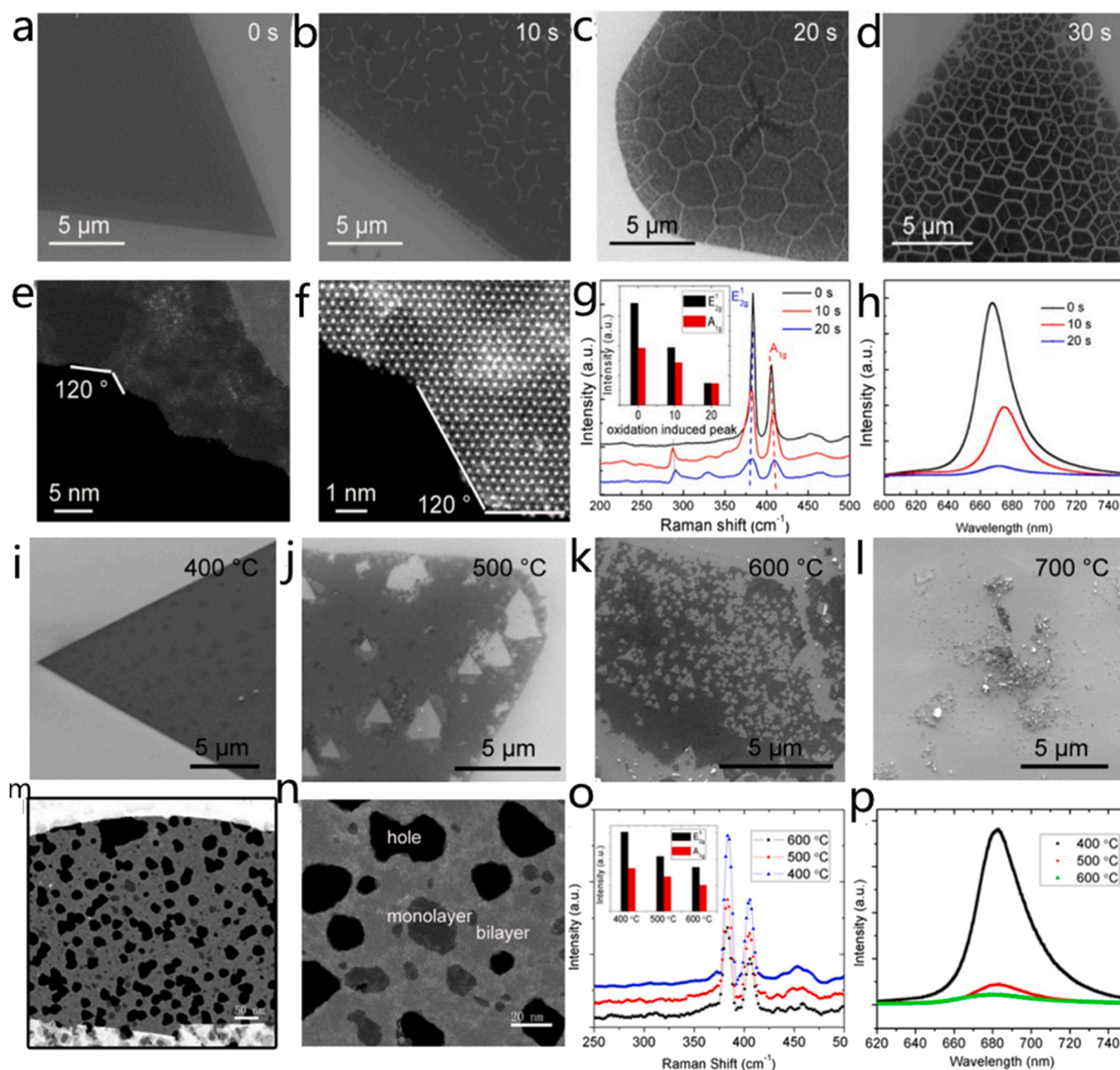
Fig. 6. (a-h) Morphology and structure characterizations of MoS$_2$ grown by CVD with oxygen plasma treatment. (i-p) Structure characterizations of MoS$_2$ grown by CVD with hydrogen treatment at different temperatures. (a-p) Reproduced with permission [144]. Copyright 2016, American Chemical Society.

4.1.2.1. P vacancy. The researchers explored various methods to prepare TMPs rich in P-vacancy as OER catalysts. Li et al. used Ar plasma treatment to adjust the P vacancy in Co$_{0.68}$Fe$_{0.32}$P, and prepared samples treated for 30 min, 60 min and 90 min, respectively [143]. The content of phosphorus vacancy increased with the increase of treatment time. Phosphides treated by argon plasma are more easily occupied by oxygen in the air, and the total surface oxygen content increases with increasing phosphorus vacancies. Among various catalyst samples, Co$_{0.68}$Fe$_{0.32}$P-60 has the most surface oxygen (surface oxygen leads to abnormal electron loss of surface Co/Fe ions), with a η_{10} of 259 mV and a Tafel slope of 35.5 mV dec^{-1} in 1 M KOH, better than commercially available IrO$_2$.

On this basis, Ren and colleagues prepared Pv-rich CoP nanorods using a simple NaBH$_4$ reduction method as shown in Fig. 7(a) [142]. The presence of P vacancies can optimize the electronic structure, regulate the energy barriers of intermediates and reactants, and promote the

formation of phosphates to improve OER activity. It is worth mentioning that the experiment also studied the effect of the number of P vacancies on the catalytic activity. The number of P vacancies was controlled by controlling reduction time. In addition, CoP-B with different vacancy concentrations was prepared with different reduction time, which was proved by EPR in Fig. 7(b). Obviously, the longer the reduction time, the stronger the response at g= 2.01. The OER performance of the catalysts was tested in 1.0 M KOH, and the LSV curve is shown in Fig. 7(c). The results show that if the number of Pv is too large, it will lead to the loss of highly active sites during the OER process. Therefore, the number of Pv should be controlled during the preparation process. Among them, CoP-B1 has the best OER catalytic performance with η_{10} of 297 mV, Tafel slope of 58.1 mV dec^{-1} and C_{dl} value of 0.051 mF cm^{-2}, which is superior to most other CoP-based catalysts.

Feng et al. prepared Fe-doped Ni$_5$P$_4$ nanosheet arrays with a large number of Pv by using a novel phase transition strategy [154]. EPR
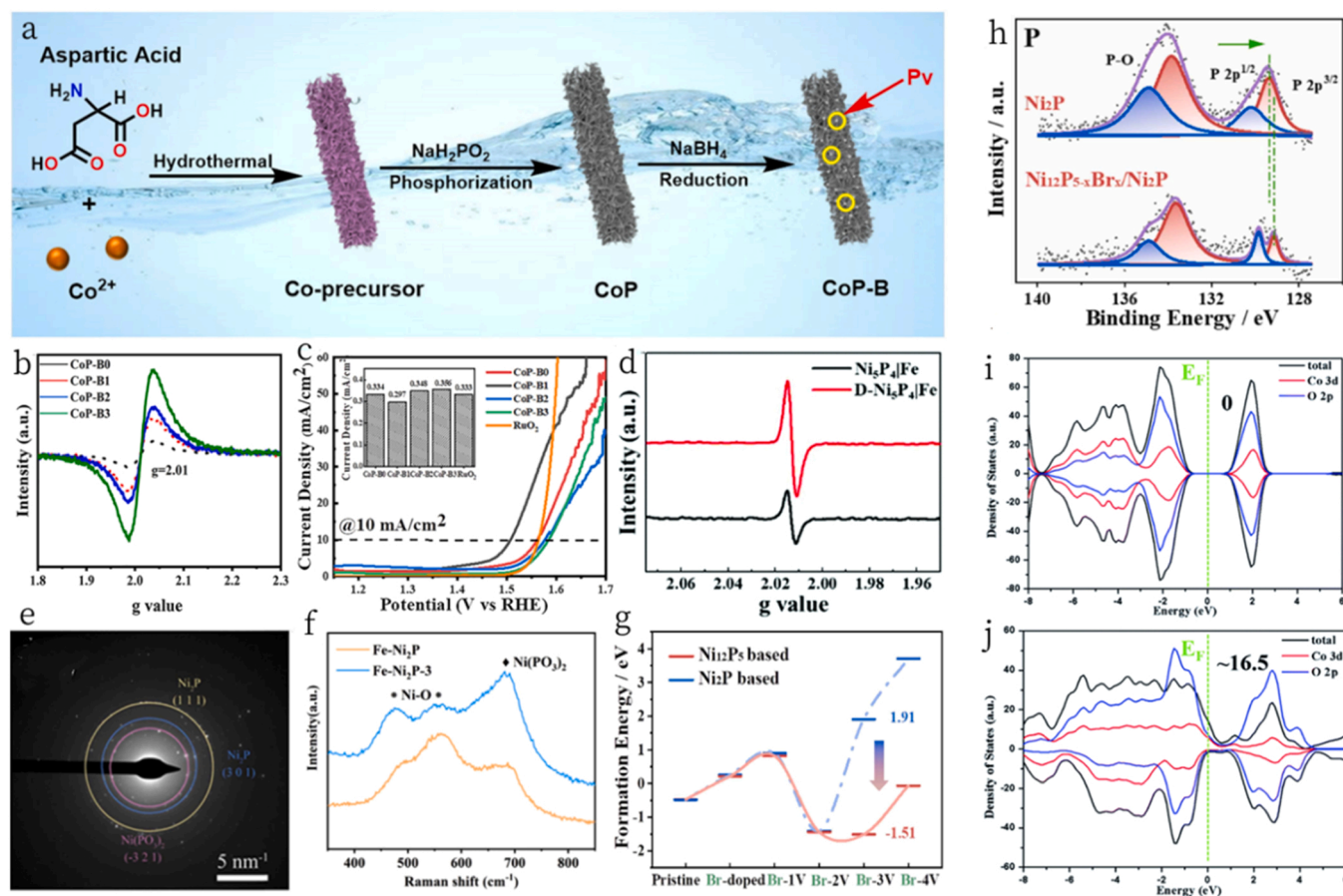
Fig. 7. (a) Schematic diagram illustrating the synthesis process of CoP-B and the significant role of P vacancies in electrocatalytic OER. (b) EPR spectra of CoP-B by different reduction time; (c) OER polarization curves in 1 M KOH (sweep rate: 2 mV s-1) of CoP-B by different reduction time (inset of required overpotentials to achieve 10 mA cm-2). (a-c) Reproduced with permission [142]. Copyright 2021, Elsevier. (d) EPR spectra of $Ni_5P_4|Fe$ and $D-Ni_5P_4|Fe$. Reproduced with permission [154]. Copyright 2020, Royal Society of Chemistry. (e) SAED pattern of $Fe-Ni_2P-3$. (f) Raman spectra of $Fe-Ni_2P$ and $Fe-Ni_2P-3$. (e-f) Reproduced with permission [156]. Copyright 2022, Elsevier. (g) Formation energies of Ni_2P and $Ni_{12}P_5$ base configurations of Pristine, Br-doped, Br-doped with 1 P vacancy (1 V), 2 P vacancies (2 V), 3 P vacancies (3 V), and 4 P vacancies (4 V). (h) High-resolution XPS spectra of P 2p of Ni_2P NS and $Ni_{12}P_{5-x}Br_x/Ni_2P$ NS. (g-h) Reproduced with permission [157]. Copyright 2022, Elsevier. DOSs of (i) β-CoOOH bulk and (j) thin shell of the (101) facet-exposed β-CoOOH with oxygen defects. The green dash lines represent the position of the Fermi energy level. (i-j) Reproduced with permission [150]. Copyright 2018, Royal Society of Chemistry.

spectra (Fig. 7(d)) confirmed that a simple transition from $NiSe_2$ to Ni_5P_4 could induce a large number of P vacancies that can accelerate the adsorption of OH⁻ species and the electron transfer of step $OH^* \rightarrow O^* + H + e^-$. The Tafel slope close to 40 mV dec⁻¹ (45.7 mV dec⁻¹) indicates that the second electron transfer step is RDS. In addition, the special structure of more edge active sites can be exposed, and the synergistic effect of highly conductive substrates and P vacancies makes it have higher ECSA, lower R_{ct}, excellent stability, and excellent OER activity (217.3 mV @ 10 mA cm⁻²). As mentioned above, the method of element doping can also generate vacancies, and the heterogeneous cation doping can also expose more active sites and regulate the interaction of electrons. Therefore, element doping and vacancy engineering should bring excellent OER catalytic performance. Feng et al. combined cation doping with P vacancy to prepare V-doped NiCoP OER catalyst with P vacancy by Ar plasma engineering (Ar-NiCoP | V) [155]. Due to the enhancement of P vacancy on the V doping effect, the number of active sites and the electron transport rate increase. In addition, EPR images also confirmed that the signal of Ar-NiCoP | V at g= 2.005 was greatly enhanced after V doping, which indicating the doping of V can induce the generation of lattice vacancies. At a current density of 10 mA cm⁻², the overpotential of Ar-NiCoP | V in 1.0 M KOH is 246 mV, and the Tafel slope is 70.4 mV dec⁻¹, indicating Ar-NiCoP | V is an excellent OER catalyst.

Liu et al. combined Fe doping with P vacancies and used O_2 plasma

physical bombardment to generate P vacancies on Fe-doped Ni_2P samples [156]. It has been described above that Fe doping can enhance conductivity, regulate the electronic structure of active sites, and reduce the adsorption energy of intermediates in the OER process. On the other hand, the sputtered P vacancies can react with highly active oxides in the plasma atmosphere to form phosphate species, promoting charge transfer and water adsorption. SAED patterns in Fig. 7(e) and Raman spectra in Fig. 7(f) both confirmed the presence of phosphate species. Due to the synergistic effect of P vacancies and Fe doping, the Fe-doped Ni_2P sample has excellent OER performance with a η_{50} of 207 mV, a η_{100} of 218 mV, and a Tafel slope of 45 mV dec⁻¹. Surprisingly, Xu et al. used Br doping to induce the formation of P-poor $Ni_{12}P_5$ phase and P vacancies ($Ni_{12}P_{5-x}Br_x/Ni_2P$ NS) [157]. Simulation calculations (Fig. 7(g)) show that the doping of Br changes the formation energy of nickel phosphide to form a $Ni_{12}P_5$ phase containing P vacancies. EPR spectra show that P vacancies change the spin state of Ni, increasing unpaired electrons. At the same time, the XPS spectrum (Fig. 7(h)) shows that the binding energy of P $2p_{3/2}$ shifts negatively, indicating that more electrons are transferred from Ni to P, which increases the electron density of P. Catalysts with different P vacancy contents can be obtained by controlling different heat treatment temperatures. Among them, the sample obtained at 350 °C has an extraordinary OER performance, with a η_{10} of 155 mV, a current density of 1 A cm⁻² at 534 mV, a Tafel slope of 56 mV dec⁻¹, and an ECSA of 1031 cm².

It is worth mentioning that for Ni_2P/Cu_3P nano sheets prepared by Lin et al., EPR characterizes the existence of P vacancies and promotes the generation of oxygen vacancies. The synergistic effect of O vacancies and interfaces leads to rich active sites and rapid electron transfer, which is proved by C_{dl} and R_{ct} [158]. Ni_2P/Cu_3P has excellent OER performance in 1.0 M KOH. The current density of 10 mA cm^{-2} only requires 262 mV overvoltage and 78.1 mV dec^{-1} Tafel slope. Zhou et al. prepared 3D reduced porous cobalt phosphide nano powder (R-CoP$_x$/rGO (O)) with rich P-vacancies (O in parentheses indicates that the catalyst is electrochemical oxidized) [150]. P vacancy leads to oxygen vacancy and lattice distortion of active species β-CoOOH growing in OER process, exposing more active sites. The existence of vacancy can make β-CoOOH coordination is more unsaturated. The DOS of the β-CoOOH shell with oxygen vacancies is closer to the Fermi level than the original shell, indicating a higher conductivity as shown in Fig. 7(i, j). The η_{10} is 268 mV, Tafel slope is 103 mV dec^{-1}. Interestingly, Raman spectroscopy tests confirmed the importance of many defects in improving OER performance by using N-doped carbon to protect catalyst surface. It can be seen from the above examples that the existence of P-vacancy can induce the generation of oxygen vacancy to improve the catalytic activity of OER. It is reasonable to speculate that the direct generation of oxygen vacancy may have better activity.

4.1.2.2. O vacancy. A large number of studies have explored the preparation of O vacancy rich TMPs as OER catalysts One of the strategies commonly used by researchers is to combine doping and O vacancy to improve OER performance by utilizing the synergistic effect of the two. Li et al. designed ultrathin Fe-doped $Ni_5P_4/Ni(OH)_2$ (Fe-Ni$_5P_4$/NiFeOH-350) nanosheets with oxygen vacancies [159]. After phosphating, the peak area of oxygen vacancies increases greatly, which fully reflects that the reaction of H_2/PH_3 with lattice oxygen during phosphating produces rich oxygen vacancies. The presence of oxygen vacancies promotes the adsorption of hydroxyl ions in the OER process, making the catalyst highly hydrophilic and conducive to the exposure of active sites. EPR signals also confirm the formation of oxygen vacancies. DFT calculation shows that when Fe replaces Ni, the D-band center of Ni_5P_4 continues to move forward, which optimizes the binding ability of

intermediates and promotes OER dynamics. The synergistic effect of Fe doping and oxygen vacancies endows the catalyst with excellent OER activity, η_{10} is only 221 mV, Tafel slope is only 35 mV dec^{-1}, R_{ct} is 0.9 Ω, and it has a durability of 80 h at a current density of 10 mA cm^{-2}.

Shao et al. prepared NiCo/NiCoP hybrids by combining N doping with oxygen vacancies [160]. In the XPS spectrum the peak at 853.0 eV in the Ni 2p spectrum is attributed to Ni(0) species, and the binding energy of Ni shifts positively by 0.2 eV, indicating that Ni provides electron to create vacancies. In the O 1 s diagram (Fig. 8(a)), O_3 is attributed to oxygen vacancies. Obviously, the peak area of oxygen vacancies is the largest, indicating that the catalyst contains many oxygen vacancies, which can improve the conductivity and accelerate redox kinetics. The η_{10} of this catalyst is 290 mV, Tafel slope is 55 mV dec^{-1}, TOF is 0.034 s^{-1} at 350 mV, and it has a high active surface area and high conductivity. In addition, Shao et al. also designed N-doped oxygen-vacancy-rich Ni-Co-based nitride phosphide hybrids (NCNP), where N doping forms N-M bonds and improves OER activity [153]. The presence of oxygen vacancies can reduce the barrier from O* to OOH*, which is only 1.47 eV, much lower than the perfect surface (1.92 eV), thereby improving OER activity, as shown in Fig. 8(b). Its η_{10} is 290 mV, Tafel slope is 41 mV dec^{-1}. C_{dl} and EIS tests show that it has abundant accessible active sites and fast charge transfer ability.

In addition to the combination of doping and vacancy, coupling in situ generated materials with O vacancy with TMPs is also one of the strategies to enhance the OER activity of TMPs. CeO_2 has a large number of oxygen vacancies and is a good candidate material. The close contact interface between CeO_2 and TMP can also take advantage of the advantages of TMP to promote the formation of active species. Gao et al. did such work. They designed 1.4-CeO$_2$/NiCoP/NF ('1.4' refers to 0.014 g Ce(NO$_3$)$_2$·6 H$_2$O) with a tight CeO$_2$/NiCoP interface [161]. Oxygen vacancies can weaken the absorption of O* by active sites, generate OOH*, and promote the release of oxygen. The strong interaction between interfaces and oxygen vacancies jointly promotes the transfer of OER intermediates and electron transfer. The η_{10} of 1.4-CeO$_2$/NiCoP/NF is 249 mV, the Tafel slope is 77.2 mV dec^{-1}, and the R_{ct} is 3.4 Ω, which are better than other samples. It is worth mentioning that experiments show that too much CeO$_2$ will reduce the electron
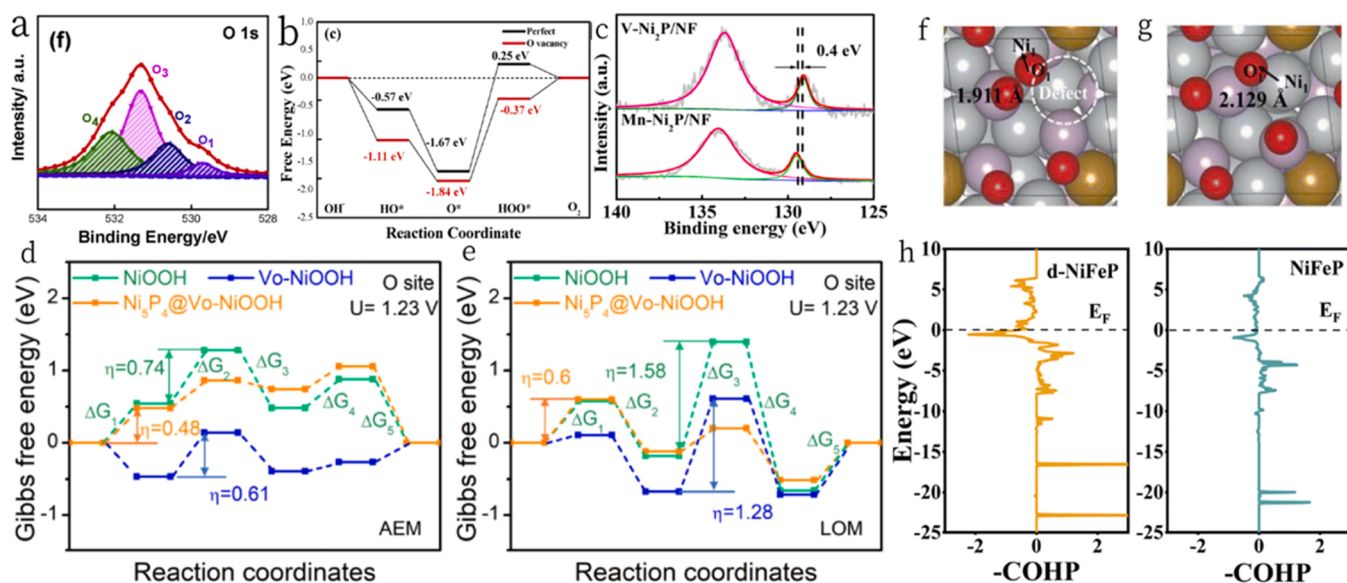

Fig. 8. (a) XPS spectrum of O 1s in NiCo/NiCoP hybrid. Reproduced with permission [160]. Copyright 2019, Elsevier. (b) Gibbs free energies diagram for the OER process catalyzed by various catalysts. Reproduced with permission [153]. Copyright 2019, Elsevier. (c) High-resolution P 2p XPS spectra of V-Ni$_2$P/NF and Mn-Ni$_2$P/NF. Reproduced with permission [163]. Copyright 2020, Elsevier. Free energies of OER steps via mechanisms of AEM (d) and LOM (e) on NiOOH, V_o-NiOOH and Ni$_5$P$_4$@V_o-NiOOH at U= 1.23 V, respectively. (d) and (e) Reproduced with permission [162]. Copyright 2021, Elsevier. [163] (f) d-NiFeP and (g) NiFeP pre-catalyst surface oxidation models. (h) COHP of d-NiFeP-NiFeP and NiFeP. (f-h) Reproduced with permission [164]. Copyright 2022, Royal Society of Chemistry.

transfer rate and affect the exposure of active sites. Therefore, when designing catalyst, the amount of precursor should be reasonably controlled.

Similarly, NiOOH formed in situ can generate abundant oxygen vacancies in situ during OER. Based on this, Wang et al. constructed a core-shell rich in oxygen vacancies Ni_5P_4 @NiOOH heterostructure nanosheet array [164]. The presence of oxygen vacancies can well activate the active NiOO* material and promote the formation of stubborn O-O bonds. DFT Calculation Reveals the Contribution of Oxygen Vacancies to OER Catalysis. The theoretical overpotentials of the catalyst under the adsorbate evolution mechanism (AEM) and lattice oxygen oxidation mechanism (LOM) were calculated, respectively. As shown in Fig. 8(d, e), it is concluded that the Ni_5P_4 @NiOOH has a lower theoretical overpotential in the AEM pathway, and in the AEM pathway the overpotential at a current density of 10 mA cm^{-2} is 370 mV. Interestingly, the η_{50} of Ni_5P_4 @NiOOH is only 273 mV, indicating a breakthrough in the AEM theoretical overpotential limit. The Ni_5P_4@NiOOH is an ideal OER catalyst with a small Tafel slope of 62 mV dec^{-1}, a big C_{dl} value of 10.0 mF cm^{-2}, and excellent stability.

4.1.2.3. Cation vacancy and multi-vacancy. In terms of cation vacancies, Zhang's team designed Mn-doped nickel phosphide, and a large number of cation vacancies were generated after removing Mn during the acid etching process (V-Ni_2P/N) [163]. The XPS spectrum in Fig. 8(c) shows that, compared with Mn-Ni_2P/NF, the binding energy of V-Ni_2P/NF moves 0.4 eV to the low energy side, indicating that the existence of cation vacancies forms a large number of negatively charged P^{x-}, which adjusts the electronic structure. The existence of cation vacancies causes the electronic dislocation of Ni active sites, which can promote the adsorption of intermediates and reduce the energy barrier of H_2O adsorption. The electron density of Fermi level of V-Ni_2P/N is much higher than that of Mn-Ni_2P and Ni_2P, indicating that cation vacancies can optimize electronic structure and improve the conductivity, which plays a vital role in improving electrocatalytic activity. The OER performance was tested in 1.0 M KOH, and V-Ni_2P/N showed excellent OER activity with η_{10} and Tafel slopes of 250 mV and 81 mV dec^{-1}, respectively.

Chen et al. prepared Zn-NiFeP/CC and further selectively etched Zn atoms to generate a large number of cation vacancies (d-NiFeP/CC) [164]. Etch Zn with the same radius as the Ni atom, and Ni around the Zn atom is more likely to generate vacancies than Fe. The formation of active phase NiOOH can be observed by Raman spectroscopy, which is attributed to the contribution of cation vacancies. As shown in Fig. 8(f, g), the Ni-O bond near the defect in d-NiFeP/CC becomes shorter, indicating that the unstable Ni atom has stronger ability to couple with O atom. The quantitative analysis of iCOHP (Fig. 8(h)) shows that the presence of defects enhances the Ni-O bond. Therefore, the introduction of cation defects makes Ni more oxygenophilic and accelerates the oxidation to form NiOOH. Therefore, the current of 10 mA cm^{-2} driven by d-NiFeP/CC only requires an overvoltage of 185 mV, and the Tafel slope is 24.56 mV dec^{-1}. In addition, Peng et al. also pointed out that the cation vacancy can enhance the long-term stability of the catalyst [165]. Unfortunately, compared with anion vacancies, more energy is needed to form cation vacancies and ideal Fermi energy levels, which can be used for water splitting to produce hydrogen, which greatly limits the development of cation vacancies [166]. Therefore, there is still little research on cation vacancy, and more cation vacancy types need to be studied in the future.

Introducing a single defect can improve the catalytic activity, so the reasonable introduction of double defects and synergistic effects may achieve high catalytic activity that a single defect cannot achieve. The introduction of Se and Mo vacancies by Gao et al. activated the electroactive sites on the basal and edge of $MoSe_2$ [167]. Wang et al. fabricated ultrathin LDH nanosheets with O, Fe, and Co vacancies by Ar plasma etching [168]. Oxygen vacancies promote the adsorption of OER

intermediates, cation vacancies adjust the atomic environment of Co, leading to electron and orbital redistribution. In addition, Lee et al. synthesized ultrathin nanosheets with oxygen and manganese double vacancies by a clever method [169]. It is confirmed that oxygen vacancies promote water destabilisation, and the introduction of Mn vacancies (V_{Mn}) can modulate the electronic state to give half-metallic properties and enhance the conductivity, resulting in the catalytic activity far superior to single vacancies. The strategy of constructing double vacancies has important inspiration and broad prospects for the preparation of TMP catalysts with excellent OER catalytic activity, but unfortunately, there are too few related reports and further research is needed.

It can be seen from the above that the vacancies in TMPs are mainly P-vacancies, which can optimize the OER activity of the catalyst Moreover, the existence of P vacancy can induce the formation of O vacancy, and O vacancy also seems to show better performance than P vacancy. Therefore, directly generating O vacancy in TMPs or coupling TMPs with materials rich in O vacancy (chemical binding or physical binding) may produce excellent OER activity, which has also been reported in the literature However, more vacancies, such as Se vacancy, cation vacancy and multi vacancy, have been studied less in TMPs, and the direct evidence and mechanism that O vacancy is superior to P vacancy have not been clarified, which still needs further exploration by researchers. Some catalysts prepared for vacancy generation and optimization are listed in Table 2 for comparisons.

4.1.3. Construction of double active sites

As mentioned in the mechanism part, the key of the OPM mechanism is to construct the polymetallic active sites, overcome the shortcomings of monomers and pursue the "1 + 1 > 2" catalytic activity by using the synergy of the active sites. Generally, different active sites play different roles in OER catalysis. The common active phase CoOOH or NiOOH acts as the adsorption of oxygen containing intermediates, while another active site often plays a role in accelerating water adsorption or promoting the release of O_2. Wen et al. synthesized CeO_2-$NiCoP_x$ on NCF substrate by coupling CeO_2 with $NiCoP_x$ [170]. DFT calculation shows that the doping of CeO_2 improves the electronic density of states of the material and has faster electron transfer capability. CeO_2 wrapped on the surface of $NiCoP_x$ promotes the dissociation and adsorption of water

Table 2

Comparisons of OER catalytic activities of various TMPs.

Catalyst	Overpotential (mV@mA cm^{-2})	Tafel slope (mV dec^{-1})	iR compensation	reference
$Co_{0.68}Fe_{0.32}P$-60	259 @ 10	35.5	with	[143]
CoP-B1	297 @ 10	58.1	without	[142]
D-Fe-Ni_5P_4	217.3 @ 10	45.7	with	[154]
Ar-NiCoP|V	246 @ 10	70.4	with	[155]
Fe-Ni_2P	218 @ 100	45	with	[156]
$Ni_{12}P_{5-x}Br_x$/ Ni_2P NS	155 @ 10	56	with	[157]
A-Ni_2P/Cu_3P	262 @ 10	78.1	with	[158]
R-CoP_x/rGO (O)	268 @ 10	103	unknown	[150]
Fe-Ni_5P_4/ NiFeOH-350	221 @ 10	35	without	[159]
NiCo/NiCoP	290 @ 10	55	with	[160]
NCNP	290 @ 10	41	unknown	[153]
1.4-CeO_2/ NiCoP/NF	249 @ 10	77.2	95%	[161]
Ni_5P_4 @NiOOH	273 @ 50	62	with	[162]
V-Ni_2P/N	250 @ 10	81	with	[163]
D-NiFeP/CC	185 @ 10	24.56	without	[164]

Note: in the column of iR compensation, "with" represents iR compensation, "without" represents no iR compensation, the percentage represents the percentage of compensation, and "Unknown" represents no clear indication of compensation in the literature.

and is the active site of water adsorption. As shown in Fig. 9(a), the energy barrier required for the O*→OOH* step of CeO₂-NiCoP is only 0.06 eV, far lower than other samples (CeO₂-Co₂P: 1.28 eV), indicating that Ni is the active center of the OER process, accelerating the conversion of O*→OOH* . Therefore, CeO₂ accelerates the adsorption of water, while Ni enhances the adsorption of OOH* . The synergistic effect of two active sites enhances the OER activity. CeO₂-NiCoP$_x$ only requires 260 mV overvoltage to drive 10 mA cm⁻² current in 1 M KOH, and the Tafel slope is 72 mV dec⁻¹.

Similarly, Shao et al. prepared Fe doped CoP two-dimensional ultra-thin nano sheet array (UNSA) for OER catalysis [171]. It can be seen from the positive shift of Co peak and negative shift of P peak in XPS (Fig. 9(c, d)) that the doped Fe promotes the electron transfer of Co to P, so that Co and P have partial positive and negative charges respectively, while the Co$^{\delta+}$ is helpful for the adsorption of intermediates and can promote the OER process [172,173]. Therefore, the energy barrier of the OH*→O* step of FeCoP decreases, which can be seen from the calculated hydrogen dissociation energy (FeCoP: 0.545 eV; CoP: 1.125 eV). In addition, as shown in Fig. 9(b), the oxygen desorption energy barrier at the Fe site is low, which leads to the transfer of oxygen to the Fe site for desorption and the rapid release of the active site of OER reaction. In conclusion, bimetallic sites are produced in FeCoP, Co sites accelerate OH* deprotonation to form O* , and Fe sites accelerate the precipitation of O₂ The bimetallic sites lead to excellent OER performance of the catalyst. Fe CoP UNSA has excellent OER activity in 1.0 M KOH, η_{20} is 260 mV, η_{100} is 330 mV, Tafel slope is 63 mV dec⁻¹.

However, when Ni and Co are both active sites, hydrolysis dissociation and O₂ release may be enhanced at the same time, and both may act as adsorption sites of intermediates. Zhao et al. prepared a series of nickel-cobalt metal phosphide catalysts (Co$_x$Ni$_y$P) by using MOF-74 as a precursor [174]. MOF-74 is suitable for studying the synergistic effect of different metal centers in forming bimetallic phosphides because it can replace metal sites without affecting the underlying framework of the MOF [175]. XPS test shows that compared with metal, the Ni Co peak of the catalyst shifts positively while the P peak shifts negatively, indicating that electrons are transferred from metal to P, and strong electron interaction contributes to the adsorption of reactants and the desorption of products. The negative shift of the P peak indicates that the electron occupation is enhanced and the electron donating ability of the catalyst is improved [176,177]. Co₄Ni₁P with the best activity in 1 M KOH η_{10} is

245 mV, Tafel slope is 61 mV dec⁻¹. This is due to the fact that Ni acts as the active site for water dissociation and Co site accelerates the release of gas [172]. Liu et al. synthesized SnPi@CoP-Ni₅P₄/NCF tri metal phosphide for OER catalysis [20]. The catalyst transmits 10 and 600 mA cm⁻² current densities in 1.0 M KOH, requiring only 180 and 364 mV low overpotentials, respectively. The author used quantum chemistry to simulate the active source. As shown in Fig. 9(e), CoP (201) has the lowest RDS energy barrier (0.3 eV) in OER catalysis, indicating that it has the best intermediate adsorption and oxygen generation capacity. For the O*→OOH* step, Ni₅P₄ (203) shows an energy barrier of − 0.02 eV, which means that for the most common RDS, Ni₅P₄ can promote the conversion of O*→OOH* . Therefore, the coupling of CoP (201) and Ni₅P₄ (203) can greatly reduce the OER energy barrier, which is 0.19 eV. During the OER process, as shown in Fig. 9(f), Ni and Co act as the adsorption sites of intermediates. OH⁻ adsorbs on the sites to form Ni-OH* and Co-OH* , and then deprotonated on Ni-OH* to form Ni-O* . OH attacks Ni-O* and binds with OH* on Co-OH* to release O₂. SnPi can also stabilize species adsorption in the reaction, and only 0.04 eV is needed for OOH*→O₂ step in SnPi-Ni₅P₄. Therefore, the excellent catalytic activity of SnPi@CoP-Ni₅P₄/NCF comes from the simultaneous use of Ni and Co as adsorption sites for key intermediates.

Some studies have also reported that non Ni or Co are used as active sites. Even though Ni species exist in the catalyst, this may be due to the introduction of more active noble metal Ir. Hoa et al. introduced monatomic Ir into amorphous NiMoP$_x$O$_y$ and crystalline NiMoP, and prepared Ir-NiMoP/NiMoP$_x$O$_y$/CNTs-Gr/Cu as OER catalyst by using foam copper on graphene sheets interconnected by carbon nanotubes as the electron transport channel [178]. The current density of 20 mA cm⁻² generated by the catalyst only requires an overvoltage of 220 mV, and the Tafel slope is 107 mV dec⁻¹, which is attributed to the introduction of monoatomic Ir and Mo as the dual active sites of electrolytic water.

Therefore, constructing multiple electroactive sites is an effective strategy to enhance OER activity. The common starting point is to introduce other metals to accelerate water dissociation or O₂ release based on NiOOH or CoOOH as active phase. There is also the coexistence of Ni and Co sites. At this time, both of them act as adsorption sites for intermediates, or accelerate water dissociation and O₂ release respectively. In addition, when precious metals are introduced, Ni or Co species may no longer act as active phases, which may be due to the better OER activity of precious metals. In general, the strategy of constructing
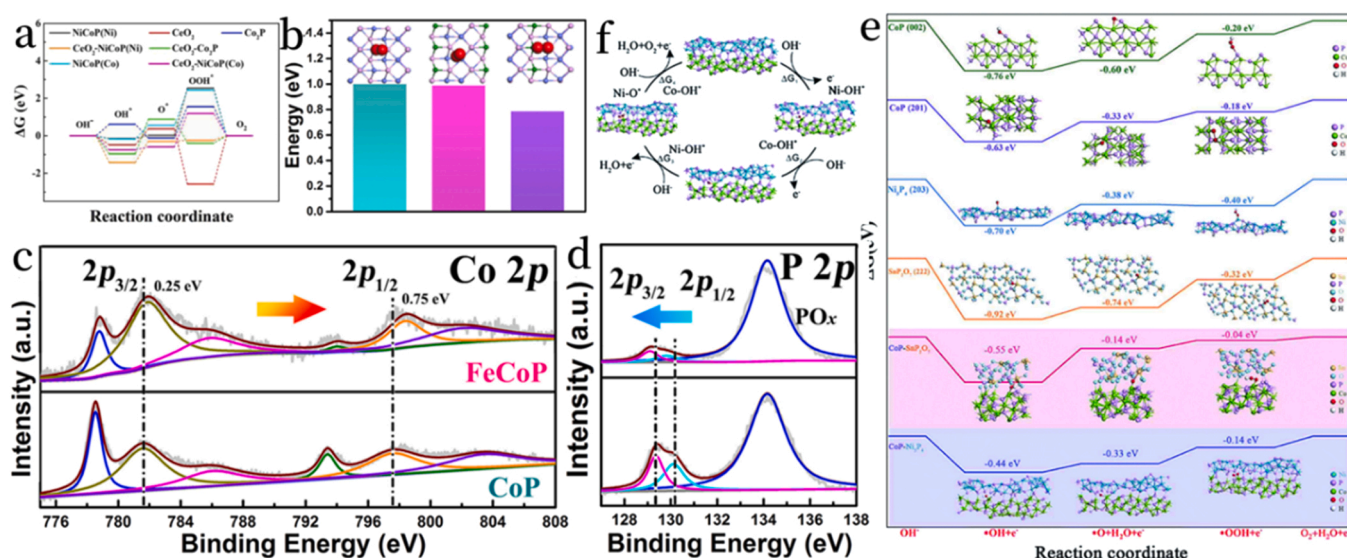

Fig. 9. (a) Gibbs free-energy evolution in the OER reaction steps of CeO₂-NiCoP$_x$/NCF. Reproduced with permission [170]. Copyright 2022, Elsevier. (b) desorption energy of oxygen molecule; (c) Co 2p and (d) Ni 2p orbital XPS spectra of FeCoP. (b-d) Reproduced with permission [171]. Copyright 2017, Elsevier. (e) Atomistic crystal models and free energy evolution of OER for SnPi@CoP–Ni₅P₄/NCF. (f) The OER reaction steps on the CoP–Ni₅P₄/NCF catalyst. (e-f) Reproduced with permission [20]. Copyright 2022, Royal Society of Chemistry.

polymetallic sites is promising, but how to accurately construct multiple active sites requires more in-depth theoretical research. More importantly, there are fewer reports on building polymetallic sites to enhance OER activity, so more research reports are needed. Some catalysts prepared for double active sites are listed in Table 3 for comparisons.

4.1.4. Promote the formation of active phase

As described in the mechanism part, TMPs will be converted into oxides/hydroxides corresponding to transition metals during the OER process, which is the real active species in the OER process. The active species formed on the catalyst surface during the OER process play an important role in ensuring the long-term activity and stability of the catalyst under harsh alkaline conditions [179,180]. Therefore, when designing TMPs as OER catalysts, appropriate strategies should be adopted to accelerate the formation of OER active phase. One of the characteristics of TMPs in water decomposition catalysis is to promote the formation of active phase by dissolving P [181,182]. When Brock et al. studied the role of precious metals in non precious metal phosphides, they found that the presence of Rh would reduce the oxidation potential of Ni and accelerate the generation of active phase. At the same time, the phase separation of Rh in the OER process can enhance the intrinsic activity of active phase, which can be confirmed by the reduced ECSA and the increased ECSA normalization current [183]. Therefore, the dissolution of elements contributes to the activation of OER, but the specific mechanism is unknown, and it is necessary to find non precious metal activation elements that can replace precious metals.

Researchers often use element doping to regulate the electronic structure of active sites to promote the formation of active phases. Jiang et al. prepared Fe doped CoP nano sheets for OER catalysis ($Co_{0.8}Fe_{0.2}P$) [184]. XPS spectra show that Co-O and P-O peaks of $Co_{0.8}Fe_{0.2}P$ are stronger than those of CoP species, and M-O and M-OH species are observed, which indicates that Fe doping can accelerate the oxidation of CoP and help the formation of active phase. When $Co_{0.8}Fe_{0.2}P$ is used to catalyze OER in 1 M KOH, a current of 10 mA cm^{-2} can be generated at an overvoltage of 270 mV, and the Tafel slope is 50 mV dec^{-1}.

Similarly, Wang et al. used Fe to adjust the charge density of the Co site and change the electronic structure of the phase interface [185]. XPS spectrum shows that the Co peak shifts negatively and the P peak shifts positively after Fe doping, which confirms the existence of strong electron interaction and is conducive to the redistribution of interface charges [186]. XPS spectrum after OER stability test shows that M-P species of the material are transformed into oxides or hydroxides, and Co-P and $Fe_{0.5}Co$-P are compared, as shown in Fig. 10(a, b), the content of CoOOH increases with the addition of Fe, indicating that doping Fe accelerates the formation of active phase by changing the charge density of the site.

Cai et al. creatively prepared O doped NiCoP-O/NC nano sheets [187]. The doped O atoms extend the M - P bond to activate the catalytic

Table 3
Comparisons of OER catalytic activities of various TMPs.

Catalyst	Overpotential (mV@mA cm^{-2})	Tafel slope (mV dec^{-1})	iR compensation	Reference
CeO_2-NiCoP$_x$	260 @ 10	72	with	[170]
FeCoP UNSA	260 @ 20	63	unknown	[171]
Co_2Ni_1P	245 @ 10	61	with	[174]
SnPi@CoP–Ni$_5$P$_4$/NCF	364 @ 600	52	with	[20]
Ir-NiMoP/NiMoP$_x$O$_y$ /CNTs-Gr/Cu	220 @ 20	107	with	[178]

Note: in the column of iR compensation, "with" represents iR compensation, "without" represents no iR compensation, the percentage represents the percentage of compensation, and "Unknown" represents no clear indication of compensation in the literature.

site. It has been reported in the past that the elongation of M-P bond is conducive to the oxidation of metal active sites at high potential, which is a process of electron loss, thus promoting electron transport to enhance the OER process [103,188]. The η_{10} of NiCoP-O/NC is 300 mV, Tafel slope is 94 mV dec^{-1}. Li et al. doped highly electronegative S into NiFeP as OER catalyst (CCS-NiFeP-10) [15]. It only needs 201 mV overvoltage to generate a current of 10 mA cm^{-2}, Tafel slope 41.2 mV dec^{-1}. XPS spectrum shows that electrons transfer from low electronegative Ni to high electronegative S, and high positive charge Ni tends to coordinate with lone pair electrons of O in H_2O, which is helpful for the dissociation of O-H bond. As shown in Fig. 10(c), the XANES peak on the K side of Ni moves to a higher energy, which indicates that more unoccupied states increase, which can induce the transfer of electrons from Ni to S, leading to a higher oxidation state [189]. DFT calculation results show that Ni is the active site. The charge density difference shows that the charge value of S is positive, indicating that it can capture electrons in the OER process. Therefore, more electrons are lost from the active site Ni to induce the generation of active phase.

Shen et al. co doped Ni and Fe into the parent phosphide Z67-H-P to form $CoNi_{0.2}Fe_{0.05}$-Z-H-Py as OER catalyst [190]. The η_{10} is 329 mV, Tafel slope is 48.2 mV dec^{-1}. Co-doping of Ni and Fe leads to electron density rearrangement. XANES spectrum shows that the unoccupied state of Co 4p increases, and more unoccupied states of Co 4p provide more charge transfer channels, thus promoting effective charge carrier transport. The author has compared the CV diagrams of $CoNi_{0.2}Fe_{0.05}$-Z-H-P and other samples. For $CoNi_{0.2}Fe_{0.05}$-Z-H-P, as shown in Fig. 10(d), the redox peak appeared in the first scan, and then the current was well maintained at the same level, while the current of other metal phosphides (i.e. Z67-H-P, $CoNi_{0.2}$-Z-H-P and $CoFe_{0.05}$-Z-H-P) hardly increased after the first CV cycle. The above results indicate that suitable Ni/Fe co doping can accelerate the formation of highly active and stable active species in situ electrochemistry.

In addition, the construction of heterostructure and the generation of built-in electric field can transfer electrons and promote the formation of active phase. Chen et al. prepared $Co(OH)_2$/NiP$_x$ nanosheet arrays by building heterostructures and using strong interactions between different substances to promote the formation of active phases [191]. XPS, XRD and UV vis test results can confirm that the strong interaction between $Co(OH)_2$ and NiP$_x$ promotes the formation of the active phase CoOOH, which is shown in the negative shift of the characteristic redox peak in the LSV curve, as shown in Fig. 10(e). Therefore, the over-potential required for OER reaction is also reduced. It only takes 236 mV and 304 mV to provide the current density of 10 and 100 mA cm^{-2}, and the Tafel slope is 52 mV dec^{-1}. Wang et al. prepared Ru@FeCoP heterostructure as OER catalyst [192]. The Ru/FeCoP heterostructure can be used as an electron transfer bridge to make more electrons flow from Co-Fe to Ru, so that Co/Fe is positively charged under the drive of the heterogeneous interface, which is easy to form Fe-O and Co-O, which is conducive to the formation of OER active species. The η_{10} is 267 mV, Tafel slope is 45.7mV dec^{-1}, the peak intensity of the characterization XRD map after catalysis is slightly reduced, the peak width is slightly widened, the oxidation peaks of Fe and Co in the XPS spectrum are significantly enhanced, and the peak of phosphide is significantly reduced, indicating the formation of active species.

In particular, Chu et al. developed a method of in-situ phosphating and rapid surface reconstruction to obtain active phase CoOOH (Hy-Ni-CoP/Co$_2$P @ NC) [193]. CoOOH comes from the pyrolysis formation of surface metal phosphides and the conversion of Co^0 species into Co$(OH)_2$ and then into CoOOH during CV activation. Therefore, compared with only CV activity, the number of active phases increases. More importantly, the carbon defect in NC further enhances the activity of the active phase, as shown in Fig. 10(f) differential charge density, there is a strong electron interaction between the defect and CoOOH, leading to an increase in the electron density around Co, which is conducive to the adsorption and desorption of intermediates. Therefore,
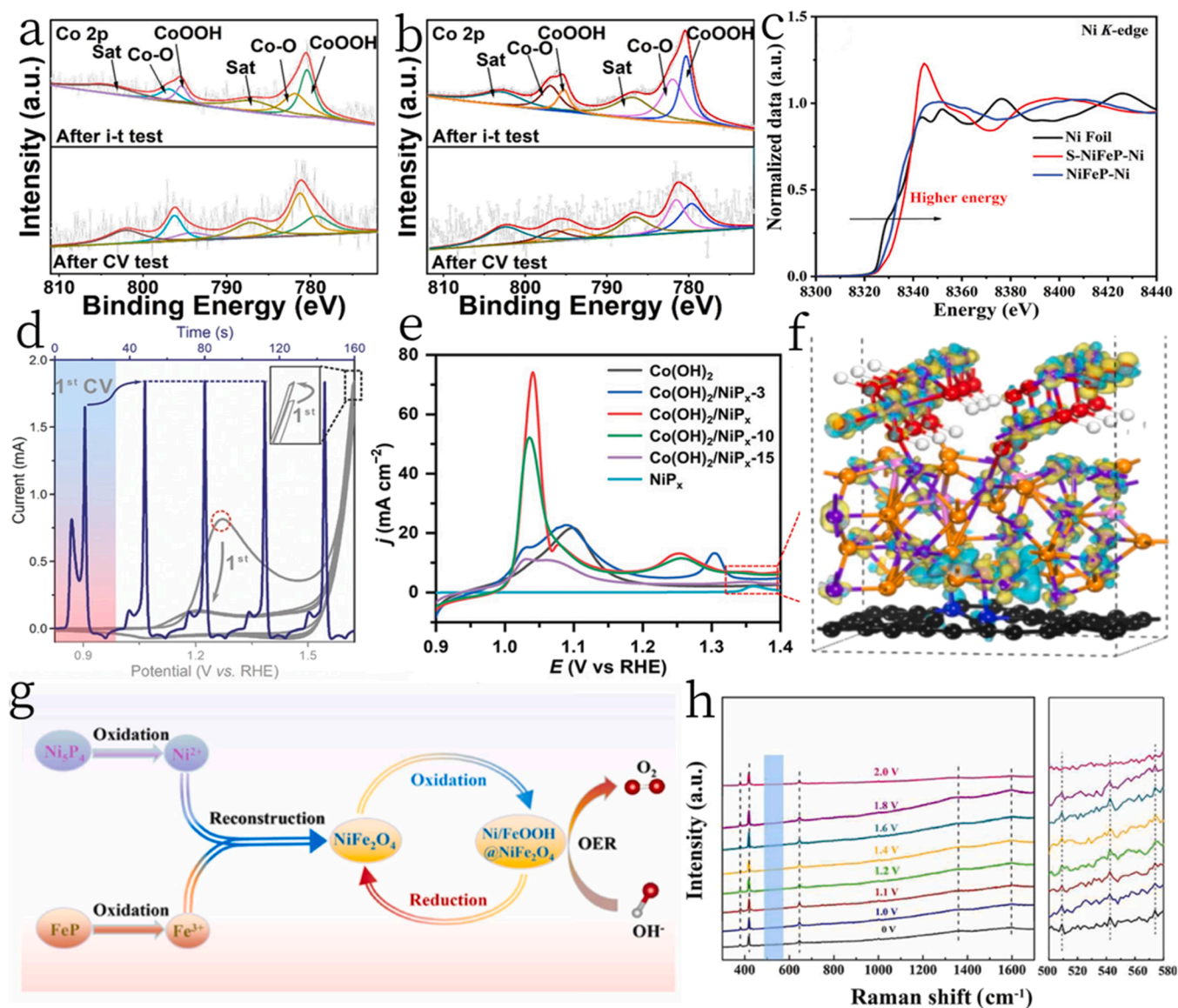
Fig. 10. (a) XPS spectra of CoP and (b) $Fe_{0.5}Co-P$ in Co 2p region after i-t and CV test. (a-b) Reproduced with permission [185]. Copyright 2022, Elsevier. (c) Normalized Ni K-edge XANES spectra of the S-NiFeP, NiFeP samples and Ni foil. Reproduced with permission [15]. Copyright 2022, Wiley-VCH. (d) CV plots (gray line) at a scan rate of 50 mV s^{-1} and the derived current-time plot (blue line) for CoNi$_{0.2}$Fe$_{0.05}$-Z-H-P in 1 m NaOH aqueous solution. The red broken circle is the redox peak for CoII/CoIII in the first CV scan. Reproduced with permission [190]. Copyright 2018, Wiley-VCH. (e) LSV curves of Co(OH)$_2$, heterostructured samples and NiP$_x$. Reproduced with permission [191]. Copyright 2022, Wiley-VCH. (f) The differential charge density image of Hy-Ni-CoP/Co$_2$P @ NC. Reproduced with permission [193]. Copyright 2022, Elsevier. (g) Schematic illustration of the dynamic surface reconstruction to form active of Ni/FeOOH-NiFe$_2$O$_4$ layer at the Ni$_5$P$_4$@FeP surface.. Reproduced with permission [194]. Copyright 2022, Elsevier. (h) In operando Raman spectra of CeO$_2$-NiCoP$_x$/NCF at various potentials during OER. Reproduced with permission [170]. Copyright 2022, Elsevier.

Hy-Ni-CoP/Co$_2$P @ NCc's overpotential of 10 mA cm^{-2} is 272 mV, Tafel slope is 69 mV dec^{-1}, close to commercial RuO$_2$.

Interestingly, Li et al. found that Ni and Fe formed NiFe$_2$O$_4$ first and then Ni during the activation process/ FeOOH@NiFe$_2$O$_4$[194]. In situ constructed NiFe$_2$O$_4$ can improve the OER activity of NiOOH [195,196]. Raman spectroscopy confirmed that Ni and Fe were rapidly oxidized under low voltage during CV activation, and reconstructed into NiFe$_2$O$_4$. NiFe$_2$O$_4$ under high overpotential was oxidized to Ni/FeOOH@NiFe$_2$O$_4$. The activation process of hybrid is shown in Fig. 10(g). The large amount of P dissolves to form amorphous NiFe$_2$O$_4$ with rich defects. The catalyst only needs 205 and 242 mV overvoltage to generate current density of 10 and 100 mA cm^{-2}. The Tafel slope is 43.93 mV dec^{-1}, which is superior to the catalyst with only NiOOH as the active phase. Therefore, NiFe$_2$O$_4$ formed by surface reconstruction can further enhance the catalytic activity of NiOOH. Similarly, Wen et al. recorded surface

species changes through laser Raman spectroscopy (Fig. 10(h)) [170], the formed NiCO$_2$O$_4$ shows better OER activity than TMPs [197], thus enhancing the performance of CoOOH active phase. This inspired researchers to further explore the metastable intermediate state of TMPs in the OER process, which is very helpful to reveal the reaction mechanism.

To sum up, in order to accelerate the generation of active phase, researchers often pay attention to the change of species binding energy in XPS map. The increase of unoccupied state in XANES map, the elongation of M-P bond and the negative shift of oxidation peak in LSV curve indicate that the formation of active phase is accelerated. On the other hand, the dissolution of P element peculiar to TMPs catalyst can accelerate the formation of active phase. Researchers also focus on the strategies of element doping to control the electronic structure of active sites and interface engineering to control electronic rearrangement. However, other methods to accelerate the formation of active phase are

still needed, such as the formation of active phase by phosphide pyrolysis [193]. More importantly, metastability in the activation process seems to be very helpful to OER activity, and researchers need to further develop in-situ characterization methods to explore the specific activation process of the catalyst. Some catalysts prepared for accelerating the formation of active phase are listed in Table 4 for comparisons.

4.2. Increase the number of active sites/active surface area

4.2.1. Construction of special nanostructures

Transition metal phosphides have gradually become a new catalyst to replace the noble metal catalysts due to their low kinetic energy barrier and good conductivity. Unfortunately, although the phosphides will be converted into corresponding oxides/hydroxides in situ (which has been proved to be a real catalytic species) during the OER process, the insufficient conductivity of oxides and hydroxides will obviously affect the catalytic activity of metal phosphide catalysts [198]. Therefore, it is necessary to employ various modulation strategies to increase catalyst activity. Usually, electrochemical reactions occur on surfaces or interfaces, so the nanostructure, chemical composition, and topography of catalyst are critical to catalytic activity. The size of the catalyst is designed to be nanoscale, and its physicochemical properties will change. In general, the smaller the nanometer size, the more active sites are exposed, and the better the activity of the catalyst [199]. As previously mentioned, researchers often improve the performance of electrocatalyst from two aspects, namely the number of active sites and the intrinsic activity of the active sites The previous aspects are all based on improving the intrinsic activity of the active sites of the catalyst. In this chapter, we will focus on common methods to increase the number of active sites or the active area.

4.2.1.1. Special hollow porous structure.
Liu et al. prepared a 3D hollow polyhedron cobalt phosphide catalyst (CoP hollow polyhedron) and compared it with CoP nanoparticles [200]. SEM images in Fig. 11(a) show that CoP hollow polyhedron obtained after phosphating and calcination exhibits the regular polyhedrons with wrinkles and cracks. N_2 adsorption/desorption isotherms indicate that wrinkles and fractures provide high specific surface area and porosity. It is worth noting that the surface of the hollow polyhedron is less oxidized than the CoP particles, perhaps because the hollow polyhedron avoids contact and aggregation of the particles, thereby reducing the diffusion of oxidation process. At the same time, if the oxide layer is too thick will cover the active sites and hinder mass transfer. Huang et al. used an innovative method with low toxicity and no external phosphorus source to prepare FeNiP/C-900 nanoparticles by pyrolysis at 900 °C [201]. As shown in Fig. 11(b), the particles are hollow barrels. The nitrogen

Table 4
Comparisons of OER catalytic activities of various TMPs.

Catalyst	Overpotential (mV@mA cm^{-2})	Tafel slope (mV/dec^{-1})	iR compensation	reference
Co$_{0.8}$Fe$_{0.2}$P	270 @ 10	50	with	[184]
NiCoP-O/NC	300 @ 10	94	95%	[187]
CCS-NiFeP-10	201 @ 10	41.2	without	[15]
CoNi$_{0.2}$Fe$_{0.05}$-Z-H-Py	329 @ 10	48.2	80%	[190]
Co(OH)$_2$/NiPx	304 @ 100	52	with	[191]
Ru@FeCoP	267 @ 10	45.7	with	[192]
Hy-Ni-CoP/ Co$_2$P @ NC	272 @ 10	69	with	[193]
Ni$_5$P$_4$ @FeP	242 @ 100	43.93	with	[194]

Note: in the column of iR compensation, "with" represents iR compensation, "without" represents no iR compensation, the percentage represents the percentage of compensation, and "Unknown" represents no clear indication of compensation in the literature.
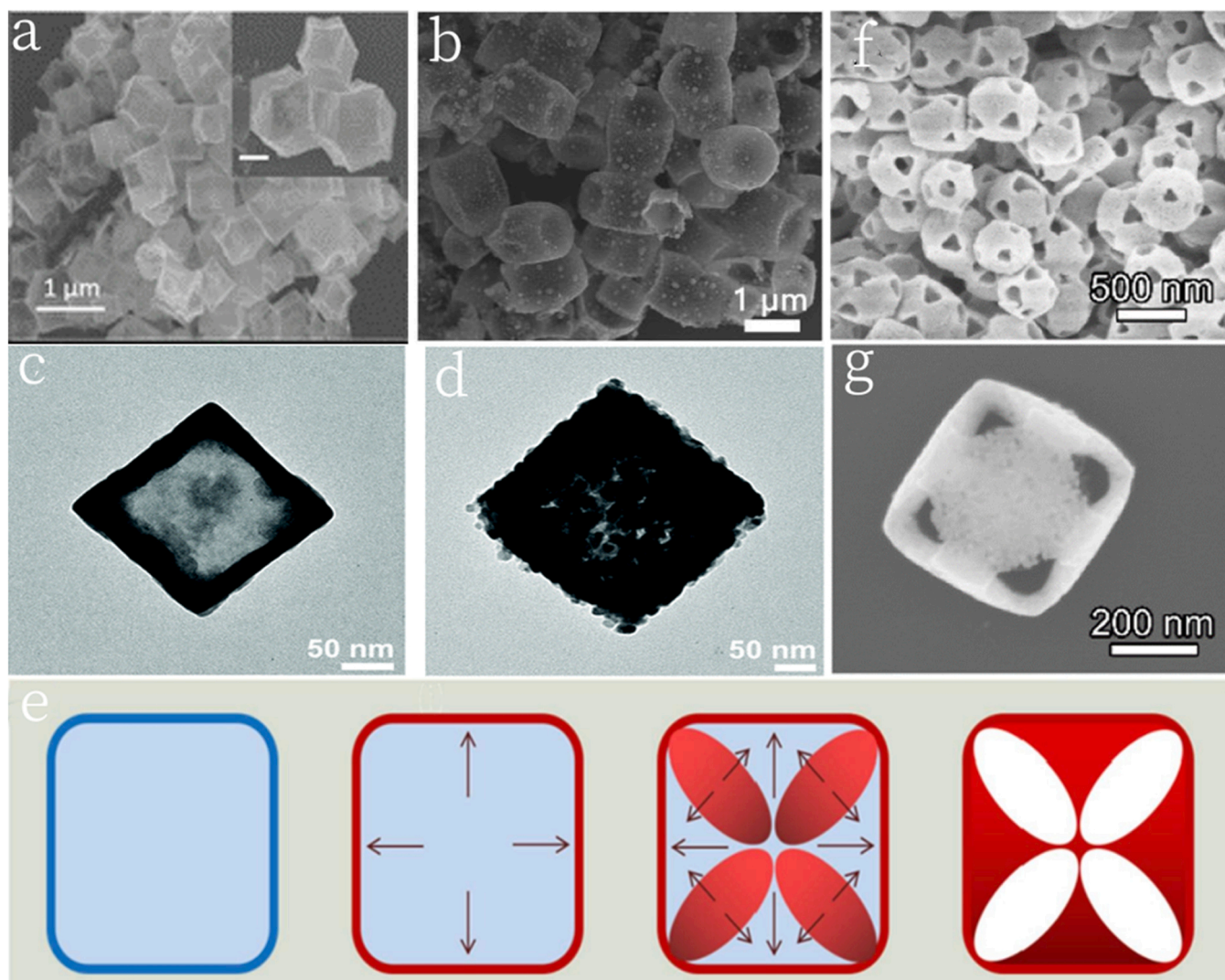
adsorption/desorption isotherms show a high specific surface area, which can promote ion transport and increase the number of active sites to increase OER activity. It is worth mentioning that compared with the samples prepared at 800 and 1000 °C, the FeNiP/C-900 has a higher graphitization degree and higher conductivity. The OER test in 1.0 M KOH showed that the FeNiP/C-900 has the smallest overpotential (229 mV @ 10 mA cm^{-2}), the smallest Tafel (74.5 mV dec^{-1}), and the largest C_{dl} (25.8 mF cm^{-2}).

The void space between the hollow nanoframes can not only provide a shorter mass transfer path, but also increase the specific surface area to provide rich active sites. The hollow nano framework formed by hollowing out the internal non functional atomic structure has large surface area and high atom utilization, which can provide highly dispersed active sites, reduce the catalyst mass and enhance the specific activity. Better still, compared with closed hollow nanostructures, this structure allows reactants to penetrate into the interior, making full use of the internal active sites. Chen et al. designed CoP NF with a hollow nano frame by precipitation-etching-phosphating steps [202]. SEM images in Fig. 11(f, g) show that the corners of the frame have cavities and small holes, which can accelerate electrolyte penetration and gas release. OER catalytic performance of CoP NF was tested in 1.0 M KOH, η_{10} was 323 mV, and the Tafel value was 49.6 mV dec^{-1}.

Interestingly, Liu et al. developed a new core-shell conversion method to produce Ni-Co-Fe-P [203]. As shown in Fig. 11(e), during phosphating, PBAs nano cubes enter hollow Ni-Co-Fe-P nano boxes by using interface induced shrinkage. Core-shell Ni-Co@Fe PBA was successfully prepared by seed coprecipitation method. As a comparison, Ni-Co PBA nano-cubes were synthesized by chemical precipitation method. At the beginning of phosphating pyrolysis, the Fe-PBA shell was transformed into a mixed layer of iron-based materials and carbon, which prevented the NiCo-PBA seeds from shrinking rapidly and the internal seeds from collapsing to form petal-like cavities. The thermal insulation of the shell makes it lag and gradually shrink, forming a hollow nanobox structure. Compared with Ni-Co-PBA nanocubes, the formed hollow nanoboxes have larger and more regular space, and the carbon layer converted from Fe-PBA shells can also improve conductivity. The hollow Ni-Co-Fe-P nanobox can reach 20 mA cm^{-2} at an overpotential of 277 mV and provide a current density of 50 mA cm^{-2} at an overpotential of only 312 mV. The Tafel slope of the catalyst is 85.64 mV dec^{-1}, and the current decay is only 5% during 24 h of continuous operation.

Open porous structure and large surface area can increase the exposure of active sites, thus improving catalytic performance [204]. Lou et al. prepared porous Fe-Co-P nano-capsules and measured their electrocatalytic OER activity in 1.0 M KOH [205]. Compared with Fe-Co-P and Fe-P nanocubes, the porous Fe-Co-P nano-boxes have cavities (Fig. 11(c, d)), which can reduce ion transport resistance and expose more active sites. The porous Fe-Co-P nanobox has the lowest onset potential, the smallest overpotential (269 mV @ 10 mA cm^{-2}), and the smallest Tafel slope (31 mV dec^{-1}). Abhishek Meena et al. reported a mesoporous Ni$_2$P @ FePO$_x$H$_y$ nanoparticle composite [206]. BET analysis confirmed that the abundant porous structure exposes a large number of active sites and active surface areas for OER, and can also promote the adsorption/desorption process [207,208]. The catalyst can produce a current density of j = 1 A cm^{-2} in 1 M KOH, which only requires 360 mV overvoltage, and maintains extraordinary stability after 100 h of operation at j = 100 mA cm^{-2}, meeting the needs of large-scale industrial application. Xiao et al. prepared carbon doped porous honeycomb NiCoFe catalyst (NiCoFeP/C) [209]. XRD characterization detected the presence of a small amount of carbon, a residue during pyrolysis, which can enhance conductivity and accelerate electron transfer. The phosphating process volatilizes the organisms on the nanospheres' surface, so the catalyst exhibits a porous honeycomb shape, which can increase the active sites. The η_{10} of NiCoFeP/C is 270 mV, the Tafel slope is 65 mV dec^{-1}, and ECSA and R_{ct} are better than RuO$_2$, which is a good OER catalyst.

Fig. 11. (a) SEM image of CoP hollow polyhedron. Inset scale bar: 300 nm. Reproduced with permission [200]. Copyright 2016, American Chemical Society. (b) SEM image of FeNiP/C-900. Reproduced with permission [201]. Copyright 2019, Elsevier. (c) TEM images of the Fe–Co PBA nanoboxes. (d) TEM images of the Fe–Co–P nanoboxes. (c) and (d) Reproduced with permission [205]. Copyright 2019, American Chemical Society. (e) Schematic diagram of the structural evolution from core-shell Ni-Co@Fe PBA nanocubes to hollow Ni-Co-Fe-P nano boxes. Reproduced with permission [203]. Copyright 2022, Elsevier. (f, g) SEM images for CoP NFs. (f-g) Reproduced with permission [202]. Copyright 2019, American Chemical Society.

In particular, Wei et al. prepared macroporous CoFeP TPAs/Ni in order to develop porous nanostructure materials [210]. After phosphating, the large interconnected pores are retained, and the large interconnected pores formed in the plane can increase the active sites and promote ion diffusion and electrolyte transport. CoFeP TPAs /Ni has excellent OER catalytic activity in 1.0 M KOH, and only 198 mV and 250 mV overpotentials are required to drive the current densities of 10 mA cm^{-2} and 100 mA cm^{-2}, respectively. The Tafel slope is 42.0 mV dec^{-1}, lower than CoFeP/Ni, which proves the contribution of large interconnected pores to OER activity.

4.2.1.2. Special one-dimensional structure. In the one-dimensional nanostructure, in addition to common nanospheres, nanoparticles, nanowires, and nanorods, the narrow needle-like nanostructure is unique, which also can increase the active area, expose more active sites, and promote ion diffusion. Wu et al. prepared CoP$_3$-NAs/CFP by topologically phosphating Co(OH)F precursor on highly conductive carbon fiber paper (CFP) [211]. Nanoneedle arrays were grown on CFP. TEM images showed that the nanoneedles were porous. The special nanoneedle structure can significantly increase the specific surface area and

the number of electrically active sites. The nitrogen adsorption/desorption isotherms confirm the above conclusions. Further, according to DFT calculation, Song et al. found that doping a small amount of Ni would not change the needle array, but the electronic properties could also be adjusted to enhance the catalytic activity of CoP$_3$ [212]. Co$_{0.93}$Ni$_{0.07}$P$_3$ NA was obtained by phosphating Co$_{1-x}$Ni$_x$(OH)F NA used as precursor. As shown in the SEM image in Fig. 12(a, b), the sample maintained needle shape before and after phosphating. The η_{20} of Co$_{0.93}$Ni$_{0.07}$P$_3$ is 221 mV, Tafel slope is 83.7 mV dec^{-1}.

In particular, Qin et al. prepared "stalk"-"cap"-typed nanoarray (Sn$_4$P$_3$/Co$_2$P SCNAs) with a unique "stem cap" structure [213]. SEM images can significantly observe high-density vertically arranged nanoneedle arrays, and slender nanoneedles can effectively promote mass transfer and electrolyte penetration, and prevent agglomeration. Fig. 12(c) SEM photos at high magnification can observe the rough cap on the top of the nano needle, which improves the hydrophilicity of the material, prevents the accumulation and strong adsorption of bubbles, and thus releases smaller bubbles than other samples, as shown in Fig. 12(d).
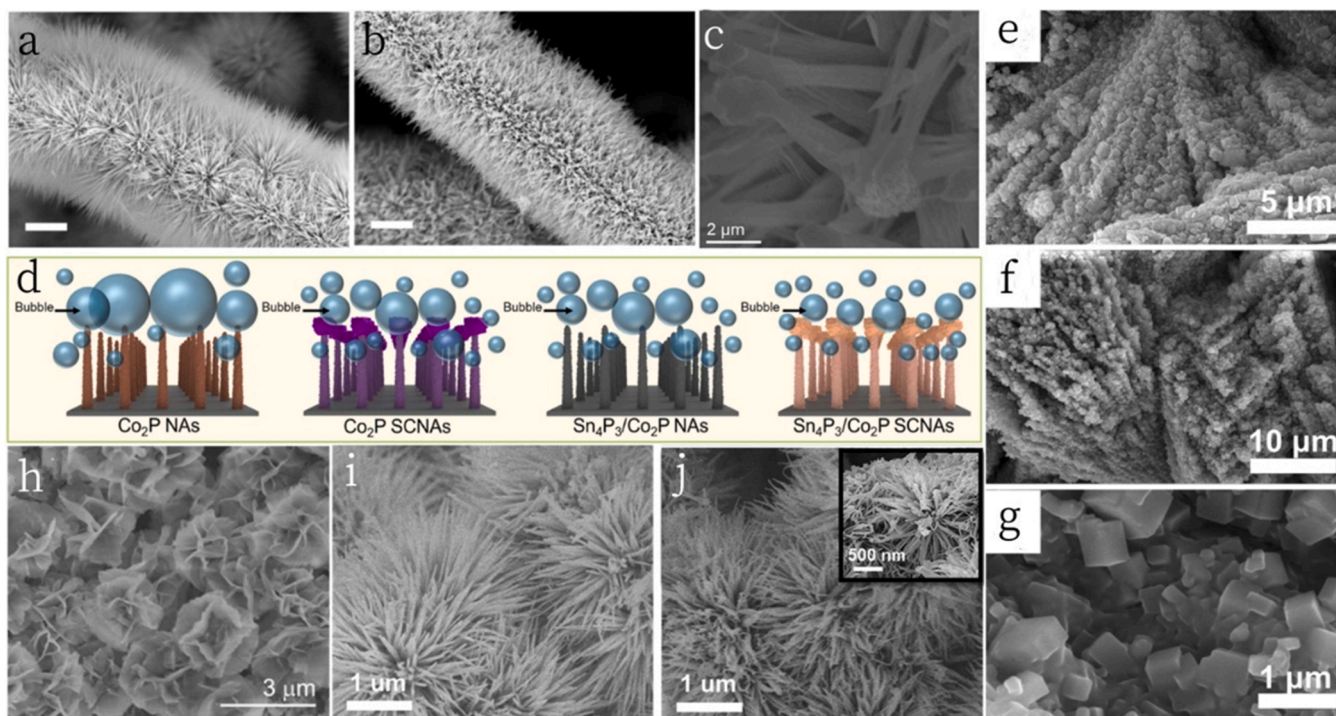
Fig. 12. SEM images of (a) $Co_{0.93}Ni_{0.07}(OH)F$ NAs, and (b) $Co_{0.93}Ni_{0.07}P_3$ NAs after phosphidation treatment (Scale bars: 5 μm). (a-b) Reproduced with permission [212]. Copyright 2018, American Chemical Society. (c) Morphological characterization of the formed Sn_4P_3/Co_2P SCNAs. SEM images. (d) the schematic illustration of bubble size release from different electrodes. (c) and (d) Reproduced with permission [213]. Copyright 2022, Elsevier. (e) SEM images of CoFePBA/CoBDC/NF. (f, g) SEM images of CoFeP/NF. (e-g) Reproduced with permission [218]. Copyright 2022, Elsevier. (h) SEM of the as-prepared Co-3DHFLM. Reproduced with permission [219]. Copyright 2019, Elsevier. SEM images of (i) 10FeNiCoP precursor and (j) 10FeNiCoP, where the insets show magnified images of 10FeNiCoP. (i) and (j) Reproduced with permission [221]. Copyright 2020, American Chemical Society.

4.2.1.3. Special two-dimensional structure. In two-dimensional structure, nano sheet is usually the research object. Interestingly, Yang et al. prepared nanosheet arrays Fe-Ni$_2$P/NF with the different surface roughness by controlling the amount of phosphorus source [214]. SEM and TEM images confirmed that with the increase of NaH$_2$PO$_2$ powder addition, the surface roughness of nanosheet arrays increased, but the initial morphology could be maintained. Electrochemical tests show that the R-Fe-Ni$_2$P with slight roughness has the best OER catalytic activity ('R' means the material has a slightly rough surface). Rough nano sheet surface can provide rich active sites and effectively release bubbles, speeding up OER dynamics [215]. The overpotential at 100 mA cm^{-2} is only 213 mV, and the Tafel slope is 50.7 mV dec^{-1}. Unfortunately, the report does not clearly explain why OER activity decreases when the roughness is too large. In the nano sheet, the two-dimensional ultra-thin nano sheet exposes many surfaces with low coordination steps, edges and kinks, thus providing rich active sites, rapid mass transfer and better conductivity, and has been used in the research of high-performance catalysts [216,217]. Zhao *et al.* phosphating NiCo(OH)$_2$ ultra-thin nano sheets to obtain Ni-CoP ultra-thin nano sheets [136]. The existence of pores in the ultra-thin nano sheet enables the electrolyte to fully contact the active site. BET also confirmed the large specific surface area of the ultra-thin nano sheet. Thanks to a large number of active sites that can be fully contacted, Ni-CoP-5% with the best OER activity needs 290 mV overvoltage to generate a current density of 10 mA cm^{-2}, and the Tafel slope is 66 mV dec^{-1}.

The nanocube array structure can also greatly promote charge transfer in the electrochemical process and increase the exposure of active sites. Its open space can encourage the penetration of electrolytes and is a good choice for catalyst morphology. In addition, the precursors can largely determine the morphology and properties of metal phosphides. Yi et al. prepared CoFeP/NF nano cubic arrays by selecting Prussian blue analogues (PBA) as precursors. When they are converted

into metal phosphides, their surface morphology is usually not changed [218]. SEM images of PBAs precursor (Fig. 12(e)) and CoFeP/NF (Fig. 12 (f, g)) showed nanocube arrays, indicating that this method can indeed maintain a perfect cube shape. The surface of CoFeP/NF is rough and porous, which is beneficial to increasing the surface area and active sites of the catalyst. CoFeP/NF has excellent OER activity, and only 253 mV overpotential can reach a current density of 10 mA cm^{-2}, Tafel slope is 36 mV dec^{-1}, R_{ct} value is 0.9 Ω, and C_{dl} is 18.82 mF cm^{-2}.

4.2.1.4. Special three-dimensional structure. Some unique 3D layered nanostructures composed of one-dimensional nano particles or two-dimensional nano sheets are often concerned by researchers. Li et al. synthesized 3D layered flower like structure composed of ultra-thin nano sheets (CoNi-P-3DHFLM) [219]. The SEM image (Fig. 12(h)) shows a panoramic view of the layered flower-like structure, with the nanosheets remaining at a thickness of 1.6 nm, the flower-like structure is composed of interconnected nanosheets. Such a unique 3D layered structure enables the electrolyte to fully contact the catalyst to accelerate ion transport. In addition, the ultrathin nanosheets and their disordered orientation avoid the agglomeration of catalyst and improve the stability. The phosphating process also gives the flower-like structure a large pore size distribution from micropores to mesopores, exposing more active sites. Thanks to the unique flower like structure, η_{10} of CoNi-P-3DHFLM is 292 mV, Tafel slope is 84 mV dec^{-1}, and mass activity is 253 A g^{-1}.

The sea urchin-like structure has a dispersed high porosity, which provides a large electrochemically active surface area, fully exposed active sites, and fast mass transport pathways [220]. And the urchin-like superstructure rigidity can avoid agglomeration [221]. Inspired by this, Feng et al. prepared sea urchin-like iron-doped nickel-cobalt phosphide (FeNiCoP) by hydrothermal and phosphating treatment [221]. SEM images in Fig. 12(i, j) revealed that the precursors owned the unique sea

urchin-like structures composed of nanoneedles, and phosphating did not destroy the sea urchin-like structure, indicating that the structure has good stability. Nitrogen adsorption-desorption isotherms indicate that its porous structure can expose active sites and promote gas release. 10FeNiCoP with sea urchin-like structure showed excellent OER catalytic activity with a low overpotential of 259 mV at 10 mA cm^{-2} and a Tafel slope of 40 mV dec^{-1}.

The advanced yolk-shell nanostructures also have good catalytic properties. Firstly, the shell can maintain the composition and structural integrity of the internal metal particles, thereby having good stability and preventing deformation and dissolution during the OER process [222]. Secondly, the core-shell structure can selectively control molecular penetration [220]. In addition, it has a fast mass transfer channel, which can accelerate the reduction and release of oxygen to improve OER catalytic activity [223]. Lin et al. also found that the construction of core-shell structure can regulate the surface morphology of shell MOF, thereby improving the conductivity [224].

On this basis, Du et al. prepared the CoNiFeP yolk shell nano-spindle (CoNiFeP-YSNS) catalyst [222]. The evolution of yolk-shell structure can be observed by TEM technique. After ion exchange, phosphating and other steps, the spindle structure gradually evolves into yolk-shell structure. There are a large number of pores at the interface between the core and the shell, which can provide many charges and material diffusion channels. The η_{10} of CoNiFeP YSNS is 261 mV, and the Tafel slope is 49.5 mV dec^{-1}, indicating high OER performance.

More interestingly, Lee et al. successfully prepared the O-doped Co$_2$P nanolayer covering CuO NWs, thereby forming a core-shell nanostructure(O-Co$_2$P/CuO NWs) [225]. CuO NWs as the core and Co$_2$P as the shell. The catalyst prepared without CuO NWs as a carrier has obvious agglomeration, which shows that CuO NWs have the effect of stabilizing shell growth. It is worth mentioning that the interaction beteen C$_{O2}$P and CuO leads to the obvious deformation of Co$_2$P nanolayer, resulting in abundant defects on the crystal surface, thereby improving the catalytic activity. The OER performance was tested in N$_2$-saturated 1.0 M KOH solution. The overpotential was 270 mV at 10 mA cm^{-2}, and the Tafel slope was 74.4 mV dec^{-1}, which were better than RuO$_2$-C/CF.

4.2.2. Select a special support

Unfortunately, TMPs nanoparticles with the above excellent structure are prone to aggregation. MOFs have a large specific surface area, multi-level porous structure, and customizable porous properties so that they can be used as ideal precursors for many TMP derivatives [226]. However, MOFs mostly exist in powder form, and the direct conversion of MOF into derivatives is mostly in powder or particles [227]. MOF derivatives in the form of a single microcrystalline powder as an electrode material usually have the disadvantage of poor electronic conductivity. This is because it is necessary to use insulating polymer binders (such as polytetrafluoroethylene and Nafion) to bond MOF powder to the substrate, which hinders the exposure of the active sites and inhibits mass transfer, eventually leading to a decrease in the conductivity of the entire electrode [228,229]. In addition, long-term catalytic process may lead to catalyst stripping [230]. Moreover, MOF derivatives in powder form are prone to aggregation, which limits charge transport capacity and leads to low active surface area and few active sites [224,227].

Therefore, loading nanoparticles on specific carriers can reduce the use of adhesives, thus avoiding agglomeration and exposing more active sites [231]. Common conductive substrates, such as foam nickel, stainless steel mesh and foam, can prepare 3D self-supporting nanomaterials and improve catalytic activity. In situ growth of catalysts on these 3D conductive substrates eliminates the need for adhesives, thus avoiding the loss of active sites, ensuring the integrity of electrodes and providing a larger surface area. There are many literatures about nano particles loaded on the above conductive substrate, so I will not repeat them here.

4.2.2.1. MXene.
MXene is a new two-dimensional material synthesized by MAX phase selective etching of A layer. It is a transition metal-carbon/nitrogen compound, which is expressed as M$_{n+1}$X$_n$T$_x$, where M is a transition metal, X is C or N, and T is a surface terminal group. As a conductive substrate, MXene can interact with the catalyst to regulate the electronic environment. It has rich functional groups and hydrophilic surfaces. Surface functional groups such as -OH, -O or -F can promote the absorption of active metal ions and prevent agglomeration [232]. Its large electronegativity makes it easy to attract electrons from transition metals, and its performance even exceeds LDH. Researchers favor its superior electrical conductivity as an emerging excellent conductive substrate, such as Ti$_3$C$_2$, with conductivity up to 9880 S cm^{-1} [233]. Phosphides loaded on MXene promise to prepare catalysts with high OER catalytic performance.

Liu et al. prepared NiFe-LDH nanosheets grown on MXene sheets by hydrothermal and obtained NiFeP/MXene by phosphating treatment [234]. The OER catalytic activity test results of different proportions of NiFe-LDH/MXene show that the proportion will greatly affect the number of active sites and conductivity. Compared with NiFe-LDH, NiFeP/MXene has smaller overpotential (286 mV @ 10 mA cm^{-2}), smaller Tafel slope (35 mV dec^{-1}), larger C_{dl} (0.76 mF cm^{-2}) and larger TOF (0.35 s^{-1} @300 mV). DFT calculations show that the synergistic effect of NiFeP and MXene can transfer electrons from NiFeP to MXene, which the large electronegativity of MXene may cause. Compared with the other two samples, the NiFeP/MXene has a higher Fermi level DOS as shown in Fig. 13(a), so the presence of Mxene and phosphating increases the conductivity. In addition, the projected density of states diagram shows that the presence of MXene makes the D-band center of Ni and Fe atoms shift positively as shown in Fig. 13(b), indicating a stronger bonding strength with the intermediate. The charge density distribution diagram in Fig. 13(c, d) shows that electron transfer occurs in NiFe-LDH/MXene, which reduces the electron density of the metal and improves OER activity.

In addition, Liang et al. prepared NiFeCoP/MXene catalysts by hydrothermal and in-situ phosphating strategies [235]. XPS spectra in Fig. 13(e) show that the presence of MXene makes the peaks of Ni^{2+} and Ni^{3+} positively shift. The ratio of Ni^{3+}/Ni^{2+} increased and the valence state of Ni also increased, confirming that MXene promoted the oxidation of metals. In addition, the peak of Ni(OOH) of in-situ Raman spectra of NiFeCoP/MXene is obviously stronger than that of NiFeCoP as shown in Fig. 13(f, g). The peak intensity is further enhanced with the increase of potential, indicating that the coupling of MXene with TMPs can accelerate the formation of active species to facilitate OER process. NiFeCoP/Mxene has excellent OER performance with a η_{10} of 240 mV, a Tafel slope of 55 mV dec^{-1}, a C_{dl} value of 10 mF cm^{-2}, and an LSV curve without attenuation after 500 CV cycles.

4.2.2.2. Carbon layer and carbon nanotube.
Carbon nanomaterials are special among the common conductive substrates. Researchers often combine TMPs with carbon nanomaterials. Benefiting from unique structure of carbon nanomaterials, researchers were able to optimize the electronic structure of the catalyst and expose more active sites. This modulation strategy can be called coupling with carbon nanomaterials. However, the complexity, long time, and high cost of synthesizing these carbon materials have limited the development of this strategy. A common way to achieve this strategy is to physically mix TMP and carbon, and another way to make better electrical contact between the two by in-situ carbonization and phosphine [236].

The carbon nanomaterials chosen by the researchers are often N-doped carbon and carbon nanotubes. Graphite carbon thin layer as a conductive substrate can provide an effective electron transport channel. Su et al. showed that the graphite carbon derived from organic ligands could increase conductivity, protect the catalyst from agglomeration and corrosion, and give it good stability [237]. In general, adding heteroatoms to carbon substrate can accelerate the transfer
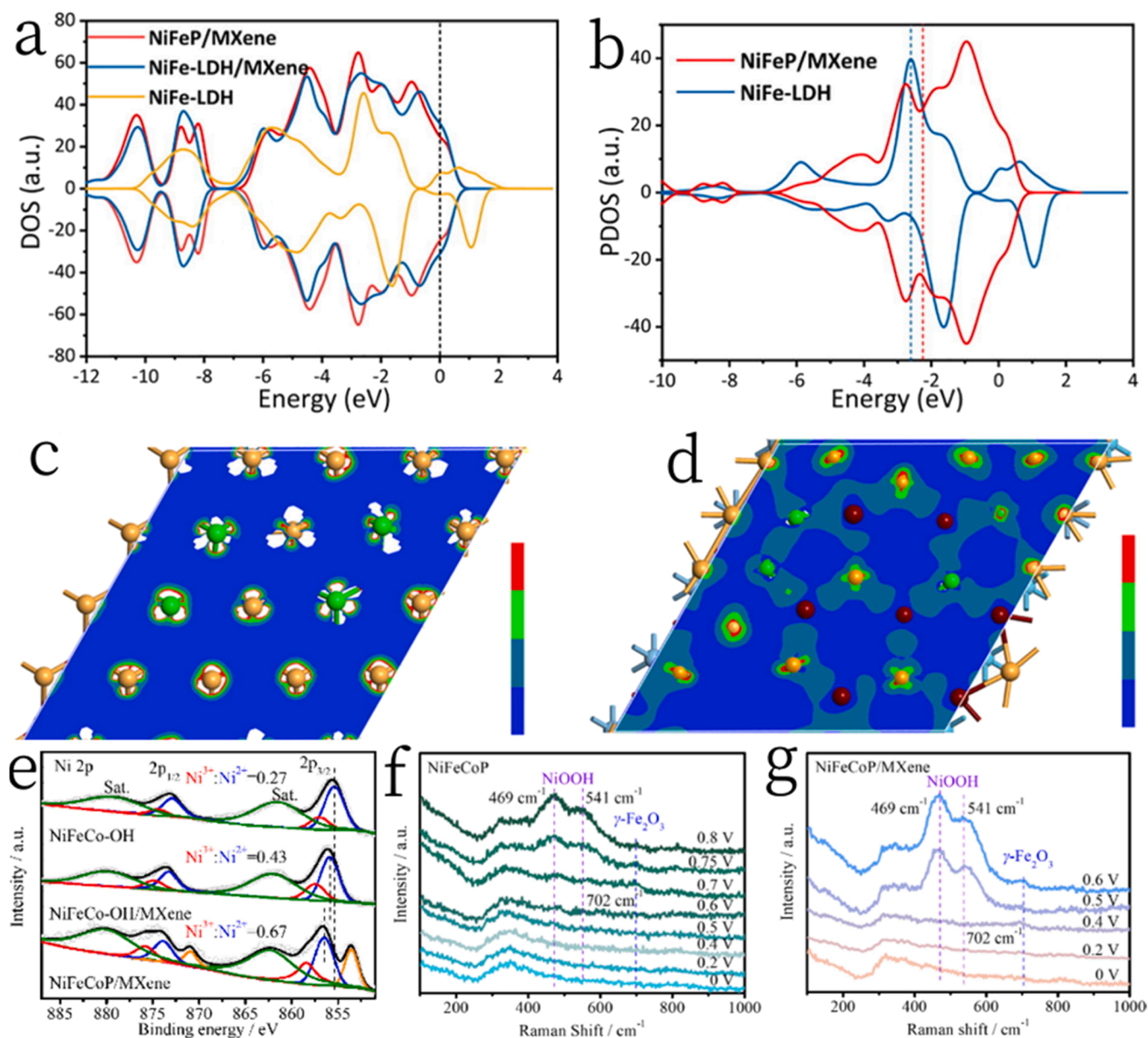
Fig. 13. (a) Density of states of NiFeP/MXene, NiFe-LDH/MXene, and NiFe-LDH (the energy refers to the Fermi level). (b) Projected density of states on to 3d orbitals of Ni and Fe for the NiFeP/MXene and NiFe-LDH nanosheets (the dashed lines indicate D-band centre for each system). (c, d) Charge density distribution plots of (c) NiFe-LDH and (d) NiFeP/MXene. (a-d) Reproduced with permission [234]. Copyright 2021, Elsevier. (e) Ni 2p XPS spectra of NiFeCo-OH, NiFeCo-OH/MXene and NiFeCoP/MXene. In situ Raman spectra of (f) NiFeCoP and (g) NiFeCoP/MXene. (e-g) Reproduced with permission [235]. Copyright 2022, Elsevier.

of electrons from the conductive carbon substrate to the active site. The research of Li et al. shows that doping N in the carbon support can form M-N bond, providing a channel for electron transfer between the active site and the carbon support, thus accelerating the charge transfer of the catalyst [238]. On this basis, Liu et al. prepared the N-doped carbon layer as the functional coating layer of CoP hollow nanorods (CoP-HNTs@NCL) used as OER catalyst [239]. Excellent one-dimensional framework provides a direct channel for mass transfer, and conductive NCL accelerates electron transfer. Bader charge analysis shows that electrons migrate from CoP to NCL, so that obvious charge redistribution occurs in the interface area of CoP/NCL, as shown in Fig. 14(a), resulting in a large number of holes on the surface of CoP HNTs, increasing the number of active sites. Moreover, the shell, as a protective layer, can slow down the dissolution of active phase CoOOH, improving the stability of OER.

It is worth mentioning that Liu et al. pointed out that N, P co doped

carbon has the following three functions: 1) It can be used as a protective layer to protect internal nanoparticles from the corrosion of electrolyte during the catalytic process; 2) The carbon layer can disperse the active sites of the internal heterostructure and prevent agglomeration during the electrocatalysis process; 3) Carbon layer can also promote charge transfer and accelerate reaction kinetics [240]. On this basis, Chen et al. used N, P co-doped carbon coupled with CoP as an excellent OER catalyst (CoP@NPC) [241]. XPS spectra in Fig. 14(b, c) showed that the N and P doping into carbon resulted in stronger polarization between Co and P in CoP so that Co had local positive charge and P had negative charge, which promoted the transfer of charge from Co to P in CoP. The OER catalytic activity of CoP@NPC was tested in 1.0 M KOH with a η_{10} of 300 mV and a Tafel slope of 61.7 mV dec^{-1}.

Carbon nanotubes have a high specific surface area and good mechanical stability, which can provide abundant active sites, provide clear channels to promote mass transfer, thereby enhancing reaction
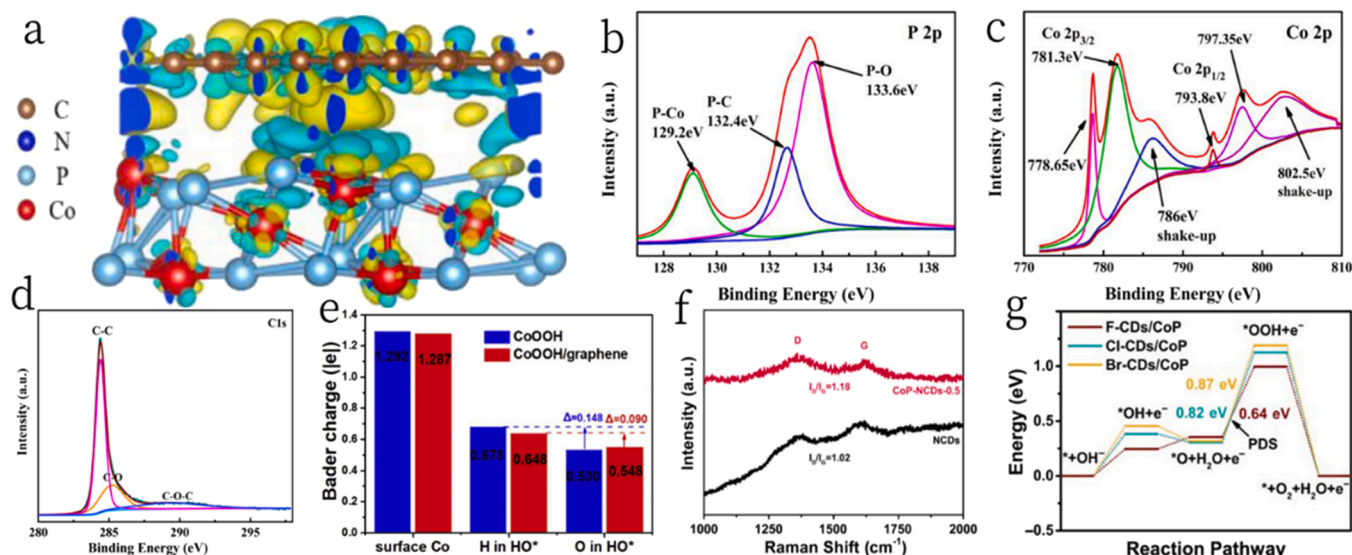
Fig. 14. (a) Charge density difference is obtained by subtracting charge density of isolated pyridinic N-doped carbon and the CoP (111) surface from that of the CoP (111)-NCL interfaces. Cyan and yellow represent charge loss and charge accumulation, respectively. The iso-surface value is set to 0.00038 e/Bohr³. Reproduced with permission [239]. Copyright 2022, Elsevier. High resolution XPS spectra of (b) P 2p and (c) Co 2p in the CoP@NPC. (b-c) Reproduced with permission [241]. Copyright 2019, Elsevier. (d) High resolution XPS spectra of c 1 s of Fe-(NiP$_2$/Ni$_2$P)@CNT-2. Reproduced with permission [242]. Copyright 2022, Elsevier. (e) Bader charge analysis for surface Co ions and H, O in HO* adsorption on pristine and CoOOH/graphene surfaces. Reproduced with permission [243]. Copyright 2019, Elsevier. (f) Raman spectra of CoP-NCDs-0.5 and NCDs. Reproduced with permission [248]. Copyright 2021, Elsevier. (g) Calculated free-energy for OER pathways on X-CDs/CoP (X = F, Cl, and Br) surfaces at U = 1.23 V. Reproduced with permission [249]. Copyright 2022, Wiley-VCH.

kinetics. In addition, combining catalyst nanoparticles with N-doped carbon nanotubes (NCN) can form an electron transfer conductive network, increase the specific surface area and conductivity, and limit the particle size to ensure more active sites [114]. Wang et al. prepared a series of catalysts (Ni$_{2-x}$Fe$_x$P @ NPC) by coupling bimetallic NiFe phosphide with N/P co-doped carbon nanotubes [236]. The coupling of TMP and NPC can re-disperse the active sites and introduce more active species for OER. The C_{dl} and R_{ct} values further confirm that the coupling of TMP with NPC increases the active surface area and accelerates electron transfer. Chen et al. successfully synthesized a CNT-interconnected iron-doped NiP$_2$/Ni$_2$P heterostructure (Fe-(NiP$_2$/-Ni$_2$P)@CNT) [242]. The C 1 s peak at 285.2 eV in the XPS spectrum (Fig. 14(d)) is attributed to point defects, indicating that there are point defects on carbon nanotubes. Fe-(NiP$_2$/Ni$_2$P) nanoparticles are uniformly attached to point defects, which can increase binding energy, thereby improving adhesion and accelerating charge transfer. The OER catalytic activity of Fe-(NiP$_2$/Ni$_2$P)@CNT was tested in 1.0 M KOH. The overpotential at a current density of 10 mA cm^{-2} was 254 mV, and Tafel slope was 46.1 mV dec^{-1}.

The unique bundle-like hierarchical porous structure composed of multi-walled carbon nanotubes (MWCNT) can provide high conductivity, high specific surface area, and fast ion transport channel. Qian et al. reported CNT-NC-CoP nanocomposites [243]. It has excellent OER performance, η_{10} is 251 mV, η_{100} is 377 mV, Tafel slope is 82.1 mV dec^{-1}. Interestingly, researchers ideally viewed CNT-NC as a monolayer of pure graphene, calculating the charge transfer of surface Co ions and H, O in OH* adsorption to highlight the contribution of the carbon substrate to OER performance. As shown in Fig. 14(e), due to the existence of carbon substrate, the Bader charge loss for forming OH* is only 0.090 e, and 0.148 e before doping. This indicates that the presence of carbon substrate accelerates hydroxylation process, which helps to provide active sites for intermediate adsorption. Interestingly, Huang et al. realized that the combination of CoP nanoparticles with carbon nanotubes and nitrogen doped carbon can further play a synergistic role in the preparation of CoP-InNC@CNT [244]. The OER electrocatalytic activity of the catalyst was evaluated in 1.0 M KOH electrolyte. The overpotential of CoP-InNC@CNT at 10 mA cm^{-2} is only 270 mV, and the Tafel slope is

84 mV dec^{-1}. The CoP-InNC@CNT is more OER active than CoP-InNC, which proves that the combination of CNT can further improve OER catalytic performance. The above examples illustrate that selecting carbon nanomaterials as conductive substrates is an effective strategy to improve OER activity.

Worryingly, although the growth of nanostructured phosphides on conductive substrates (such as N-doped carbon and carbon nanotubes) is conductivity, it is easy to peel off from the substrate after a long period of catalytic reaction. However, encapsulating phosphides in porous carbon materials can solve this problem. Jin et al. prepared the ultrafine Co$_2$P nanoparticles (NPs) encapsulated in nitrogen and phosphorus co-doped porous carbon nanosheets/carbon nanotube hybrids (denoted as Co$_2$P @ N, P-PCN/CNTs) [245]. The incorporation of carbon nanotubes provides fast electron transfer ability, and the doping of P can improve conductivity. Co$_2$P NP is evenly embedded in porous carbon nano sheets to expose active sites and prevent aggregation and peeling. The prepared catalyst has a η_{10} of 280 mV, a Tafel slope of 72 mV dec^{-1}.

4.2.2.3. Carbon dots (CDs). It is worth mentioning that carbon dots (CDs) are a new type of zero-dimensional carbon nanomaterials. The internal graphitized core has high conductivity, and the rich functional groups of the shell can be interconnected with metal ions to form a 3D network structure, which can inhibit the agglomeration of nanoparticles and easily combine with other materials to form composite materials [246]. Some functional groups (-OH and -COOH) can also provide active sites. In addition, the small size of carbon dots facilitates their incorporation into various nanostructures for the catalytic action [247].

Like doping N into carbon nanotubes, doping nonmetallic elements into carbon dots can also control catalytic activity. Wu et al. controlled the content of N-doped carbon dots (NCDs) to synthesize a series of CoP-NCDs on nickel foam [248]. The difference in NCD content led to different morphologies of the catalyst. when the addition amount of NCD is 0.5 mg/ml (CoP-NCDs-0.5/NF), the catalyst is fluffy fungal-like, which increases the active surface area and gives the catalyst the best OER activity. The η_{10} was 226 mV and the Tafel slope was 86 mV dec^{-1}. It is better than RuO$_2$ (η_{10} is 191 mV, Tafel slope is 121 mV dec^{-1}), and the presence of CD avoids the dissolution of the catalyst in

agglomeration. Raman spectroscopy in Fig. 14(f) shows that the ID/IG intensity ratio increases after the combination of NCD and CoP, indicating that the defect density increases and the G band redshifts, indicating that there is a strong interaction between NCD and CoP. The excellent OER catalytic activity can be attributed to the increased active surface area after adding NCD and the strong interaction between CoP and NCD. Song et al. reported that halogen doped carbon point modified amorphous cobalt phosphides (X-CDs/CoP) were used as OER catalysts [249]. Among them, F-CDs/CoP/NF has the best OER activity, with a η_{20} of 161 mV and a Tafel slope of 96 mV dec^{-1}. As shown in Fig. 14(g), compared with other X-CD/CoPs, there is an obvious charge transfer between CD and CoP at the F-CD/CoP interface, which leads to a significant reduction in the water decomposition energy of F-CD/CoP (0.95 eV), and the energy barrier required for the potential measurement step (PDS) (O*→OOH*) is also the lowest (0.64 V), so it has excellent OER activity. Unfortunately, there are few studies on the application of carbon dots as phosphide carriers in OER, and further reports are needed.

As mentioned above, exposure to more active sites and expansion of active surface area are also important strategies to improve OER activity. Construction of appropriate nanostructures, such as porous, hollow, unique one-dimensional, two-dimensional and three-dimensional structures, especially ultra-thin nano sheet, core-shell structures, is favored by researchers due to their large surface area. However, fine nanoparticles may still agglomerate to cover the active site, which is often due to the use of adhesives. Therefore, self growing catalysts on suitable conductive substrates can avoid the use of adhesives to expose the active site. Common 3D conductive substrates such as foam nickel, foam copper, carbon cloth, etc. will not be described here, and the emerging two-dimensional materials MXene and zero dimensional materials CDs will be introduced emphatically. However, how to accurately control the synthesis of unique nanostructures remains a difficult problem. Although MXene is an excellent carrier, its high cost limits its development. Further development of carriers with low price and excellent performance is also a challenge. In addition, it is necessary to explore more effective methods to anchor nanoparticles to prevent catalyst agglomeration. Some catalysts prepared for increasing the number of active sites / active surface area are listed in Table 5 for comparisons.

5. Conclusions and prospects

Transition metal phosphides (TMPs) have attracted great interest as bifunctional catalysts for water splitting. Due to the high electronegativity of P, TMP shows excellent HER catalytic performance as a catalyst. However, the OER catalytic performance of TMP does not meet commercial requirements. Therefore, improving the OER catalytic performance of TMP is crucial for efficient water splitting. In this review, we take TMPs as an example to analyze how to prepare highly active OER catalysts. Firstly, the evaluation criteria of OER reaction are introduced to compare the activity of catalysts. Then, how to prepare highly active OER catalysts was analyzed from two aspects: increasing the intrinsic activity of active sites and increasing the number of active sites/active surface area. For the former, it is often necessary to explore ways to make the OER potential close to the thermodynamic limit on the basis of understanding the OER mechanism. Therefore, we first summarize the widely recognized OER mechanism. Then, in order to improve the intrinsic activity of active sites, how to prepare efficient OER catalysts is described from four aspects: optimizing the adsorption and desorption of key intermediates, generating and optimizing vacancies in catalysts, constructing multiple active sites, and promoting the formation of active phases. In order to increase the number of active sites/active surface area, a strategy of constructing unique nanostructures and selecting special carriers was proposed.

Although researchers have made great efforts to prepare highly active OER catalysts, we believe that the current research still has the

Table 5
Comparisons of OER catalytic activities of various TMPs.

Catalyst	Overpotential (mV@mA cm^{-2})	Tafel slope (mV/dec^{-1})	iR compensation	Reference
FeNiP/C-900	229 @ 10	74.5	without	[201]
CoP-NF	323 @ 10	49.6	90%	[202]
Ni-Co-Fe-P	312 @ 50	85.64	with	[203]
Fe-Co-P	269 @ 10	31	with	[205]
NiCoFeP/C	270 @ 10	65	with	[209]
CoFeP TPAs/Ni	250 @ 100	42	with	[210]
Co$_{0.93}$Ni$_{0.07}$P$_3$ NA	221 @ 20	83.7	with	[212]
R-Fe-Ni$_2$P	213 @ 100	50.7	with	[214]
Ni-CoP-5%	290 @ 10	66	unknown	[136]
CoFeP/NF	253 @ 10	36	85%	[218]
CoNi-P-3DHFLM	292 @ 10	84	with	[219]
10FeNiCoP	259 @ 10	40	with	[221]
CoNiFeP-YSNS	261 @ 10	49.5	95%	[222]
O-Co$_2$P/CuO NWs	270 @ 10	74.4	unknown	[225]
NiFeP/MXene	286 @ 10	35	unknown	[234]
NiFeCoP/ MXene	240 @ 10	55	without	[235]
CoP@NPC	300 @ 10	61.7	without	[241]
Fe-(NiP$_2$/Ni$_2$P) @CNT	254 @ 10	46.1	unknown	[242]
CNT-NC-CoP	377 @ 100	82.1	unknown	[243]
CoP-InNC@CNT	270 @ 10	84	without	[244]
Co$_2$P @ NP-PCN/CNT	280 @ 10	72	with	[245]
CoP NCD	226 @ 10	86	without	[248]
F-CD/CoP	161 @ 20	96	with	[249]

Note: in the column of *iR* compensation, "with" represents iR compensation, "without" represents no iR compensation, the percentage represents the percentage of compensation, and "Unknown" represents no clear indication of compensation in the literature.

following problems that need further study:

1) To develop more characterization techniques to explore the mechanism of OER: As mentioned above, the research on the OER mechanism of TMPs is still in its infancy, and more accurate evidence is still needed to explain the exact mechanism of OER. At the same time, clarifying the mechanism is crucial for guiding the development of the next generation of OER catalysts.

2) Conduct electrochemical tests reasonably: As mentioned above, whether iR compensation and compensation percentage greatly affect the size of the overpotential. At the same time, in industrial practical applications, more information comes from data without iR compensation, so researchers should give uncompensated data when reporting. In addition, when the LSV curve is measured, the oxidation peak of the active species will cause the OER overpotential to shift negatively, resulting in an ' imaginary high ' activity. It is recommended to use a ' negative sweep ' to measure the LSV curve to avoid the influence of the oxidation peak.

3) Exploring the optimization of intermediate adsorption by double doping and amorphous state: As mentioned above, element doping and heterostructure construction strategies are widely used to optimize the adsorption of intermediates. Two-element doping in doping seems to be more promising than single-atom doping because of the synergy between different elements, although there are relatively few reports on two-element doping. In addition, common heterostructures focus on electron rearrangement at the interface, while the creation of amorphous and crystalline heterostructures is rarely reported, and the latter also has great potential.

4) Exploring more vacancy types: As mentioned above, the study of vacancy engineering mainly focuses on anionic vacancies, because

anionic vacancies are easier to synthesize than cationic vacancies. However, cation vacancies still play a key role in improving catalytic activity, and more types of cation vacancies should be further studied or catalysts with multiple vacancies should be synthesized.

5) Exploring more multi-metal sites: As mentioned above, there are few reports on the construction of multi-metal sites to enhance OER activity, and how to accurately construct multiple active sites requires more profound theoretical research, which is still a huge challenge.

6) Exploring the formation process of active phase: As mentioned above, researchers need to study other methods to accelerate the formation of active phase. At the same time, the specific formation process of active phase and the role of metastable state still need further study.

7) Explore the controllable synthesis of unique nanostructures: As mentioned above, constructing suitable nanostructures can expose more active sites and expand the active surface area, but precisely controlling the synthesis of unique nanostructures remains a challenge.

8) Explore more emerging conductive substrates: As mentioned above, self-growing catalysts on suitable conductive substrates can avoid the use of adhesives to expose active sites. However, it is still necessary to explore more conductive substrates that can anchor nanoparticles to prevent catalyst agglomeration and promote electron transfer through strong coupling with the catalyst.

CRediT authorship contribution statement

Chen-Jin Huang: Investigation, Formal analysis, Writing – original draft. **Hui-Min Xu**: Resources, Data curation, Visualization. **Ting-Yu Shuai**: Resources, Data curation, Visualization. **Qi-Ni Zhan**: Resources, Data curation, Visualization. **Zhi-Jie Zhang**: Resources, Data curation, Visualization. **Gao-Ren Li**: Conceptualization, Supervision, Funding acquisition, Project administration, Resources, Supervision, Validation, Writing – review & editing.

Declaration of Competing Interest

We declare that we have no known competing financial interests or personal relationships that could have appeared to influence the work reported in this paper.

Data availability

No data was used for the research described in the article.

Acknowledgments

References

[1] S. Chu, A. Majumdar, Opportunities and challenges for a sustainable energy future, Nature 488 (2012) 294–303.

[2] H. Wu, L. Kong, Y. Ji, J. Yan, Y. Ding, Y. Li, S. Lee, S. (Frank) Liu, Double-site Ni–W nanosheet for best alkaline HER performance at high current density >500 mA cm^{-2}, Adv. Mater. Interfaces 6 (2019) 1900308.

[3] Y. Yan, R. Zhang, Y. Yu, Z. Sun, R. Che, B. Wei, A.P. LaGrow, Z. Wang, W. Zhou, Interfacial optimization of PtNi octahedrons@Ti$_3$C$_2$MXene with enhanced alkaline hydrogen evolution activity and stability, Appl. Catal. B Environ. 291 (2021), 120100.

[4] G. Xi, L. Zuo, X. Li, Y. Jin, R. Li, T. Zhang, In-situ constructed Ru-rich porous framework on NiFe-based ribbon for enhanced oxygen evolution reaction in alkaline solution, J. Mater. Sci. Technol. 70 (2021) 197–204.

[5] Y. Lee, J. Suntivich, K.J. May, E.E. Perry, Y. Shao-Horn, Synthesis and activities of rutile IrO$_2$ and RuO$_2$ nanoparticles for oxygen evolution in acid and alkaline solutions, J. Phys. Chem. Lett. 3 (2012) 399–404.

[6] H. Li, S.-M. Xu, H. Yan, L. Yang, S. Xu, Cobalt phosphide composite encapsulated within N,P-doped carbon nanotubes for synergistic oxygen evolution, Small 14 (2018) 1800367.

[7] Y. Huang, Trimetallic spinel NiCo$_2$A$_x$Fe$_x$O$_4$ nanoboxes for highly efficient electrocatalytic oxygen evolution, Angew. Chem. . Ed. 133.21 (2021) 11947–11952.

[8] C.-F. Li, J.-W. Zhao, L.-J. Xie, J.-Q. Wu, G.-R. Li, Water adsorption and dissociation promoted by Co*-/N-C*-biactive sites of metallic Co/N-doped carbon hybrids for efficient hydrogen evolution, Appl. Catal. B: Environ. 282 (2021), 119463.

[9] S.F. Zai, A.Q. Dong, J. Li, Z. Wen, C.C. Yang, Q. Jiang, Low-crystallinity mesoporous NiGaFe hydroxide nanosheets on macroporous Ni foam for high-efficiency oxygen evolution electrocatalysis, J. Mater. Chem. A 9 (2021) 6223–6231.

[10] Y. Lu, Z. Li, Y. Xu, L. Tang, S. Xu, D. Li, J. Zhu, D. Jiang, Bimetallic Co-Mo nitride nanosheet arrays as high-performance bifunctional electrocatalysts for overall water splitting, Chem. Eng. J. 411 (2021), 128433.

[11] S. Ibraheem, G. Yasin, A. Kumar, M.A. Mushtaq, S. Ibrahim, R. Iqbal, M. Tabish, S. Ali, A. Saad, Iron-cation-coordinated cobalt-bridged-selenides nanorods for highly efficient photo/electrochemical water splitting, Appl. Catal. B-Environ. 304 (2022), 120987.

[12] H. Zhang, A.W. Maijenburg, X. Li, S.L. Schweizer, R.B. Wehrspohn, Bifunctional heterostructured transition metal phosphides for efficient electrochemical water splitting, Adv. Funct. Mater. 30 (2020) 2003261.

[13] Y. Yan, P. Wang, J. Lin, J. Cao, J. Qi, Modification strategies on transition metal-based electrocatalysts for efficient water splitting, J. Energy Chem. 58 (2021) 446–462.

[14] P. Liu, J.A. Rodriguez, Catalysts for hydrogen evolution from the [NiFe] hydrogenase to the Ni$_2$P(001) surface: the importance of ensemble effect, J. Am. Chem. Soc. 127 (2005) 14871–14878.

[15] S. Li, L. Wang, H. Su, A.N. Hong, Y. Wang, H. Yang, L. Ge, W. Song, J. Liu, T. Ma, X. Bu, P. Feng, Electron redistributed S-doped nickel iron phosphides derived from one-step phosphatization of MOFs for significantly boosting electrochemical water splitting, Adv. Funct. Mater. 32 (2022) 2200733.

[16] Y. Pan, K. Sun, Y. Lin, X. Cao, Y. Cheng, S. Liu, L. Zeng, W.-C. Cheong, D. Zhao, K. Wu, Z. Liu, Y. Liu, D. Wang, Q. Peng, C. Chen, Y. Li, Electronic structure and d-band center control engineering over M-doped CoP (M = Ni, Mn, Fe) hollow polyhedron frames for boosting hydrogen production, Nano Energy 56 (2019) 411–419.

[17] Y. Li, Z. Dong, L. Jiao, Multifunctional transition metal-based phosphides in energy-related electrocatalysis, Adv. Energy Mater. 10 (2019) 1902104.

[18] Y. Shi, B. Zhang, Recent advances in transition metal phosphide nanomaterials: synthesis and applications in hydrogen evolution reaction, Chem. Soc. Rev. 45 (2016) 1529–1541.

[19] X. Li, Q. Hu, H. Wang, M. Chen, X. Hao, Y. Ma, J. Liu, K. Tang, A. Abudula, G. Guan, Charge induced crystal distortion and morphology remodeling: Formation of Mn-CoP nanowire@Mn-CoOOH nanosheet electrocatalyst with rich edge dislocation defects, Appl. Catal. B. 292 (2021), 120172.

[20] X. Liu, J. Huang, T. Li, W. Chen, G. Chen, L. Han, K. (Ken), Ostrikov, High-efficiency oxygen evolution catalyzed by Sn–Co–Ni phosphide with oriented crystal phases, J. Mater. Chem. A 10 (2022) 13448–13455.

[21] J.F. Callejas, C.G. Read, C.W. Roske, N.S. Lewis, R.E. Schaak, Synthesis, characterization, and properties of metal phosphide catalysts for the hydrogen-evolution reaction, Chem. Mater. 28 (2016) 6017–6044.

[22] M.R. Kandel, U.N. Pan, D.R. Paudel, P.P. Dhakal, N.H. Kim, J.H. Lee, Hybridized bimetallic phosphides of Ni–Mo, Co-Mo, and Co-Ni in a single ultrathin-3D-nanosheets for efficient HER and OER in alkaline media, Compos. Part. B-Eng. 239 (2022).

[23] Y. Jiang, Y. Lu, J. Lin, X. Wang, Z. Shen, A hierarchical MoP nanoflake array supported on ni foam: a bifunctional electrocatalyst for overall water splitting, Small Methods 2 (2018) 1700369.

[24] M. Baek, G. Kim, T. Park, K. Yong, NiMoFe and NiMoFeP as complementary electrocatalysts for efficient overall water splitting and their application in PV-electrolysis with STH 12.3%, Small 15 (2019) 1905501.

[25] Y. Wang, J. Liu, T. Lu, R. He, N. Xu, J. Qiao, Ultra-high voltage efficiency rechargeable zinc-air battery based on high-performance structurally regulated metal-rich nickel phosphides and carbon hybrids bifunctional electrocatalysts, Appl. Catal. B: Environ. 321 (2023), 122041.

[26] B. Liu, R. Wang, Y. Yao, J. Ma, Y. Sun, J. Wan, Y. Zhang, S. Wang, J. Zou, Hollow-structured CoP nanotubes wrapped by N-doped carbon layer with interfacial charges polarization for efficiently boosting oxygen reduction/evolution reactions, Chem. Eng. J. 431 (2022), 133238.

[27] X. Zhou, Y. Zi, L. Xu, T. Li, J. Yang, J. Tang, Core–shell-structured prussian blue analogues ternary metal phosphides as efficient bifunctional electrocatalysts for OER and HER, Inorg. Chem. 60 (2021) 11661–11671.

[28] J.F. Callejas, C.G. Read, C.W. Roske, N.S. Lewis, R.E. Schaak, Synthesis, characterization, and properties of metal phosphide catalysts for the hydrogen-evolution reaction, Chem. Mater. 28 (2016) 6017–6044.

[29] Y. Wang, B. Kong, D. Zhao, H. Wang, C. Selomulya, Strategies for developing transition metal phosphides as heterogeneous electrocatalysts for water splitting, Nano Today 15 (2017) 26–55.

[30] C. Guan, W. Xiao, H. Wu, X. Liu, W. Zang, H. Zhang, J. Ding, Y.P. Feng, S. J. Pennycook, J. Wang, Hollow Mo-doped CoP nanoarrays for efficient overall water splitting, Nano Energy 48 (2018) 73–80.

[31] G. Zhou, M. Li, Y. Li, H. Dong, D. Sun, X. Liu, L. Xu, Z. Tian, Y. Tang, Regulating the electronic structure of CoP nanosheets by O incorporation for high-efficiency electrochemical overall water splitting, Adv. Funct. Mater. 30 (2019) 1905252.

[32] H. Du, Q. Liu, N. Cheng, A.M. Asiri, X. Sun, C.M. Li, Template-assisted synthesis of CoP nanotubes to efficiently catalyze hydrogen-evolving reaction, J. Mater. Chem. A 2 (2014) 14812–14816.

[33] J.-W. Zhao, Z.-X. Shi, C.-F. Li, L.-F. Gu, G.-R. Li, Boosting electrocatalytic performance of NiFe layered double hydroxides for oxygen evolution reaction by exposing the highly active edge plane (012), Chem. Sci. 12 (2021) 650–659.

[34] Z.-X. Shi, J.-W. Zhao, C.-F. Li, H. Xu, G.-R. Li, Fully exposed edge/corner active sites in Fe substituted-Ni(OH)$_2$ tube-in-tube arrays for efficient electrocatalytic oxygen evolution, Appl. Catal. B: Environ. 298 (2021), 120558.

[35] A.B. Laursen, K.R. Patraju, M.J. Whitaker, M. Retuerto, T. Sarkar, N. Yao, K. V. Ramanujachary, M. Greenblatt, G.C. Dismukes, Nanocrystalline Ni$_5$P$_4$: a hydrogen evolution electrocatalyst of exceptional efficiency in both alkaline and acidic media, Energy Environ. Sci. 8 (2015) 1027–1034.

[36] B.K. Kim, S.-K. Kim, S.K. Cho, J.J. Kim, Enhanced catalytic activity of electrodeposited Ni-Cu-P toward oxygen evolution reaction, Appl. Catal. B-Environ. 237 (2018) 409–415.

[37] B.K. Kim, M.J. Kim, J.J. Kim, Modulating the active sites of nickel phosphorous by pulse-reverse electrodeposition for improving electrochemical water splitting, Appl. Catal. B: Environ. 308 (2022), 121226.

[38] Y. Lin, M. Zhang, L. Zhao, L. Wang, D. Cao, Y. Gong, Ru doped bimetallic phosphide derived from 2D metal organic framework as active and robust electrocatalyst for water splitting, Appl. Surf. Sci. 536 (2021), 147952.

[39] S. Anantharaj, P.E. Karthik, S. Noda, The significance of properly reporting turnover frequency in electrocatalysis research, Angew. Chem. -Int. Ed. 60 (2021) 23051–23067.

[40] J. Kibsgaard, C. Tsai, K. Chan, J.D. Benck, J.K. Nørskov, F. Abild-Pedersen, T. F. Jaramillo, Designing an improved transition metal phosphide catalyst for hydrogen evolution using experimental and theoretical trends, Energy Environ. Sci. 8 (2015) 3022–3029.

[41] S. Niu, S. Li, Y. Du, X. Han, P. Xu, How to reliably report the overpotential of an electrocatalyst, ACS Energy Lett. 5 (2020) 1083–1087.

[42] L. Yu, Z. Ren, Systematic study of the influence of iR compensation on water electrolysis, Mater. Today Phys. 14 (2020), 100253.

[43] Y. Lai, Y. Li, L. Jiang, W. Xu, X. Lv, J. Li, Y. Liu, Electrochemical behaviors of co-deposited Pb/Pb–MnO$_2$ composite anode in sulfuric acid solution - Tafel and EIS investigations, J. Electroanal. Chem. 671 (2012) 16–23.

[44] E.J.F. Dickinson, A.J. Wain, The Butler-Volmer equation in electrochemical theory: origins, value, and practical application, J. Electroanal. Chem. 872 (2020), 114145.

[45] C.-F. Li, L.-J. Xie, J.-W. Zhao, L.-F. Gu, H.-B. Tang, L. Zheng, G.-R. Li, Interfacial Fe-O-Ni-O-Fe bonding regulates the active ni sites of ni-mofs via iron doping and decorating with FeOOH for super-efficient oxygen evolution, Angew. Chem. Int. Ed. 61 (2022), e202116934.

[46] J.-W. Zhao, H. Zhang, C.-F. Li, X. Zhou, J.-Q. Wu, F. Zeng, J. Zhang, G.-R. Li, Key roles of surface Fe sites and Sr vacancies in perovskite for efficient oxygen evolution reaction participated by lattice oxygen oxidation, Energy Environ. Sci. 15 (2022) 3912–3922.

[47] C.-F. Li, L.-J. Xie, J.-W. Zhao, L.-F. Gu, J.-Q. Wu, G.-R. Li, Interfacial electronic modulation by Fe$_2$O$_3$/NiFe-LDHs heterostructures for efficient oxygen evolution at high current density, Appl. Catal. B: Environ. 306 (2022), 121097.

[48] C.-F. Li, T. Shuai, L. Zheng, H. Tang, J.-W. Zhao, G.-R. Li, The key role of carboxylate ligands in Ru@MOFs/NF in promoting water dissociation kinetics for effective hydrogen evolution in alkaline media, Chem. Eng. J. 451 (2023), 138618.

[49] S. Anantharaj, S.R. Ede, K. Sakthikumar, K. Karthick, S. Mishra, S. Kundu, Recent trends and perspectives in electrochemical water splitting with an emphasis on sulfide, selenide, and phosphide catalysts of Fe, Co, and Ni: a review, ACS Catal. 6 (2016) 8069–8097.

[50] J.F. Callejas, C.G. Read, E.J. Popczun, J.M. McEnaney, R.E. Schaak, Nanostructured Co$_2$P electrocatalyst for the hydrogen evolution reaction and direct comparison with morphologically equivalent CoP, Chem. Mater. 27 (2015) 3769–3774.

[51] A. Kumar, D.A. Buttry, Size-dependent underpotential deposition of copper on palladium nanoparticles, J. Phys. Chem. C 119 (2015) 16927–16933.

[52] J. Wu, Z. Yu, Y. Zhang, S. Niu, J. Zhao, S. Li, P. Xu, Understanding the effect of second metal on CoM (M = Ni, Cu, Zn) metal–organic frameworks for electrocatalytic oxygen evolution reaction, Small (2021) 2105150.

[53] Q. Liang, L. Zhong, C. Du, Y. Luo, J. Zhao, Y. Zheng, J. Xu, J. Ma, C. Liu, S. Li, Q. Yan, Interfacing epitaxial dinickel phosphide to 2D nickel thiophosphate nanosheets for boosting electrocatalytic water splitting, ACS Nano 13 (2019) 7975–7984.

[54] T. Ul Haq, S.A. Mansour, A. Munir, Y. Haik, Gold-supported gadolinium doped CoB amorphous sheet: a new benchmark electrocatalyst for water oxidation with high turnover frequency, Adv. Funct. Mater. 30 (2020) 1910309.

[55] S. Anantharaj, S. Kundu, Do the evaluation parameters reflect intrinsic activity of electrocatalysts in electrochemical water splitting? ACS Energy Lett. 4 (2019) 1260–1264.

[56] K. Karthick, S. Anantharaj, P.E. Karthik, B. Subramanian, S. Kundu, Self-assembled molecular hybrids of CoS-DNA for enhanced water oxidation with low cobalt content, Inorg. Chem. 56 (2017) 6734–6745.

[57] Z. Abdi, M. Vandichel, A.S. Sologubenko, M.-G. Willinger, J.-R. Shen, S. I. Allakhverdiev, M.M. Najafpour, The importance of identifying the true catalyst

[58] J.G. Vos, M.T.M. Koper, Measurement of competition between oxygen evolution and chlorine evolution using rotating ring-disk electrode voltammetry, J. Electroanal. Chem. 819 (2018) 260–268.

[59] S.-X. Guo, Y. Liu, A.M. Bond, J. Zhang, P. Esakki Karthik, I. Maheshwaran, S. Senthil Kumar, K.L.N. Phani, Facile electrochemical co-deposition of a graphene–cobalt nanocomposite for highly efficient water oxidation in alkaline media: direct detection of underlying electron transfer reactions under catalytic turnover conditions, Phys. Chem. Chem. Phys. 16 (2014) 19035–19045.

[60] S. Anantharaj, S.R. Ede, K. Karthick, S. Sam Sankar, K. Sangeetha, P.E. Karthik, S. Kundu, Precision and correctness in the evaluation of electrocatalytic water splitting: revisiting activity parameters with a critical assessment, Energy Environ. Sci. 11 (2018) 744–771.

[61] T. Naresh Kumar, S. Sivabalan, N. Chandrasekaran, K.L. Phani, Synergism between polyurethane and polydopamine in the synthesis of Ni–Fe alloy monoliths, Chem. Commun. 51 (2015) 1922–1925.

[62] S.-F. Hung, Y. Zhu, G.-Q. Tzeng, H.-C. Chen, C.-S. Hsu, Y.-F. Liao, H. Ishii, N. Hiraoka, H.M. Chen, In situ spatially coherent identification of phosphide-based catalysts: crystallographic latching for highly efficient overall water electrolysis, ACS Energy Lett. 4 (2019) 2813–2820.

[63] J. Wang, C. Chen, N. Cai, M. Wang, H. Li, F. Yu, High topological tri-metal phosphide of CoP@FeNiP toward enhanced activities in oxygen evolution reaction, Nanoscale (2021).

[64] E. Jiang, J. Li, X. Li, A. Ali, G. Wang, S. Ma, P. Kang Shen, J. Zhu, MoP-MO$_2$C quantum dot heterostructures uniformly hosted on a heteroatom-doped 3D porous carbon sheet network as an efficient bifunctional electrocatalyst for overall water splitting, Chem. Eng. J. 431 (2022), 133719.

[65] H. Liao, C. Wei, J. Wang, A. Fisher, T. Sritharan, Z. Feng, Z.J. Xu, A multisite strategy for enhancing the hydrogen evolution reaction on a nano-pd surface in alkaline media, Adv. Energy Mater. 7 (2017) 1701129.

[66] S.-S. Lu, L.-M. Zhang, Y.-W. Dong, J.-Q. Zhang, X.-T. Yan, D.-F. Sun, X. Shang, J.-Q. Chi, Y.-M. Chai, B. Dong, Tungsten-doped Ni–Co phosphides with multiple catalytic sites as efficient electrocatalysts for overall water splitting, J. Mater. Chem. A 7 (2019) 16859–16866.

[67] J. Durst, A. Siebel, C. Simon, F. Hasché, J. Herranz, H.A. Gasteiger, New insights into the electrochemical hydrogen oxidation and evolution reaction mechanism, Energy Environ. Sci. 7 (2014) 2255–2260.

[68] L. Zhao, M. Wen, Y. Tian, Q. Wu, Y. Fu, A novel structure of quasi-monolayered NiCo-bimetal-phosphide for superior electrochemical performance, J. Energy Chem. 74 (2022) 203–211.

[69] J.S. Kim, B. Kim, H. Kim, K. Kang, Recent progress on multimetal oxide catalysts for the oxygen evolution reaction, Adv. Energy Mater. 8 (2018) 1702774.

[70] Q. Liang, G. Brocks, A. Bieberle-Hütter, Oxygen evolution reaction (OER) mechanism under alkaline and acidic conditions, J. Phys. Energy 3 (2021), 026001.

[71] S. Marini, P. Salvi, P. Nelli, R. Pesenti, M. Villa, M. Berrettoni, G. Zangari, Y. Kiros, Advanced alkaline water electrolysis, Electrochim. Acta 82 (2012) 384–391.

[72] A. Indra, U. Paik, T. Song, Boosting electrochemical water oxidation with metal hydroxide carbonate templated prussian blue analogues, Angew. Chem. . Ed. 57.5 (2018) 1241–1245.

[73] Y. Lin, Chromium-ruthenium oxide solid solution electrocatalyst for highly efficient oxygen evolution reaction in acidic media, Nat. Commun. 10.1 (2019) 1–13.

[74] I.C. Man, H. Su, F. Calle-Vallejo, H.A. Hansen, J.I. Martínez, N.G. Inoglu, J. Kitchin, T.F. Jaramillo, J.K. Nørskov, J. Rossmeisl, Universality in oxygen evolution electrocatalysis on oxide surfaces, ChemCatChem 3 (2011) 1159–1165.

[75] J. Rossmeisl, Z.-W. Qu, H. Zhu, G.-J. Kroes, J.K. Nørskov, Electrolysis of water on oxide surfaces, J. Electroanal. Chem. 607 (2007) 83–89.

[76] I.C. Man, H. Su, F. Calle-Vallejo, H.A. Hansen, J.I. Martínez, N.G. Inoglu, J. Kitchin, T.F. Jaramillo, J.K. Nørskov, J. Rossmeisl, Universality in oxygen evolution electrocatalysis on oxide surfaces, ChemCatChem 3 (2011) 1159–1165.

[77] J. Song, C. Wei, Z.-F. Huang, C. Liu, L. Zeng, X. Wang, Z.J. Xu, A review on fundamentals for designing oxygen evolution electrocatalysts, Chem. Soc. Rev. 49 (2020) 2196–2214.

[78] J. Rossmeisl, Z.-W. Qu, H. Zhu, G.-J. Kroes, J.K. Nørskov, Electrolysis of water on oxide surfaces, J. Electroanal. Chem. 607 (2007) 83–89.

[79] M.T.M. Koper, Theory of multiple proton–electron transfer reactions and its implications for electrocatalysis, Chem. Sci. 4 (2013) 2710.

[80] J.R. Petrie, V.R. Cooper, J.W. Freeland, T.L. Meyer, Z. Zhang, D.A. Lutterman, H. N. Lee, Enhanced bifunctional oxygen catalysis in strained LaNiO$_3$ perovskites, J. Am. Chem. Soc. 138 (2016) 2488–2491.

[81] L. Giordano, B. Han, M. Risch, W.T. Hong, R.R. Rao, K.A. Stoerzinger, Y. Shao-Horn, pH dependence of OER activity of oxides: current and future perspectives, Catal. Today 262 (2016) 2–10.

[82] B.J. Trześniewski, O. Diaz-Morales, D.A. Vermaas, A. Longo, W. Bras, M.T. M. Koper, W.A. Smith, In situ observation of active oxygen species in Fe-containing Ni-based oxygen evolution catalysts: the effect of pH on electrochemical activity, J. Am. Chem. Soc. 137 (2015) 15112–15121.

[83] L.-P. Wang, T. Van Voorhis, Direct-coupling O$_2$ bond forming a pathway in cobalt oxide water oxidation catalysts, J. Phys. Chem. Lett. 2 (2011) 2200–2204.

[84] M.G. Mavros, T. Tsuchimochi, T. Kowalczyk, A. McIsaac, L.-P. Wang, T. V. Voorhis, What can density functional theory tell us about artificial catalytic water splitting? Inorg. Chem. 53 (2014) 6386–6397.

[85] J.T. Mefford, X. Rong, A.M. Abakumov, W.G. Hardin, S. Dai, A.M. Kolpak, K. P. Johnston, K.J. Stevenson, Water electrolysis on $La_{1-x}Sr_xCoO_{3-\delta}$ perovskite electrocatalysts, Nat. Commun. 7 (2016).

[86] A. Grimaud, O. Diaz-Morales, B. Han, W.T. Hong, Y.-L. Lee, L. Giordano, K. A. Stoerzinger, M.T.M. Koper, Y. Shao-Horn, Activating lattice oxygen redox reactions in metal oxides to catalyse oxygen evolution, Nat. Chem. 9 (2017) 457–465.

[87] X. Rong, J. Parolin, A.M. Kolpak, A fundamental relationship between reaction mechanism and stability in metal oxide catalysts for oxygen evolution, ACS Catal. 6 (2016) 1153–1158.

[88] C. Lin, J.-L. Li, X. Li, S. Yang, W. Luo, Y. Zhang, S.-H. Kim, D.-H. Kim, S.S. Shinde, Y.-F. Li, Z.-P. Liu, Z. Jiang, J.-H. Lee, In-situ reconstructed Ru atom array on α-MnO_2 with enhanced performance for acidic water oxidation, Nat. Catal. 4 (2021) 1012–1023.

[89] J.S. Yoo, X. Rong, Y. Liu, A.M. Kolpak, Role of lattice oxygen participation in understanding trends in the oxygen evolution reaction on perovskites, ACS Catal. 8 (2018) 4628–4636.

[90] Y. Piao, Synthesis of remarkably thin Co−Fe phosphide/carbon nanosheet for enhanced oxygen evolution reaction electrocatalysis driven by readily generated active oxyhydroxide, ACS Appl. Energy Mater. (2022) 2400–2411.

[91] O. Kasian, Degradation of iridium oxides via oxygen evolution from the lattice: correlating atomic scale structure with reaction mechanisms, Energy Environ. Sci. 12.12 (2019) 3548–3555.

[92] Z. Shi, X. Wang, J. Ge, C. Liu, W. Xing, Fundamental understanding of the acidic oxygen evolution reaction: mechanism study and state-of-the-art catalysts, Nanoscale 12 (2020) 13249–13275.

[93] M. Okamura, M. Kondo, R. Kuga, Y. Kurashige, T. Yanai, S. Hayami, V.K. K. Praneeth, M. Yoshida, K. Yoneda, S. Kawata, S. Masaoka, A pentanuclear iron catalyst designed for water oxidation, Nature 530 (2016) 465–468.

[94] M. Kodera, Y. Kawahara, Y. Hitomi, T. Nomura, T. Ogura, Y. Kobayashi, Reversible O–O bond scission of peroxodiiron(III) to high-spin oxodiiron(IV) in dioxygen activation of a diiron center with a bis-tpa dinucleating ligand as a soluble methane monooxygenase model, J. Am. Chem. Soc. 134 (2012) 13236–13239.

[95] E. Lim, Direct O–O coupling promoted the oxygen evolution reaction by dual active sites from $Ag/LaNiO_3$ interfaces, ACS Appl. Mater. Interfaces (2022).

[96] S. Jin, Are metal chalcogenides, nitrides, and phosphides oxygen evolution catalysts or bifunctional catalysts? ACS Energy Lett. 2 (2017) 1937–1938.

[97] H. Liang, A.N. Gandi, C. Xia, M.N. Hedhili, D.H. Anjum, U. Schwingenschlögl, H. N. Alshareef, Amorphous NiFe-OH/NiFeP electrocatalyst fabricated at low temperature for water oxidation applications, ACS Energy Lett. 2 (2017) 1035–1042.

[98] T.A. Shifa, K. Yusupov, G. Solomon, A. Gradone, R. Mazzaro, E. Cattaruzza, A. Vomiero, In situ-generated oxide in Sn-doped nickel phosphide enables ultrafast oxygen evolution, ACS Catal. 11 (2021) 4520–4529.

[99] X. Wang, W. Li, D. Xiong, D.Y. Petrovykh, L. Liu, Bifunctional nickel phosphide nanocatalysts supported on carbon fiber paper for highly efficient and stable overall water splitting, Adv. Funct. Mater. 26 (2016) 4067–4077.

[100] Y. Li, R. Li, D. Wang, H. Xu, F. Meng, D. Dong, J. Jiang, J. Zhang, M. An, P. Yang, A review: target-oriented transition metal phosphide design and synthesis for water splitting, Int. J. Hydrog. Energy 46 (2021) 5131–5149.

[101] J. Ryu, N. Jung, J.H. Jang, H.-J. Kim, S.J. Yoo, In situ transformation of hydrogen-evolving CoP nanoparticles: toward efficient oxygen evolution catalysts bearing dispersed morphologies with Co-oxo/hydroxo molecular units, ACS Catal. 5 (2015) 4066–4074.

[102] J. Chang, Surface oxidized cobalt-phosphide nanorods as an advanced oxygen evolution catalyst in alkaline solution, ACS Catal. 5 (2015) 6874–6878.

[103] G. Zhang, G. Wang, Y. Liu, H. Liu, J. Qu, J. Li, Highly active and stable catalysts of phytic acid-derivative transition metal phosphides for full water splitting, J. Am. Chem. Soc. 138 (2016) 14686–14693.

[104] J. Ryu, N. Jung, J.H. Jang, H.-J. Kim, S.J. Yoo, In situ transformation of hydrogen-evolving CoP nanoparticles: toward efficient oxygen evolution catalysts bearing dispersed morphologies with co-oxo/hydroxo molecular units, ACS Catal. 5 (2015) 4066–4074.

[105] J.-F. Deng, H. Li, W. Wang, Progress in design of new amorphous alloy catalysts, Catal. Today 51 (1999) 113–125.

[106] Y. Zhao, N. Dongfang, C.A. Triana, C. Huang, R. Erni, W. Wan, J. Li, D. Stoian, L. Pan, P. Zhang, J. Lan, M. Iannuzzi, G.R. Patzke, Dynamics and control of active sites in hierarchically nanostructured cobalt phosphide/chalcogenide-based electrocatalysts for water splitting, Energy Environ. Sci. 15 (2022) 727–739.

[107] K. Xu, H. Cheng, L. Liu, H. Lv, X. Wu, C. Wu, Y. Xie, Promoting active species generation by electrochemical activation in alkaline media for efficient electrocatalytic oxygen evolution in neutral media, Nano Lett. 17 (2016) 578–583.

[108] L.-A. Stern, L. Feng, F. Song, X. Hu, Ni2P as a Janus catalyst for water splitting: the oxygen evolution activity of Ni2P nanoparticles, Energy Environ. Sci. 8 (2015) 2347–2351.

[109] W. Xi, Z. Yan, Z. Lang, Y. Ma, H. Tan, H. Zhu, Y. Wang, Y. Li, Oxygen-doped nickel iron phosphide nanocube arrays grown on Ni foam for oxygen evolution electrocatalysis, Small 14 (2018) 1802204.

[110] L. Yan, B. Zhang, J. Zhu, Y. Li, P. Tsiakaras, P. Kang Shen, Electronic modulation of cobalt phosphide nanosheet arrays via copper doping for highly efficient neutral-pH overall water splitting, Appl. Catal. B: Environ. 265 (2020), 118555.

[111] B. Seo, Y.J. Sa, J. Woo, K. Kwon, J. Park, T.J. Shin, H.Y. Jeong, S.H. Joo, Size-dependent activity trends combined with in Situ X-ray absorption spectroscopy

[112] reveal insights into cobalt oxide/carbon nanotube-catalyzed bifunctional oxygen electrocatalysis, ACS Catal. 6 (2016) 4347–4355.

[112] D. Thiyagarajan, M. Gao, L. Sun, X. Dong, D. Zheng, M. Abdul Wahab, G. Will, J. Lin, Nanoarchitectured porous Cu-CoP nanoplates as electrocatalysts for efficient oxygen evolution reaction, Chem. Eng. J. 432 (2022), 134303.

[113] D. Chen, R. Lu, Z. Pu, J. Zhu, H.-W. Li, F. Liu, S. Hu, X. Luo, J. Wu, Y. Zhao, S. Mu, Ru-doped 3D flower-like bimetallic phosphide with a climbing effect on overall water splitting, Appl. Catal. B Environ. 279 (2020), 119396.

[114] J. Feng, S.-Y. Tong, Y.-X. Tong, G.-R. Li, Pt-like hydrogen evolution electrocatalysis on PANI/CoP hybrid nanowires by weakening the shackles of hydrogen ions on the surfaces of catalysts, J. Am. Chem. Soc. 140 (2018) 5118–5126.

[115] X. Xiao, C.-T. He, S. Zhao, J. Li, W. Lin, Z. Yuan, Q. Zhang, S. Wang, L. Dai, D. Yu, A general approach to cobalt-based homobimetallic phosphide ultrathin nanosheets for highly efficient oxygen evolution in alkaline media, Energy Environ. Sci. 10 (2017) 893–899.

[116] D. Li, H. Baydoun, C.N. Verani, S.L. Brock, Efficient water oxidation using CoMnP nanoparticles, J. Am. Chem. Soc. 138 (2016) 4006–4009.

[117] L. Yan, B. Zhang, J. Zhu, Y. Li, P. Tsiakaras, P. Kang Shen, Electronic modulation of cobalt phosphide nanosheet arrays via copper doping for highly efficient neutral-pH overall water splitting, Appl. Catal. B Environ. 265 (2020), 118555.

[118] S. Sun, X. Zhou, B. Cong, W. Hong, G. Chen, Tailoring the d-band centers endows $(Ni_xFe_{1-x})_2P$ nanosheets with efficient oxygen evolution catalysis, ACS Catal. 10 (2020) 9086–9097.

[119] Y. Jeung, H. Jung, D. Kim, H. Roh, C. Lim, J.W. Han, K. Yong, 2D-structured V-doped Ni(Co,Fe) phosphides with enhanced charge transfer and reactive sites for highly efficient overall water splitting electrocatalysts, J. Mater. Chem. A 9 (2021) 12203–12213.

[120] H. Lee, O. Gwon, K. Choi, L. Zhang, J. Zhou, J. Park, J.-W. Yoo, J.-Q. Wang, J. H. Lee, G. Kim, Enhancing bifunctional electrocatalytic activities via metal d-band center lift induced by oxygen vacancy on the subsurface of perovskites, ACS Catal. 10 (2020) 4664–4670.

[121] H. Roh, H. Jung, H. Choi, J.W. Han, T. Park, S. Kim, K. Yong, Various metal (Fe, Mo, V, Co)-doped Ni2P nanowire arrays as overall water splitting electrocatalysts and their applications in unassisted solar hydrogen production with STH 14%, Appl. Catal. B: Environ. 297 (2021), 120434.

[122] Y. Liu, N. Ran, R. Ge, J. Liu, W. Li, Y. Chen, L. Feng, R. Che, Porous Mn-doped cobalt phosphide nanosheets as highly active electrocatalysts for oxygen evolution reaction, Chem. Eng. J. 425 (2021), 131642.

[123] D. Chen, R. Lu, Z. Pu, J. Zhu, H.-W. Li, F. Liu, S. Hu, X. Luo, J. Wu, Y. Zhao, S. Mu, Ru-doped 3D flower-like bimetallic phosphide with a climbing effect on overall water splitting, Appl. Catal. B Environ. 279 (2020), 119396.

[124] Y. Zhao, M. Luo, S. Chu, M. Peng, B. Liu, Q. Wu, P. Liu, F.M.F. de Groot, Y. Tan, 3D nanoporous iridium-based alloy microwires for efficient oxygen evolution in acidic media, Nano Energy 59 (2019) 146–153.

[125] R.-Q. Li, B.-L. Wang, T. Gao, R. Zhang, C. Xu, X. Jiang, J. Zeng, Y. Bando, P. Hu, Y. Li, X.-B. Wang, Monolithic electrode integrated of ultrathin NiFeP on 3D strutted graphene for bifunctionally efficient overall water splitting, Nano Energy 58 (2019) 870–876.

[126] Y. Liu, Z. Zhang, L. Zhang, Y. Xia, H. Wang, H. Liu, S. Ge, J. Yu, Manipulating the d-band centers of transition metal phosphides through dual metal doping towards robust overall water splitting, J. Mater. Chem. A 10 (2022) 22125–22134.

[127] X. Jiang, X. Yue, Y. Li, X. Wei, Q. Zheng, F. Xie, D. Lin, G. Qu, Anion-cation-dual doped tremella-like nickel phosphides for electrocatalytic water oxidation, Chem. Eng. J. 426 (2021), 130718.

[128] Y. Sun, T. Liu, Z. Li, A. Meng, G. Li, L. Wang, S. Li, Morphology and interfacial charge regulation strategies constructing 3D flower-like Co@CoP2 heterostructure electrocatalyst for efficient overall water splitting, Chem. Eng. J. 433 (2022), 133684.

[129] X. Ding, J. Yu, W. Huang, D. Chen, W. Lin, Z. Xie, Modulation of the interfacial charge density on Fe2P–CoP by coupling CeO2 for accelerating alkaline electrocatalytic hydrogen evolution reaction and overall water splitting, Chem. Eng. J. 451 (2023), 138550.

[130] H. Liu, J. Gao, X. Xu, Q. Jia, L. Yang, S. Wang, D. Cao, Oriented construction Cu3P and Ni2P heterojunction to boost overall water splitting, Chem. Eng. J. 448 (2022), 137706.

[131] V.L. Deringer, A.L. Tchougréeff, R. Dronskowski, Crystal orbital hamilton population (COHP) analysis as projected from plane-wave basis sets, J. Phys. Chem. A 115 (2011) 5461–5466.

[132] Y. Zhang, H. Liu, R. Ge, J. Yang, S. Li, Y. Liu, L. Feng, Y. Li, M. Zhu, W. Li, Mo-induced in-situ architecture of Ni_xCo_yP/CoP heterostructure nano-networks on nickel foam as bifunctional electrocatalysts for overall water splitting, Sustain. Mater. Technol. 33 (2022), e00461.

[133] Z. Jin, P. Li, D. Xiao, Metallic CO2P ultrathin nanowires distinguished from CoP as robust electrocatalysts for overall water-splitting, Green. Chem. 18 (2016) 1459–1464.

[134] D. Kong, H. Wang, Z. Lu, Y. Cui, CoSe2 nanoparticles grown on carbon fiber paper: an efficient and stable electrocatalyst for hydrogen evolution reaction, J. Am. Chem. Soc. 136 (2014) 4897–4900.

[135] G. Zhang, Y. Li, X. Xiao, Y. Shan, Y. Bai, H.-G. Xue, H. Pang, Z. Tian, Q. Xu, In situ anchoring polymetallic phosphide nanoparticles within porous prussian blue analogue nanocages for boosting oxygen evolution catalysis, Nano Lett. 21 (2021) 3016–3025.

[136] Y. Zhao, J. Zhang, Y. Xie, B. Sun, J. Jiang, W.-J. Jiang, S. Xi, H.Y. Yang, K. Yan, S. Wang, X. Guo, P. Li, Z. Han, X. Lu, H. Liu, G. Wang, Constructing atomic heterometallic sites in ultrathin nickel-incorporated cobalt phosphide nanosheets

via a boron-assisted strategy for highly efficient water splitting, Nano Lett. (2021).

[137] G. Wu, X. Zheng, P. Cui, H. Jiang, X. Wang, Y. Qu, W. Chen, Y. Lin, H. Li, X. Han, Y. Hu, P. Liu, Q. Zhang, J. Ge, Y. Yao, R. Sun, Y. Wu, L. Gu, X. Hong, Y. Li, A general synthesis approach for amorphous noble metal nanosheets, Nat. Commun. 10 (2019) 4855.

[138] D. Bhutani, S. Maity, S. Chaturvedi, D. Chalapathi, U.V. Waghmare, C. Narayana, V.C. Prabhakaran, E. Muthusamy, Heterostructure from heteromixture: unusual OER activity of FeP and CoP nanostructures on physical mixing, J. Mater. Chem. A 10 (2022) 22354–22362.

[139] P. Wang, Z. Pu, W. Li, J. Zhu, C. Zhang, Y. Zhao, S. Mu, Coupling NiSe$_2$-Ni$_2$P heterostructure nanowrinkles for highly efficient overall water splitting, J. Catal. 377 (2019) 600–608.

[140] H.-Y. Wang, J.-T. Ren, L. Wang, M.-L. Sun, H.-M. Yang, X.-W. Lv, Z.-Y. Yuan, Synergistically enhanced activity and stability of bifunctional nickel phosphide/sulfide heterointerface electrodes for direct alkaline seawater electrolysis, J. Energy Chem. 75 (2022) 66–73.

[141] J. He, Y. Zou, S. Wang, Defect engineering on electrocatalysts for gas-evolving reactions, Dalton Trans. 48 (2019) 15–20.

[142] G. Yuan, J. Bai, L. Zhang, X. Chen, L. Ren, The effect of P vacancies on the activity of cobalt phosphide nanorods as oxygen evolution electrocatalyst in alkali, Appl. Catal. B Environ. 284 (2021), 119693.

[143] S. Li, Z. Geng, X. Wang, X. Ren, J. Liu, X. Hou, Y. Sun, W. Zhang, K. Huang, S. Feng, Optimizing the surface state of cobalt-iron bimetallic phosphide via regulating phosphorus vacancies, Chem. Commun. 56 (2020) 2602–2605.

[144] G. Ye, Y. Gong, J. Lin, B. Li, Y. He, S.T. Pantelides, W. Zhou, R. Vajtai, P. M. Ajayan, Defects engineered monolayer MoS$_2$ for improved hydrogen evolution reaction, Nano Lett. 16 (2016) 1097–1103.

[145] Y. Zhao, X. Zhang, X. Jia, G.I.N. Waterhouse, R. Shi, X. Zhang, F. Zhan, Y. Tao, L.-Z. Wu, C.-H. Tung, D. O'Hare, T. Zhang, Sub-3 nm ultrafine monolayer layered double hydroxide nanosheets for electrochemical water oxidation, Adv. Energy Mater. 8 (2018) 1703585.

[146] Y. Wang, Layered double hydroxide nanosheets with multiple vacancies obtained by dry exfoliation as highly efficient oxygen evolution electrocatalysts, Angew. Chem. . Ed. 56.21 (2017) 5867–5871.

[147] J. Qi, T. Xu, J. Cao, S. Guo, Z. Zhong, J. Feng, Fe doped Ni$_5$P$_4$ nanosheet arrays with rich P vacancies via phase transformation for efficient overall water splitting, Nanoscale 12 (2020) 6204–6210.

[148] Y. Hou, M. Qiu, T. Zhang, X. Zhuang, C.-S. Kim, C. Yuan, X. Feng, Ternary porous cobalt phosphoselenide nanosheets: an efficient electrocatalyst for electrocatalytic and photoelectrochemical water splitting, Adv. Mater. 29 (2017) 1701589.

[149] N. Yao, R. Meng, F. Wu, Z. Fan, G. Cheng, W. Luo, Oxygen-vacancy-induced CeO$_2$/Co$_4$N heterostructures toward enhanced pH-Universal hydrogen evolution reactions, Appl. Catal. B: Environ. 277 (2020), 119282.

[150] X. Zhou, H. Gao, Y. Wang, Z. Liu, J. Lin, Y. Ding, P vacancies-enriched 3D hierarchical reduced cobalt phosphide as a precursor template for defect engineering for efficient water oxidation, J. Mater. Chem. A 6 (2018) 14939–14948.

[151] J. Yin, J. Li, F. Lv, M. Lu, K. Sun, W. Wang, L. Wang, F. Cheng, Y. Li, P. Xi, S. Guo, Oxygen vacancies dominated NiS$_2$/CoS$_2$ interface porous nanowires for portable Zn-Air batteries driven water splitting devices, Adv. Mater. 29 (2017) 1704681.

[152] R. Zhang, Y.-C. Zhang, L. Pan, G.-Q. Shen, N. Mahmood, Y.-H. Ma, Y. Shi, W. Jia, L. Wang, X. Zhang, W. Xu, J.-J. Zou, Engineering cobalt defects in cobalt oxide for highly efficient electrocatalytic oxygen evolution, ACS Catal. 8 (2018) 3803–3811.

[153] Z. Shao, J. Sun, N. Guo, F. He, K. Huang, F. Tian, Q. Wang, Boosting electrocatalysis by heteroatom doping and oxygen vacancies in hierarchical Ni-Co based nitride phosphide hybrid, J. Power Sources 422 (2019) 33–41.

[154] J. Qi, T. Xu, J. Cao, S. Guo, Z. Zhong, J. Feng, Fe doped Ni$_5$P$_4$ nanosheet arrays with rich P vacancies via phase transformation for efficient overall water splitting, Nanoscale 12 (2020) 6204–6210.

[155] Y. Yan, J. Lin, J. Cao, S. Guo, X. Zheng, J. Feng, J. Qi, Activating and optimizing the activity of NiCoP nanosheets for electrocatalytic alkaline water splitting through the V doping effect enhanced by P vacancies, J. Mater. Chem. A 7 (2019) 24486–24492.

[156] Y. Dong, X. Chen, B. Yu, W. Zhang, X. Zhu, Z. Liu, Engineering of P vacancies and phosphate on Fe-doped Ni$_2$P nanosheet arrays for enhanced oxygen evolution, J. Alloy. Compd. 905 (2022), 164023.

[157] T. Xu, D. Jiao, L. Zhang, H. Zhang, L. Zheng, D.J. Singh, J. Zhao, W. Zheng, X. Cui, Br-induced P-poor defective nickel phosphide for highly efficient overall water splitting, Appl. Catal. B: Environ. 316 (2022), 121686.

[158] J. Lin, Y. Yan, T. Xu, J. Cao, X. Zheng, J. Feng, J. Qi, Rich P vacancies modulate Ni$_2$P/Cu$_3$P interfaced nanosheets for electrocatalytic alkaline water splitting, J. Colloid Interface Sci. 564 (2020) 37–42.

[159] C.-F. Li, J.-W. Zhao, L.-J. Xie, J.-Q. Wu, G.-R. Li, Fe doping and oxygen vacancy modulated Fe-Ni$_5$P$_4$/NiFeOH nanosheets as bifunctional electrocatalysts for efficient overall water splitting, Appl. Catal. B: Environ. 291 (2021) 119987.

[160] Z. Shao, H. Qi, X. Wang, J. Sun, N. Guo, K. Huang, Q. Wang, Boosting oxygen evolution by surface nitrogen doping and oxygen vacancies in hierarchical NiCo/NiCoP hybrid nanocomposite, Electrochim. Acta 296 (2019) 259–267.

[161] M. Gao, Z. Wang, S. Sun, D. Jiang, M. Chen, Interfacial engineering of CeO$_2$ on NiCoP nanoarrays for efficient electrocatalytic oxygen evolution, Nanotechnology 32 (2021), 195704.

[162] T. Wang, X. Li, Y. Pang, X. Gao, Z. Kou, J. Tang, J. Wang, Unlocking the synergy of interface and oxygen vacancy by core-shell nickel phosphide@oxyhydroxide

[163] nanosheets arrays for accelerating alkaline oxygen evolution kinetics, Chem. Eng. J. 425 (2021), 131491.

[163] W.-Z. Zhang, G.-Y. Chen, J. Zhao, J.-C. Liang, L.-F. Sun, G.-F. Liu, B.-W. Ji, X.-Y. Yan, J.-R. Zhang, Self-growth Ni$_2$P nanosheet arrays with cationic vacancy defects as a highly efficient bifunctional electrocatalyst for overall water splitting, J. Colloid Interface Sci. 561 (2020) 638–646.

[164] T. Chen, B. Li, K. Song, C. Wang, J. Ding, E. Liu, B. Chen, F. He, Defect-activated surface reconstruction: mechanism for triggering the oxygen evolution reaction activity of NiFe phosphide, J. Mater. Chem. A 10 (2022) 22750–22759.

[165] L. Peng, N. Yang, Y. Yang, Q. Wang, X. Xie, D. Sun-Waterhouse, L. Shang, T. Zhang, G.I.N. Waterhouse, Atomic cation-vacancy engineering of NiFe-layered double hydroxides for improved activity and stability towards the oxygen evolution reaction, Angew. Chem. Int. Ed. 60 (2021) 24612–24619.

[166] S. Choi, Y. Park, H. Yang, H. Jin, G.M. Tomboc, K. Lee, Vacancy-engineered catalysts for water electrolysis, CrystEngComm 22 (2020) 1500–1513.

[167] D. Gao, B. Xia, Y. Wang, W. Xiao, P. Xi, D. Xue, J. Ding, Dual-native vacancy activated basal plane and conductivity of MoSe$_2$ with high-efficiency hydrogen evolution reaction, Small 14 (2018) 1704150.

[168] W.L. Kwong, E. Gracia-Espino, C.C. Lee, R. Sandström, T. Wågberg, J. Messinger, Cationic vacancy defects in iron phosphide: a promising route toward efficient and stable hydrogen evolution by electrochemical water splitting, ChemSusChem 10 (2017) 4544–4551.

[169] Y. Liu, H.T.D. Bui, A.R. Jadhav, T. Yang, S. Saqlain, Y. Luo, J. Yu, A. Kumar, H. Wang, L. Wang, V.Q. Bui, M.G. Kim, Y.D. Kim, H. Lee, Revealing the synergy of cation and anion vacancies on improving overall water splitting kinetics, Adv. Funct. Mater. (2021) 2010718.

[170] S. Wen, J. Huang, T. Li, W. Chen, G. Chen, Q. Zhang, X. Zhang, Q. Qian, K. Ken Ostrikov, Multiphase nanosheet-nanowire cerium oxide and nickel-cobalt phosphide for highly-efficient electrocatalytic overall water splitting, Appl. Catal. B Environ. 316 (2022) 121678.

[171] L. Zhou, M. Shao, J. Li, S. Jiang, M. Wei, X. Duan, Two-dimensional ultrathin arrays of CoP: electronic modulation toward high performance overall water splitting, Nano Energy 41 (2017) 583–590.

[172] R. Zhang, X. Wang, S. Yu, T. Wen, X. Zhu, F. Yang, X. Sun, X. Wang, W. Hu, Ternary NiCo$_2$P$_x$Nanowires as pH-universal electrocatalysts for highly efficient hydrogen evolution reaction, Adv. Mater. 29 (2016) 1605502.

[173] P. Jiang, Q. Liu, Y. Liang, J. Tian, A.M. Asiri, X. Sun, A cost-effective 3D hydrogen evolution cathode with high catalytic activity: FeP Nanowire array as the active phase, Angew. Chem. Int. Ed. 53 (2014) 12855–12859.

[174] L. Yan, L. Cao, P. Dai, X. Gu, D. Liu, L. Li, Y. Wang, X. Zhao, Metal-organic frameworks derived nanotube of nickel-cobalt bimetal phosphides as highly efficient electrocatalysts for overall water splitting, Adv. Funct. Mater. 27 (2017) 1703455.

[175] T. Grant Glover, G.W. Peterson, B.J. Schindler, D. Britt, O. Yaghi, MOF-74 building unit has a direct impact on toxic gas adsorption, Chem. Eng. Sci. 66 (2011) 163–170.

[176] W. Zhou, M. Wu, G.-R. Li, Rambutan-like CoP@Mo-Co-O hollow microspheres for efficient hydrogen evolution reaction in alkaline solution, Chin. J. Catal. 41 (2020) 691–697.

[177] J. Yu, Q. Li, Y. Li, C.-Y. Xu, L. Zhen, V.P. Dravid, J. Wu, Ternary metal phosphide with triple-layered structure as a low-cost and efficient electrocatalyst for bifunctional water splitting, Adv. Funct. Mater. 26 (2017) 7644–7651.

[178] V.H. Hoa, S. Prabhakaran, K.T. Nhi Le, D.H. Kim, A single atom Ir doped heterophase of a NiMoP-NiMoP$_x$O$_y$ ultrathin layer assembled on CNTs-graphene for high-performance water splitting, J. Mater. Chem. A 10 (2022) 14604–14612.

[179] Y.-J. Tang, Y. Zou, D. Zhu, Efficient water oxidation using an Fe-doped nickel telluride–nickel phosphide electrocatalyst by partial phosphating, J. Mater. Chem. A 10 (2022) 12438–12446.

[180] Y. Li, X. Du, J. Huang, C. Wu, Y. Sun, G. Zou, C. Yang, J. Xiong, Recent progress on surface reconstruction of earth-abundant electrocatalysts for water oxidation, Small 15 (2019) 1901980.

[181] Q. Fu, Phase-junction electrocatalysts towards enhanced hydrogen evolution reaction in alkaline media, Angew. Chem. . Ed. 133.1 (2021) 263–271.

[182] Y. Zhang, L. Gao, E.J.M. Hensen, J.P. Hofmann, Evaluating the stability of Co$_2$P electrocatalysts in the hydrogen evolution reaction for both acidic and alkaline electrolytes, ACS Energy Lett. 3 (2018) 1360–1365.

[183] T.N. Batugedara, S.L. Brock, Role of noble- and base-metal speciation and surface segregation in Ni$_{2-x}$Rh$_x$P nanocrystals on electrocatalytic water splitting reactions in alkaline media, Chem. Mater. 34 (2022) 4414–4427.

[184] M. Jiang, J. Li, J. Li, Y. Zhao, L. Pan, Q. Cao, D. Wang, Y. Du, Two-dimensional bimetallic phosphide ultrathin nanosheets as non-noble electrocatalysts for a highly efficient oxygen evolution reaction, Nanoscale 11 (2019) 9654–9660.

[185] Y. Wang, M. Xie, F. Dai, J. Liu, L. Zhang, R. Zhang, Z. Zhang, W. Hu, Iron regulates the interfacial charge distribution of transition metal phosphides for enhanced oxygen evolution reaction, J. Colloid Interface Sci. 615 (2022) 725–731.

[186] F. Chen, Z. Zhang, W. Liang, X. Qin, Z. Zhang, L. Jiang, Synthesis of Co$_4$S$_3$/Co$_9$S$_8$ nanosheets and comparison study toward the OER properties induced by different metal ion doping, Chin. Chem. Lett. 33 (2022) 1395–1402.

[187] C. Wang, W. Chen, D. Yuan, S. Qian, D. Cai, J. Jiang, S. Zhang, Tailoring the nanostructure and electronic configuration of metal phosphides for efficient electrocatalytic oxygen evolution reactions, Nano Energy 69 (2020), 104453.

[188] J. Chang, Y. Xiao, M. Xiao, J. Ge, C. Liu, W. Xing, Surface oxidized cobalt-phosphide nanorods as an advanced oxygen evolution catalyst in alkaline solution, ACS Catal. 5 (2015) 6874–6878.

[189] S. Sarkar, L. Dheer, C.P. Vinod, R. Thapa, U.V. Waghmare, S.C. Peter, Stress-induced electronic structure modulation of manganese-incorporated ni2p leading to enhanced activity for water splitting, ACS Appl. Energy Mater. 3 (2020) 1271–1278.

[190] M. Wang, C.-L. Dong, Y.-C. Huang, Y. Li, S. Shen, Electronic structure evolution in tricomponent metal phosphides with reduced activation energy for efficient electrocatalytic oxygen evolution, Small 14 (2018) 1801756.

[191] M. Chen, H. Li, C. Wu, Y. Liang, J. Qi, J. Li, E. Shangguan, W. Zhang, R. Cao, Interfacial engineering of heterostructured Co(OH)$_2$/NiP$_x$ nanosheets for enhanced oxygen evolution reaction, Adv. Funct. Mater. 32 (2022) 2206407.

[192] Y. Wang, Construction of Ru/FeCoP heterointerface to drive dual active site mechanism for efficient overall water splitting, J. Mater. Chem. A 10.30 (2022) 16071–16079.

[193] H. Chu, P. Feng, B. Jin, G. Ye, S. Cui, M. Zheng, G.-X. Zhang, M. Yang, In-situ release of phosphorus combined with rapid surface reconstruction for Co–Ni bimetallic phosphides boosting efficient overall water splitting, Chem. Eng. J. 433 (2022), 133523.

[194] Y. Li, Y. Wu, H. Hao, M. Yuan, Z. Lv, L. Xu, B. Wei, In situ unraveling surface reconstruction of Ni$_5$P$_4$@FeP nanosheet array for superior alkaline oxygen evolution reaction, Appl. Catal. B Environ. 305 (2022) 121033.

[195] K. Zhu, W. Luo, G. Zhu, J. Wang, Y. Zhu, Z. Zou, W. Huang, Interface-engineered Ni(OH)$_2$/β-like FeOOH electrocatalysts for highly efficient and stable oxygen evolution reaction, Chem. Asian J. 12 (2017) 2720–2726.

[196] F. Zhang, Y. Shi, T. Xue, J. Zhang, Y. Liang, B. Zhang, In situ electrochemically converting Fe$_2$O$_3$-Ni(OH)$_2$ to NiFe$_2$O$_4$-NiOOH: a highly efficient electrocatalyst towards water oxidation, Sci. China Mater. 60 (2017) 324–334.

[197] W. Chu, Z. Shi, Y. Hou, D. Ma, X. Bai, Y. Gao, N. Yang, Trifunctional of phosphorus-doped NiCo$_2$O$_4$ nanowire materials for asymmetric supercapacitor, oxygen evolution reaction, and hydrogen evolution reaction, ACS Appl. Mater. Interfaces 12 (2019) 2763–2772.

[198] B.S. Yeo, A.T. Bell, Enhanced activity of gold-supported cobalt oxide for the electrochemical evolution of oxygen, J. Am. Chem. Soc. 133 (2011) 5587–5593.

[199] S.C. Sekhar, B. Ramulu, M.H. Han, S.J. Arbaz, M. Nagaraju, H. Oh, J.S. Yu, Unraveling CoNiP-CoP$_2$ 3D-on-1D hybrid nanoarchitecture for long-lasting electrochemical hybrid cells and oxygen evolution reaction, Adv. Sci. 9 (2022) 2104877.

[200] M. Liu, J. Li, Cobalt phosphide hollow polyhedron as efficient bifunctional electrocatalysts for the evolution reaction of hydrogen and oxygen, ACS Appl. Mater. Interfaces 8 (2016) 2158–2165.

[201] X. Wang, L. Chai, J. Ding, L. Zhong, Y. Du, T.-T. Li, Y. Hu, J. Qian, S. Huang, Chemical and morphological transformation of MOF-derived bimetallic phosphide for efficient oxygen evolution, Nano Energy 62 (2019) 745–753.

[202] L. Ji, J. Wang, X. Teng, T.J. Meyer, Z. Chen, CoP nanoframes as bifunctional electrocatalysts for efficient overall water splitting, ACS Catal. 10 (2019) 412–419.

[203] Y. Wang, Y. Wang, H. Gao, Z. Huang, Q. Hao, B. Liu, Interface-induced contraction of core–shell Prussian blue analogues toward hollow Ni-Co-Fe phosphide nanoboxes for efficient oxygen evolution electrocatalysis, Chem. Eng. J. 451 (2023) 138515.

[204] P. Li, H.C. Zeng, Promoting electrocatalytic oxygen evolution over transition-metal phosphide-based nanocomposites via architectural and electronic engineering, ACS Appl. Mater. Interfaces 11 (2019) 46825–46838.

[205] H. Zhang, W. Zhou, J. Dong, X.F. Lu, X.W. (David) Lou, Intramolecular electronic coupling in porous iron cobalt (oxy)phosphide nanoboxes enhances the electrocatalytic activity for oxygen evolution, Energy Environ. Sci. 12 (2019) 3348–3355.

[206] A. Meena, P. Thangavel, D.S. Jeong, A.N. Singh, A. Jana, H. Im, D.A. Nguyen, K. S. Kim, Crystalline-amorphous interface of mesoporous Ni$_2$P @ FePO$_x$H$_y$ for oxygen evolution at high current density in alkaline-anion-exchange-membrane water-electrolyzer, Appl. Catal. B: Environ. 306 (2022), 121127.

[207] L. Yang, H. Ren, Q. Liang, K.N. Dinh, R. Dangol, Q. Yan, Ultrathin amorphous nickel doped cobalt phosphates with highly ordered mesoporous structures as efficient electrocatalyst for oxygen evolution reaction, Small 16 (2020) 1906766.

[208] C.M.A. Parlett, K. Wilson, A.F. Lee, Hierarchical porous materials: catalytic applications, Chem. Soc. Rev. 42 (2013) 3876–3893.

[209] X. Wei, Y. Zhang, H. He, L. Peng, S. Xiao, S. Yao, P. Xiao, Carbon-incorporated porous honeycomb NiCoFe phosphide nanospheres derived from a MOF precursor for overall water splitting, Chem. Commun. 55 (2019) 10896–10899.

[210] L. Zhang, X. Wang, A. Li, X. Zheng, L. Peng, J. Huang, Z. Deng, H. Chen, Z. Wei, Rational construction of macroporous CoFeP triangular plate arrays from bimetal–organic frameworks as high-performance overall water-splitting catalysts, J. Mater. Chem. A 7 (2019) 17529–17535.

[211] T. Wu, M. Pi, D. Zhang, S. Chen, 3D structured porous CoP$_3$ nanoneedle arrays as an efficient bifunctional electrocatalyst for the evolution reaction of hydrogen and oxygen, J. Mater. Chem. A 4 (2016) 14539–14544.

[212] Q. Fu, T. Wu, G. Fu, T. Gao, J. Han, T. Yao, Y. Zhang, W. Zhong, X. Wang, B. Song, Skutterudite-type ternary Co$_{1-x}$Ni$_x$P$_3$ nanoneedle array electrocatalysts for enhanced hydrogen and oxygen evolution, ACS Energy Lett. 3 (2018) 1744–1752.

[213] X. Qin, B. Yan, D. Kim, Z. Teng, T. Chen, J. Choi, L. Xu, Y. Piao, Interfacial engineering and hydrophilic/aerophobic tuning of Sn$_4$P$_3$/CO$_2$P heterojunction nanoarrays for high-efficiency fully reversible water electrolysis, Appl. Catal. B Environ. 304 (2022) 120923.

[214] M. Li, J. Wang, X. Guo, J. Li, Y. Huang, S. Geng, Y. Yu, Y. Liu, W. Yang, Structural engineering of Fe-doped Ni$_2$P nanosheets arrays for enhancing bifunctional electrocatalysis towards overall water splitting, Appl. Surf. Sci. 536 (2021), 147909.

[215] Y. Wang, Dispersed nickel cobalt oxyphosphide nanoparticles confined in multichannel hollowcarbon fibers for photocatalytic CO$_2$ reduction, Angew. Chem. In. Ed. 58 (2019) 17236–17240.

[216] H. Li, X. Zhao, H. Liu, S. Chen, X. Yang, C. Lv, H. Zhang, X. She, D. Yang, Sub-1.5 nm ultrathin CoP nanosheet aerogel: efficient electrocatalyst for hydrogen evolution reaction at all pH values, Small 14 (2018) 1802824.

[217] Y. Yin, J. Han, Y. Zhang, X. Zhang, P. Xu, Q. Yuan, L. Samad, X. Wang, Y. Wang, Z. Zhang, P. Zhang, X. Cao, B. Song, S. Jin, Contributions of phase, sulfur vacancies, and edges to the hydrogen evolution reaction catalytic activity of porous molybdenum disulfide nanosheets, J. Am. Chem. Soc. 138 (2016) 7965–7972.

[218] D. Xiong, C. Lu, C. Chen, J. Wang, Y. Kong, T. Liu, S. Ying, F.-Y. Yi, CoFeP nanocube-arrays based on Prussian blue analogues for accelerated oxygen evolution electrocatalysis, J. Power Sources 520 (2022), 230884.

[219] G. Li, X. Zhang, H. Zhang, C. Liao, G. Jiang, Bottom-up MOF-intermediated synthesis of 3D hierarchical flower-like cobalt-based homobimetallic phophide composed of ultrathin nanosheets for highly efficient oxygen evolution reaction, Appl. Catal. B: Environ. 249 (2019) 147–154.

[220] Y. Guo, Y.-T. Xu, B. Zhao, T. Wang, K. Zhang, M.M.F. Yuen, X.-Z. Fu, R. Sun, C.-P. Wong, Urchin-like Pd@CuO–Pd yolk–shell nanostructures: synthesis, characterization and electrocatalysis, J. Mater. Chem. A 3 (2015) 13653–13661.

[221] K. Zhan, C. Feng, X. Feng, D. Zhao, S. Yue, Y. Li, Q. Jiao, H. Li, Y. Zhao, Iron-doped nickel cobalt phosphide nanoarrays with urchin-like structures as high-performance electrocatalysts for oxygen evolution reaction, ACS Sustain. Chem. Eng. 8 (2020) 6273–6281.

[222] Y. Zhang, Heterogeneous interface engineering for boosting electron transfer induced by MOF-derived Yolk-shell trimetallic phosphide nanospindles for robust water oxidation electrocatalysis, Appl. Surf. Sci. 590 (2022), 153102.

[223] Y.V. Kaneti, Y. Guo, N.L.W. Septiani, M. Iqbal, X. Jiang, T. Takei, B. Yuliarto, Z. A. Alothman, D. Golberg, Y. Yamauchi, Self-templated fabrication of hierarchical hollow manganese-cobalt phosphide yolk-shell spheres for enhanced oxygen evolution reaction, Chem. Eng. J. 405 (2021) 126580.

[224] B. Yuan, C. Li, L. Guan, K. Li, Y. Lin, Prussian blue analog nanocubes tuning synthesis of coral-like Ni$_3$S$_2$@MIL-53(NiFeCo) core-shell nanowires array and boosting oxygen evolution reaction, J. Power Sources 451 (2020), 227295.

[225] T.L. Luyen Doan, D.T. Tran, D.C. Nguyen, H. Tuan, Le, N.H. Kim, J.H. Lee, Hierarchical three-dimensional framework interface assembled from oxygen-doped cobalt phosphide layer-shelled metal nanowires for efficient electrocatalytic water splitting, Appl. Catal. B Environ. 261 (2020), 118268.

[226] P. He, Carbon-incorporated nickel–cobalt mixed metal phosphide nanoboxes with enhanced electrocatalytic activity for oxygen evolution, Angew. Chem. . Ed. (2017).

[227] Y. Tang, X. Fang, X. Zhang, G. Fernandes, Y. Yan, D. Yan, X. Xiang, J. He, Space-confined earth-abundant bifunctional electrocatalyst for high-efficiency water splitting, ACS Appl. Mater. Interfaces 9 (2017) 36762–36771.

[228] J. Mu, J. Xu, C. Zhou, Q. Wang, X. Wang, Z. Liu, X. Zhao, E. Yang, Self-supported oxygen and molybdenum dual-doped cobalt phosphide hierarchical nanomaterials as superior bifunctional electrocatalysts for overall water splitting, ChemElectroChem 8 (2020) 103–111.

[229] J. Duan, S. Chen, C. Zhao, Ultrathin metal-organic framework array for efficient electrocatalytic water splitting, Nat. Commun. 8 (2017).

[230] N. Li, J. Han, K. Yao, M. Han, Z. Wang, Y. Liu, L. Liu, H. Liang, Synergistic phosphorized NiFeCo and MXene interaction inspired the formation of high-valence metal sites for efficient oxygen evolution, J. Mater. Sci. Technol. 106 (2022) 90–97.

[231] R.B. Ghising, U.N. Pan, D.R. Paudel, M.R. Kandel, N.H. Kim, J.H. Lee, A hybrid trimetallic–organic framework-derived N, C co-doped Ni–Fe–Mn–P ultrathin nanosheet electrocatalyst for proficient overall water-splitting, J. Mater. Chem. A 10 (2022) 16457–16467.

[232] C. Cui, R. Cheng, H. Zhang, C. Zhang, Y. Ma, C. Shi, B. Fan, H. Wang, X. Wang, Ultrastable MXene@Pt/SWCNTs' nanocatalysts for hydrogen evolution reaction, Adv. Funct. Mater. 30 (2020) 2000693.

[233] C.J. Zhang, B. Anasori, A. Seral-Ascaso, S.-H. Park, N. McEvoy, A. Shmeliov, G. S. Duesberg, J.N. Coleman, V. Gogotsi, V. Nicolosi, Transparent, flexible, and conductive 2D titanium Carbide (MXene) films with high volumetric capacitance, Adv. Mater. 29 (2017) 1702678.

[234] J. Chen, Q. Long, K. Xiao, T. Ouyang, N. Li, S. Ye, Z.-Q. Liu, Vertically-interlaced NiFeP/MXene electrocatalyst with tunable electronic structure for high-efficiency oxygen evolution reaction, Sci. Bull. 66 (2021) 1063–1072.

[235] N. Li, J. Han, K. Yao, M. Han, Z. Wang, Y. Liu, L. Liu, H. Liang, Synergistic phosphorized NiFeCo and MXene interaction inspired the formation of high-valence metal sites for efficient oxygen evolution, J. Mater. Sci. Technol. 106 (2022) 90–97.

[236] J. Wang, F. Ciucci, In-situ synthesis of bimetallic phosphide with carbon tubes as an active electrocatalyst for oxygen evolution reaction, Appl. Catal. B: Environ. 254 (2019) 292–299.

[237] X. Li, X. Wang, J. Zhou, L. Han, C. Sun, Q. Wang, Z. Su, Ternary hybrids as efficient bifunctional electrocatalysts derived from bimetallic metal–organic-frameworks for overall water splitting, J. Mater. Chem. A 6 (2018) 5789–5796.

[238] J. Li, Y. Xu, L. Liang, R. Ge, J. Yang, B. Liu, J. Feng, Y. Li, J. Zhang, M. Zhu, S. Li, W. Li, Metal-organic frameworks-derived nitrogen-doped carbon with anchored dual-phased phosphides as efficient electrocatalyst for overall water splitting, S Sustain. Mater. Technol. 32 (2022), e00421.

[239] B. Liu, R. Wang, Y. Yao, J. Ma, J. Sun, J. Wan, Y. Zhang, S. Wang, J. Zou, Hollow-structured CoP nanotubes wrapped by N-doped carbon layer with interfacial

charges polarization for efficiently boosting oxygen reduction/evolution reactions, Chem. Eng. J. 431 (2022), 133238.

[240] Y. Li, G. Tang, Y. Wang, Y. Chai, C. Liu, Interfacial engineering of a phase-controlled heterojunction for high-efficiency HER, OER, and ORR trifunctional electrocatalysis, ACS Omega 7 (2022) 13687–13696.

[241] Z. Chen, H. Jia, J. Yuan, X. Liu, C. Fang, Y. Fan, C. Cao, Z. Chen, N, P-co-doped carbon coupled with CoP as superior electrocatalysts for hydrogen evolution reaction and overall water splitting, Int. J. Hydrog. Energy 44 (2019) 24342–24352.

[242] Y. Liu, B. Wang, K. Srinivas, M. Wang, Z. Chen, Z. Su, D. Liu, Y. Li, S. Wang, Y. Chen, CNT-interconnected iron-doped NiP$_2$/Ni$_2$P heterostructural nanoflowers as high-efficiency electrocatalyst for oxygen evolution reaction, Int. J. Hydrog. Energy 47 (2022) 12903–12913.

[243] X. Wang, Z. Ma, L. Chai, L. Xu, Z. Zhu, Y. Hu, J. Qian, S. Huang, MOF derived N-doped carbon coated CoP particle/carbon nanotube composite for efficient oxygen evolution reaction, Carbon 141 (2019) 643–651.

[244] L. Chai, Z. Hu, X. Wang, Y. Xu, L. Zhang, T. Li, Y. Hu, J. Qian, S. Huang, Stringing bimetallic metal–organic framework-derived cobalt phosphide composite for high-efficiency overall water splitting, Adv. Sci. 7 (2020) 1903195.

[245] X. Li, Y. Fang, F. Li, M. Tian, X. Long, J. Jin, J. Ma, Ultrafine CO$_2$P nanoparticles encapsulated in nitrogen and phosphorus dual-doped porous carbon nanosheet/carbon nanotube hybrids: high-performance bifunctional electrocatalysts for overall water splitting, J. Mater. Chem. A 4 (2016) 15501–15510.

[246] C. Hu, M. Li, J. Qiu, Y.-P. Sun, Design and fabrication of carbon dots for energy conversion and storage, Chem. Soc. Rev. 48 (2019) 2315–2337.

[247] H. Song, J. Yu, Z. Tang, B. Yang, S. Lu, Halogen-doped carbon dots on amorphous cobalt phosphide as robust electrocatalysts for overall water splitting, Adv. Energy Mater. 12 (2022) 2102573.

[248] H. Liu, Z. Liu, Y. Wang, J. Zhang, Z. Yang, H. Hu, Q. Zhao, H. Ning, L. Zhi, M. Wu, Carbon dots-oriented synthesis of fungus-like CoP microspheres as a bifunctional electrocatalyst for efficient overall water splitting, Carbon 182 (2021) 327–334.

[249] H. Song, J. Yu, Z. Tang, B. Yang, S. Lu, Halogen-doped carbon dots on amorphous cobalt phosphide as robust electrocatalysts for overall water splitting, Adv. Energy Mater. 12 (2022) 2102573.